A NOVEL METHOD FOR THE QUANTIFICATION OF CORONARY ARTERY STENOSIS: A 2D QCA SYSTEM

A THESIS SUBMITTED TO
THE GRADUATE SCHOOL OF NATURAL AND APPLIED SCIENCES
OF
MIDDLE EAST TECHNICAL UNIVERSITY

BY

MUHARREM DEMİRAY

IN PARTIAL FULLFILLMENT OF THE REQUIREMENTS
FOR
THE DEGREE OF MASTER OF SCIENCE
IN
ELECTRICAL AND ELECTRONICS ENGINEERING

MAY 2015

Approval of the thesis:

A NOVEL METHOD FOR THE QUANTIFICATION OF CORONARY ARTERY STENOSIS: A 2D QCA SYSTEM

submitted by **MUHARREM DEMİRAY** in partial fulfillment of the requirements for the degree of **Master of Science in Electrical and Electronics Engineering Department, Middle East Technical University** by,

Prof. Dr. Gülbin Dural Ünver
Dean, Graduate School of **Natural and Applied Sciences** _____

Prof. Dr. Gönül Turhan Sayan
Head of Department, **Electrical and Electronics Engineering** _____

Assoc. Prof. Dr. Yeşim Serinağaoğlu Doğrusöz
Supervisor, **Electrical and Electronics Engineering Dept., METU** _____

Prof. Dr. Ahmet Tulga Ulus
Co-Supervisor, **Cardiovascular Surgery, Hacettepe University** _____

Examining Committee Members:

Prof. Dr. B. Murat Eyüboğlu
Electrical and Electronics Engineering Dept., METU _____

Assoc. Prof. Dr. Yeşim Serinağaoğlu Doğrusöz
Electrical and Electronics Engineering Dept., METU _____

Prof. Dr. Nevzat Güneri Gençer
Electrical and Electronics Engineering Dept., METU _____

Prof. Dr. Gözde Bozdağı Akar
Electrical and Electronics Engineering Dept., METU _____

Prof. Dr. Ahmet Tulga Ulus
Cardiovascular Surgery, Hacettepe University _____

Date: 15.05.2015

I hereby declare that all information in this document has been obtained and presented in accordance with academic rules and ethical conduct. I also declare that, as required by these rules and conduct, I have fully cited and referenced all material and results that are not original to this work.

Name, Last Name : Muharrem DEMİRAY

Signature :

ABSTRACT

A NOVEL METHOD FOR THE QUANTIFICATION OF CORONARY ARTERY STENOSIS: A 2D QCA SYSTEM

Demiray, Muharrem
M.S., Department of Electrical and Electronics Engineering
Supervisor: Assoc. Prof. Dr. Yeşim Serinağaoğlu Doğrusöz
Co-Supervisor: Prof. Dr. Ahmet Tulga Ulus

May 2015, 168 Pages

According to reports published by WHO, vascular diseases are leading cause of death and it is very widespread in both developing and developed countries. Therefore, diagnosis of coronary artery diseases plays an important role on health of the whole world. Although there exist many different imaging modalities used for coronary artery imaging like CTA, DSA and MRI, the most commonly used imaging modality in clinics is XRA. Using XRA images, interventional cardiologists give a decision about the treatment planning by investigating anatomic characteristics of stenotic coronary artery. Most of the clinicians do not have QCA tools to quantify the degree of stenosis automatically and they have to inspect the stenosis visually depending on their experience. Since visual inspection of a stenosis depends on the experience of the clinicians, clinicians are not able to agree on the severity of the same stenosis. This phenomenon is called as subjective interpretation and causes wrong decisions about the treatment planning. We propose a remedy to this phenomenon with a novel semi-automatic 2D QCA system which quantifies the stenosis severity by using the anatomical properties of the stenotic region. QCA system we have proposed is based on the deformable splines and their optimization using dynamic programming. Finally, 2D lesion characteristics are compared with

the FFR which is a gold standard technique on the determination of functional severity of a stenosis. In this way, correlation between 2D lesion characteristics and functional severity of a stenosis is investigated.

Keywords: Gabor Filter, Perona-Malik Anisotropic Diffusion, B-Spline Snakes, Dynamic Programming, Quantitative Coronary Angiography (QCA)

ÖZ

KORONER ARTER TIKANIKLIKLARININ NİCELİKSEL ÖLÇÜMÜ İÇİN YENİ BİR METOT: 2 BOYUTLU NKA SİSTEMİ

Demiray, Muharrem
Yüksek Lisans, Elektrik Elektronik Mühendisliği Bölümü
Tez Yöneticisi: Doç. Dr. Yeşim Serinağaoğlu Doğrusöz
Ortak Tez Yöneticisi: Prof. Dr. Ahmet Tulga Ulus

Mayıs 2015, 168 Pages

Dünya Sağlık Örgütü (DSÖ) tarafından yayınlanan raporlara göre, kalp damar hastalıkları ölümcül hastalıkların başında geliyor ve özellikle gelişen/gelişmekte olan ülkelerde çok yaygın. Bu yüzden, koroner arter hastalıklarının teşhisi dünya sağlığı için önemli bir role sahip. BTA, SÇA ve MRG gibi birçok farklı koroner damar görüntüleme teknikleri olmasına rağmen, klinikte en çok kullanılan görüntüleme metodu X-Işını Anjiyosu(XIA) dur. Girişimsel kardiyologlar, X-Işını Anjiyo görüntüleriyle tıkanık koroner damarın anatomik özelliklerini inceleyerek tedavi planlaması hakkında karar verirler. Birçok klinisyenin tıkanıklık oranını otomatik ve sayısal olarak saptayacak NKA araçları yok ve tıkanıklık oranını kendi tecrübesine dayanarak ve görsel olarak incelemek zorundalar. Tıkanıklık derecesinin görsel yolla incelenmesi klinisyenin kendi tecrübesine bağlı olduğu için, klinisyenler aynı tıkanık koroner damara bakarak darlık derecesi hakkında ortak görüşe varamazlar. Bu olay, subjektif yorumlama olarak adlandırılır ve hatalı tedavi planlanmasına sebebiyet verir. Darlık derecesini, tıkanıklık bölgesinin anatomik özelliklerini nicel olarak ifade eden yeni, yarı-otomatik 2 boyutlu bir Nicel Koroner Anjiyosu (NKA) sistemi sunarak bu probleme bir çözüm öneriyoruz. Önerdiğimiz yeni NKA sistemi, esnek yılanlar yöntemi ve bu yılanların dinamik programlama yoluyla optimizasyonuna

dayanır. Son olarak da, 2 boyutlu lezyon özelliklerini, damar tıkanıklığının fonksiyonel önemini belirlemede altın standart olarak kullanılan FAR sonuçlarıyla karşılaştırıldı. Böylelikle, 2 boyutlu lezyon özellikleriyle tıkanıklığın fonksiyonel önem derecesi arasındaki korrelesyon incelendi.

Anahtar Kelimeler: Gabor Filtre, Perona-Malik Anizotropik Difüzyon, B-teli yılanları, Dinamik Programlama, Nicel Koroner Anjiyosu (NKA)

To my dear wife

ACKNOWLEDGEMENTS

First of all, I would like to thank to my supervisor Assoc. Prof. Dr. Yeşim SERİNAĞAOĞLU DOĞRUSÖZ for her precious supervision, guidance, suggestions and encouragements throughout this study.

I am very thankful to Prof. Dr. Ahmet Tulga ULUS for his suggestions, assistance and guidance which make this study closer to clinical applicability and hence helpful to the health of patients having cardiovascular diseases.

I would like to thank to Prof. Dr. B. Murat EYÜBOĞLU, Prof. Dr. Nevzat G. GENÇER, Prof. Dr. Gözde BOZDAĞI AKAR for serving in my thesis defense committee and sharing their critics and opinions.

I am also thankful to my company ASELSAN for their great support and encouragement in the form of formal consent in workdays and transportation to the school.

I would like to express my sincere gratitude to my dear wife Gamze DEMİRAY who always supported and encouraged me patiently throughout this study.

I owe great thanks to my parents Ünzüle and Hüseyin, my sisters Nuray and Nurcan and my brother Adem for their endless support and encouragement throughout my whole educational and academic life.

Lastly, I am very thankful to my white tiny netbook, having 10.1 inches screen, 1.66 Ghz Intel Atom processor and 2 GB RAM, which accompanied me throughout this thesis study all the time.

TABLE OF CONTENTS

APPENDICES

LIST OF TABLES

TABLES

LIST OF FIGURES

FIGURES

LIST OF ABBREVIATIONS

AHE: Adaptive Histogram Equalization

AS: Area Stenosis

AV: Atrioventricular

CAA: Coronary Artery Anomalies

CAD: Coronary Artery Disease

CAG: Coronary Angiography

CCTA: Coronary CT angiography

CLAHE: Contrast Limited Adaptive Histogram Equalization

CT: Computed Tomography

CTA: Computed Tomography Angiography

CX: Circumflex Artery

DICOM: Digital Imaging and Communications in Medicine

DP: Dynamic Programming

DS: Diameter Stenosis

DSA: Digital Subtraction Angiography

FFR: Fractional Flow Reserve

HE: Histogram Equalization

IMP: Index of Merit of Pratt

LAD: Left Anterior Descending (artery)

LAO: Left Anterior Oblique

LL: Lesion Length

MLA: Minimum Lumen Area

MLD: Minimum Lumen Diameter

MSCT: Multi Slice Computed Tomography

NCD: Non-Communicable Diseases

PCA: Percutaneous balloon angioplasty

PCI: Percutaneous Coronary Intervention (formerly known as angioplasty with stent)

PMAD: Perona-Malik Anisotropic Diffusion

QCA: Quantitative Coronary Angiography

RAO: Right Anterior Oblique

ROI: Region of Interest

CHAPTER 1

INTRODUCTION

1.1. MOTIVATION

Vascular diseases are one of the most widespread health problems throughout the world, especially in developing countries. According to the report conducted by World Health Organization **[15]**, 38 of 56 million global deaths in 2012 were caused by noncommunicable diseases (NCD). Cardiovascular diseases, cancers, diabetes and chronic lung diseases are the four main NCD diseases. 75 % of deaths caused by NCD diseases occurred in low- and middle-income countries (According to the World Bank, Turkey is in the group of Upper-Middle Income Countries **[16]**). Among all the NCD deaths in 2012, cardiovascular diseases were the leading one with 46 % (17,5 of 38 million).

Cardiologists who use coronary angiographic images to describe the functional significance of an intermediate stenosis are usually unable to quantify it and they try to describe the stenosis qualitatively as: “a mild-to-moderate stenosis”, “a dubious lesion”, “an intermediate stenosis”, “a moderate stenosis”, “a non-flow-limiting lesion” etc. **[24]**. The most interesting and dramatic statistics is that 71 % of the Percutaneous Coronary Interventions (PCI) are done without any knowledge of functional significance of the stenosis **[24].**

A study conducted by J. Fischer **[14]** makes a comparison between visual assessment of a stenosis and Fractional Flow Reserve (FFR) of the same stenosis. For this purpose, they have three experienced interventional cardiologists classify some clinical subjects as “SIGNIFICANT”, “NOT SIGNIFICANT” and “UNSURE”. These labeled clinical subjects are then compared with the corresponding FFR index. If FFR index of a patient is greater than 0.8, it means that it is not a significant lesion; if FFR index of a patient is less than 0.8, it means that it is a significant

lesion. Result of this comparison is visualized in Figure 1.1 and shows the dramatic aspect of subjective interpretations of interventional cardiologists. While some cardiologists underestimate the functional significance of a stenosis which will result in a wrong diagnosis and wrong medical treatment; the others may overestimate the functional significance of the same stenosis which will result in unnecessary Percutaneous Coronary Interventions (PCI). Another point that needs special attention is that even experienced interventional cardiologists are "UNSURE" about the severity of the stenosis in some clinical cases. How can they find out correct treatment method when they are "UNSURE" about the case and have no accurate idea about the diagnosis?

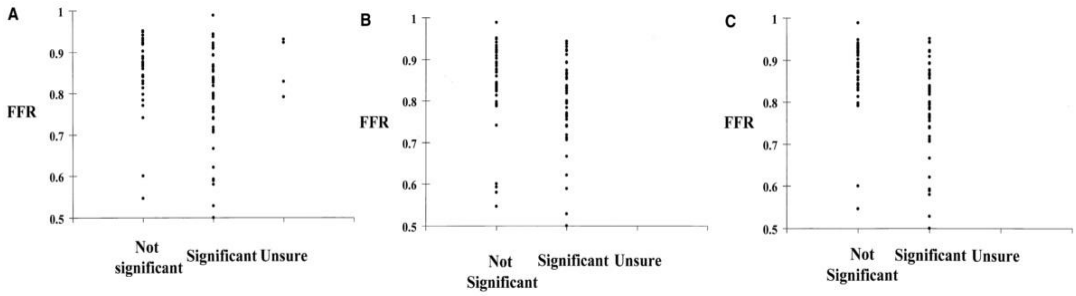

Figure 1.1: Comparison between visual assessment of cardiologists and FFR [14]

J. Fischer et al **[14]** make further comparisons between percent diameter stenosis (obtained via Quantitative Coronary Angiography (QCA)) and FFR; and between Minimum Lumen Diameter (MLD) and FFR as shown in Figure 1.2 and Figure 1.3 respectively. According to these statistical results, they conclude that there is a moderate level of correlation between functional significance of a stenosis and its anatomical properties (QCA) but they do not fully and accurately characterize the functional significance of a stenosis and may mislead the clinicians.

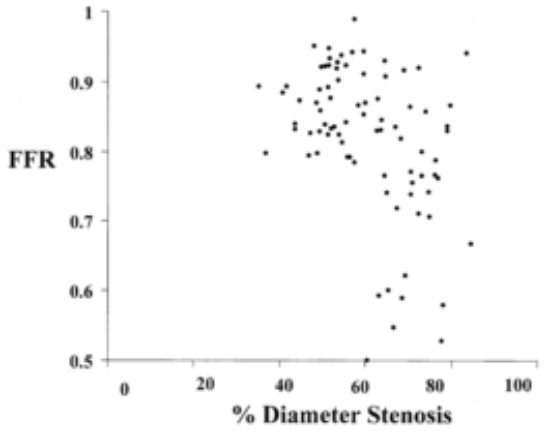

Figure 1.2: Comparison between percent diameter stenosis and FFR [14].

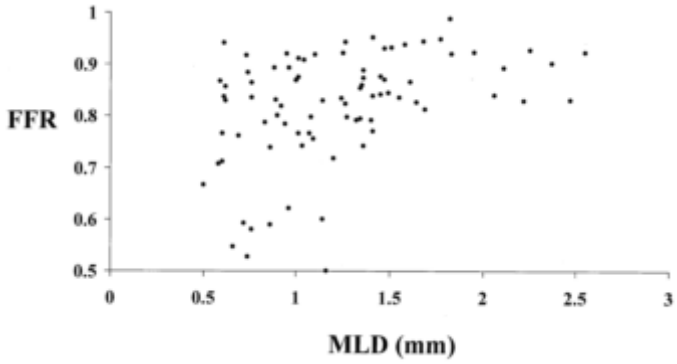

Figure 1.3: Comparison between Minimum Lumen Diameter (MLD) and FFR [14].

The widespread method of imaging coronary arteries is X-Ray Angiography (XRA). The main disadvantage of this imaging technique is that the resultant image is a 2D projection of the 3D vessel. 2D images therefore suffer from viewpoint dependency. In other words, while a stenotic artery is quantified as significant from one viewpoint; the same stenotic region may be quantified as non-significant when imaged from another viewpoint. Causes of this viewpoint dependency problem are stated in **[13]** as foreshortening effect and overlapping of peripheral arteries. Hence, viewpoint dependency in 2D angiograms is a big obstacle on the objective interpretation of the arterial diseases and on reliable diagnosis. Despite these well-known limitations of 2D QCA systems, they are reported to be the most commonly used and validated form of QCA systems **[58]**. Although accuracy of 3D QCA

systems are still being improved, there are comparative studies showing that 2D QCA systems are more accurate than 3D QCA systems **[78]**.

Another motivation and inspiration is to give an opportunity to the clinicians to investigate the functional significance of a stenosis in a non-interventional manner so that they do not need further operations (FFR) to measure the functional significance of a stenosis interventionally. Any little step into the estimation of functional significance of a stenosis non-interventionally is welcome in this field.

Since J. Fischer et al investigated the correlation between two QCA parameters with FFR and they could not explain the functional significance of a stenosis using only two QCA parameters, we will study more parameters related to the anatomical properties of a stenosis and investigate their effect on functional significance of the stenosis by using a novel 2D QCA system.

1.2. SCOPE

Scope of this thesis is mainly determined by the request and needs of interventional cardiologists who complain about the inter-operator variability in the interpretation of 2D XRA images of coronary stenoses. After a patient goes into Coronary Angiography operation, a council consisting of expert clinicians meet and discuss the treatment planning by assessing the stenosis visually. In these meetings, while some clinicians claim that stenosis is 80 % and needs PCI, the other claims that stenosis is 60 % and does not need any PCI operation. (This situation is called as subjective interpretation in the MOTIVATON part). If no agreement is reached on the functional severity of a stenosis, FFR operation is done for the measurement of functional severity of that stenosis.

In the Ph. D. thesis of Schrijver **[17]**, definition of severity of stenosis can be grouped into 3 main categories, namely: 1. Stenosis geometry and plaque composition, 2. Cardiac function 3. Vessel function (flow and perfusion). In the first category (i.e. stenosis geometry), severity of the stenosis is quantified using anatomical dimensions of the vessel such as, minimum diameter and cross-section in stenotic region, average diameter and cross-section in non-stenotic region etc. After these geometrical properties of the vessel are found, corresponding severity of

stenosis is defined as percent diameter stenosis, percent area stenosis. In the second category (i.e. cardiac function), stenosis severity is quantified using stroke volume ($V_{stroke} = V_{diast} - V_{syst}$), cardiac output (CO, stroke volume times heart rate) and ejection fraction ($EF = \frac{V_{stroke}}{V_{diast}} = \frac{V_{diast} - V_{syst}}{V_{diast}}$). As stated in **[17]**, cardiac function method is used for qualitative assessment of stenoses rather than quantitative assessment, since this method is not sensitive to coronary artery diseases. In the last category (i.e. vessel function), blood flow in the vessel is used rather than its geometry. In this approach, functional significance of a stenosis is determined by flow estimation methods.

In the scope of this thesis work, we will quantify the severity of a stenosis using the first category and investigate the correlation between blood flow parameters, as in the third category, and the parameters found in the first category. In other words, quantification of stenosis severity will be based on stenosis geometry and these geometrical properties of a stenotic vessel will be used in the investigation of functional severity of the stenosis by comparing FFR values of corresponding stenosis.

Aim of this thesis work is to assist the interventional cardiologists in the decision making process of quantification of coronary artery stenosis both anatomically and functionally.

Another constraint on the scope of the thesis is the cardiac imaging modality. Although there are many types of imaging techniques such as Computed Tomography Angiography (CTA) and Digital Subtraction Angiography (DSA), most commonly used imaging modality in clinics for the diagnosis of coronary stenoses is XRA. Therefore, this thesis study is based on XRA images.

1.3. CONTRIBUTION OF THE THESIS

In order to work with medical images, the first prerequisite is to read these images which are in DICOM format. DICOM is a standard for medical images to store, print and transmit patient-related imaging data. Every hospital capable of XRA imaging has to have a commercially available DICOM reader or viewer so that acquired images are handled by the clinicians. Therefore, we have developed a DICOM reader

tool as a first step through this study. This DICOM viewer is capable of reading DICOM images consisting of many frames, navigating between successive frames and displaying patient-related and imaging information embedded into DICOM via a GUI.

Perona-Malik Anisotropic Diffusion, which is used to smooth the noisy XRA image preserving the edge features of the vessel, is implemented in the scope of this study. Involvement of Perona-Malik Anisotropic Diffusion to increase the optimization performance of B-spline snakes prior to the application of Gabor filter is a novelty here. Also 2D Gabor filters and energy field calculated using the responses of Gabor filters with different orientations are implemented. The only code block which is taken from a reference **[57]** is the construction of B-spline snakes when the control points are given. Additionally, Canny and Contrast Limited Adaptive Histogram Equalization (CLAHE) functions are directly used from MATLAB library. Two different dynamic programming algorithms, which are used for the optimization of B-spline snakes, are implemented. The first one, which has high complexity and slow convergence, is proposed in **[11]**. We have proposed a new algorithm, which has lower complexity and faster convergence, which is also novel to this study. As an alternative to dynamic programming, a semi-automatic and faster method, which initializes and fits the B-splines using solely a few control points, is also implemented. The most significant contribution of this study comes from the vessel tracing algorithm, which is based on an analytical geometry approach, and this algorithm is used for the extraction of the anatomical features of a stenotic vessel.

Another contribution of the proposed QCA system comes for interventional cardiologists. Most of the cardiologists do not have a QCA system in their hospital and they have to decide the treatment plan by just inspecting the image visually. The proposed QCA system having a user-friendly GUI, with a reasonable running time, being validated with real patient data, giving the quantitative (not qualitative) results about the stenotic vessel is a remedy for clinical use.

To make the proposed QCA system useful for clinical practice, a user-friendly GUI is designed. GUI provides many useful features for the clinicians. Every intermediate step of the algorithm can be saved and observed by the user. This makes our

algorithm transparent to the user. For detailed features of the GUI, one can refer to Appendix B.

1.4. OUTLINE OF THE THESIS

This thesis work consists of 6 chapters. Chapter 1 is an introduction chapter which introduces the handled problem, motivation, scope and the contribution of this thesis study. In the next chapter (Chapter 2) background knowledge is presented to the reader to be able to fully understand and assess the work done here. Background chapter includes sub-chapters about coronary anatomy of the heart, common cardiovascular disease, cardiac imaging modalities, FFR and the challenges encountered throughout this study. After the first two chapters, the reader will have a better understanding related to the problem and the medical/clinical background. Therefore, the first two chapters serve as a warm-up for the reader.

After the reader is warmed up, Chapter 3 comes next and presents a literature review about the research activities related to the quantification of coronary stenosis. After this chapter, the reader can easily locate the proposed method in the existing literature. Following the literature review chapter, the proposed algorithm is presented in Chapter 4 so that location of the proposed algorithm in the current literature is much clear.

In Chapter 5, the proposed algorithm is investigated extensively by the help of experiments which test the robustness, time performance and the immunity of the algorithm to different conditions. Finally, a conclusion is drawn in Chapter 6. This chapter makes a summary and discusses the future work of this study.

Since this thesis is closely related to medical terminology, the reader may encounter with difficulties while reading this thesis work. To overcome this difficulty, an abbreviations list is prepared (just before Introduction chapter) and a glossary (Appendix A) so that reader can apply these two assistants whenever they encountered with an unknown abbreviation or a medical terminology.

CHAPTER 2

BACKGROUND

This chapter presents medical and biomedical background sections for the reader as a warm-up and a better understanding.

2.1. CARDIOVASCULAR ANATOMY

Coronary arteries composed of two main branches namely, Left Coronary Artery (LCA) and Right Coronary Artery (RCA). In the Figure 2.1 these two main branches from an anterior projection view are illustrated **[18].**

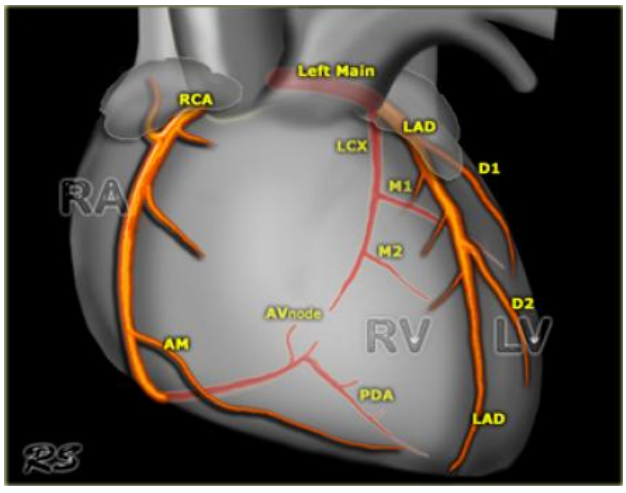

Figure 2.1: Main coronaries from anterior projection [18]

According to this illustration, coronary arteries can be grouped as follows:

- Left Main or left coronary artery (LCA)
    - Left anterior descending (LAD)

        - Diagonal branches (D1, D2)
        - Septal branches
    - Circumflex (Cx)
        - Marginal branches (M1,M2)
- Right coronary artery
    - Acute marginal branch (AM)
    - AV node branch
    - Posterior descending artery (PDA)

2.1.1. Left Coronary Artery LCA)

Left coronary artery is also called as Left Main Artery (LMA) and this main branch starts from the left coronary cusp [18]. LCA branches almost at the very beginning into Circumflex Artery (CX) and Left Anterior Descending (LAD) artery.

LAD branch lies in a region starting from anterior interventricular part up to the apex of the heart. While LAD supply blood to left ventricle and the AV-bundle, its sub branches(diagonal and septal) supply blood to anterior part of the septum and the anterior wall of the left ventricle [18].

The Circumflex (CX) artery lies between left ventricle and left atrium and it supplies blood to the lateral wall of the left ventricle [18].

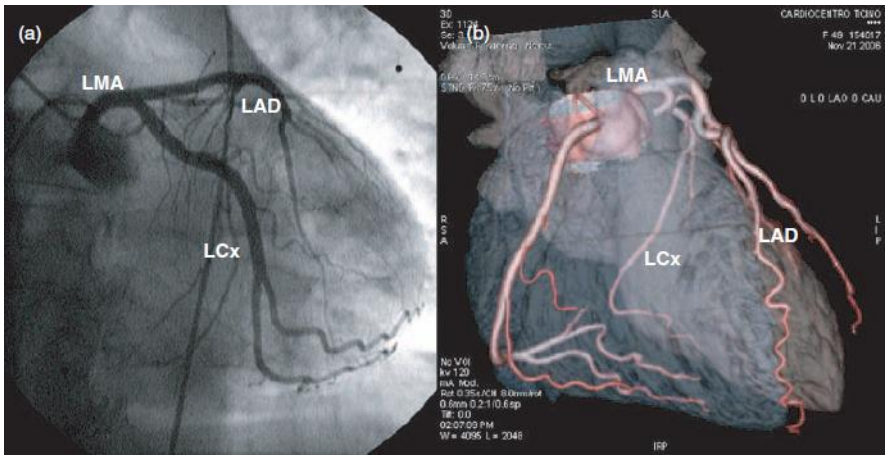

Figure 2.2: Coronary angiographic image obtained from antero-posterior projection.(b) Corresponding 3D volume image [19].

In Figure 2.2, a real angiographic image and its corresponding 3D image which show clearly the Left Coronary Artery (LCA) and its sub branches. Label LMA

stands for Left Main Artery and label LCX stands for Left Circumflex artery [19].

2.1.2. Right Coronary Artery (RCA)

RCA starts from anterior sinus of Valsalva and goes in between the right atrium and right ventricle until to the inferior part of the septum.

While Acute marginal (AM) branch supplies blood to the lateral wall of the right ventricle, PDA supplies the inferior wall of the left ventricle and inferior part of the septum. [18]

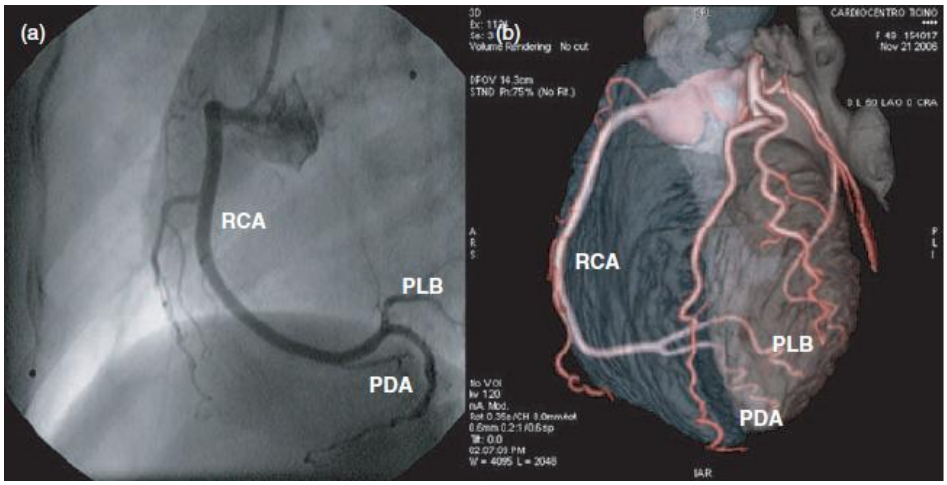

Figure 2.3: (a) Right Coronary angiographic image obtained from LAO 60o view. (b) Corresponding 3D volume image [19].

In Figure 2.3, a real angiographic image and its corresponding 3D image which show clearly the Right Coronary Artery (RCA) and its sub branches. Label PDA stands for Posterior Descending Artery and label PLB stands for Postero-Lateral Branch **[19]**.

2.2. CARDIOVASCULAR DISEASES

Common types of heart diseases are as follows [21]:

- Coronary artery disease (CAD)
- Arrhythmia
- Heart failure
- Heart muscle disease
- Congenital heart disease
- Atrial septal defects (ASD) and ventricular septal defects (VSD)

Among them, the most important one is the CAD. Cause of this disease is the existence of stenosis in a coronary artery. As defined in the glossary in Appendix A, stenosis is an abnormal narrowing of a blood vessel due to plaque formation inside the artery as shown in Figure 2.4. Plaque inside the artery is formed by the accumulation of fat and cholesterol.

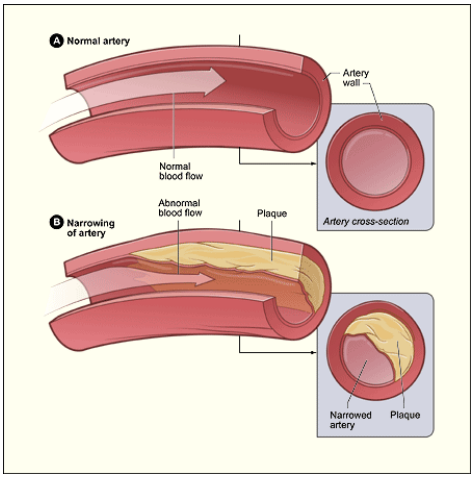

Figure 2.4: (A) Normal artery, (B) Stenotic artery due to Atherosclerosis [22]

2.2.1. Coronary Artery Diseases (CAD)

Types of coronary artery diseases are listed in [23] as follows:

- Acute Coronary Syndromes
- Advanced Ischemic Heart Disease
- Bifurcation Blockage
- Heart Attack (Myocardial Infarction)
- Microvessel Disease
- Stent Restenosis
- Total Coronary Occlusion

2.2.1.1. Acute Coronary Syndromes

Heart attacks occur due to the abrupt blockage of the coronary arteries which supplies blood to myocardium. Blockage in the artery is a layer which is formed due to the accumulation of fat and cholesterol. This layer is named usually as plaque. Criticality level of the coronary artery blockage is mainly determined by three factors

namely; location of the blockage point, the time passed after the blockage and resulting damage occurred in the myocardium **[23]**.

2.2.1.2. Advanced Ischemic Heart Diseases

Patients having advanced heart disease conditions have a great risk for repeat of heart attack**,** arrhythmias and even heart failure. Patients having chronic heart diseases could have chest pain although they had the required operations like coronary artery bypass surgery, angioplasty operations, and multiple stents **[23]**.

2.2.1.3. Bifurcation Blockage

If the blockage of the artery (as mentioned in A.) occurs just before the bifurcation point where main artery branches off; it is called as bifurcation blockage. This type of blockage is much more dangerous than the single branch blockage. Since, in this case more than one branch (i.e. 2) is blocked and wider area in the myocardium suffers from ischemia **[23].**

2.2.1.4. Heart Attack (Myocardial Infarction)

This condition is named also as myocardial infarction. "**myo-**" means muscle, "**-cardial**" means related to heart and "**infarction**" means death of the tissue **[23]**. When these words are gathered, myocardial infarction can be defined as the situation in which some part of the heart muscle dies due the lack of blood supply caused by the blockage of the artery. After myocardial infarction, some part of the heart muscle becomes non-functional, since it is dead.

2.2.1.5. Microvessel Disease

As can be understood from its name, this type of heart disease is related to tiny vessels which supplies blood to the little area of myocardial muscles. This disease occurs when some tiny blood vessels narrow down although they should widen **[23]**. As a result, less oxygen is supplied to the heart muscle which is feed by the narrowed micro vessel. Patients having this type of disease have generally a chest pain not a

fatal but a lessening the quality of life. Treatment of this disease is done using medications and life style changes instead of interventional operations.

2.2.1.6. Stent Restenosis

This disease is the stenosis of the artery which is treated early with a stent due to the former stenosis. In other words, stenosis is repeated in the same artery although a stent is located formerly **[23]**. These types of diseases require a special attention of an experienced cardiologist.

2.2.1.7. Total Coronary Occlusion

A complete blockage of a whole artery is called as total coronary occlusion. Total failure of the artery also causes a heart attack. Complete blockage of the artery lasting more than three months is named as chronic coronary occlusion **[23].**

2.3. CORONARY ANOMALIES

Coronary anomalies are very important since any type of anomaly has a potential of myocardial ischemia and sudden death [18]. Coronary Artery Anomalies (CAA) are commonly classified into three groups depending upon their origin, course and termination as seen in the below grouping **[18]**.

- Anomalies of the Origin
  - Anomalous origin of coronary artery from pulmonary artery
  - Single coronary artery
  - Origin from ‘non-coronary cusp’
- Anomalies of the Course
  - Myocardial bridging
  - Duplication
- Anomalies of termination
  - Coronary Artery Fistula
  - Extracardiac termination

2.3.1. Anomalies of the Origin

2.3.1.1. Absent Left Main Trunk

If a patient's heart does not have a Left Main Coronary Artery (LMCA), its sub branches LAD and LCX does not have a common origin. This anomaly is rarely observed in the population (0.41 – 0.43 %) and it is hemodynamically insignificant **[20]**.

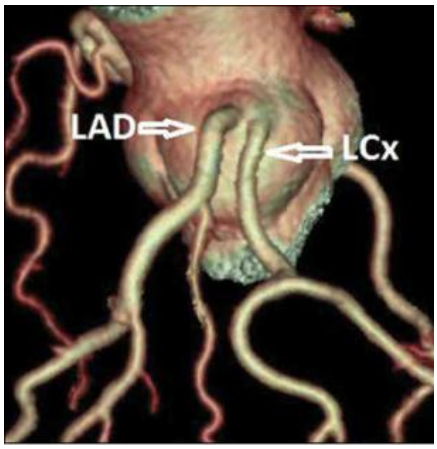

Figure 2.5: In case of absent Left Main Coronary Artery (LMCA) **[20]**

In Figure 2.5, although LAD and LCX are expected to originate from the LMCA as in the case of a healthy subject, their origins are not the same.

2.3.1.2. Anomalous Origin Of A Coronary Artery From The Pulmonary Artery

This type of anomaly is stated as the most serious and hemodynamically significant one in [20]. Most common form of this anomaly is called as ALCAPA and it is seen at each every live birth out of 300 000. If this anomaly is not treated, 90 % of infants die within the first year of birth. In some ALCAPA cases, it is observed that patients may reach the adult ages if there exists sufficient coronary collateral circulation. [20]

2.3.1.3. Anomalous Coronary Ostium Location

As can be inferred from its name, cause of this anomaly is the defective positioning of coronary ostium location. It is named as *low coronary artery ostium* if the ostium

is located at the lower end of coronary sinus; commissural *coronary artery ostium* if it is located within 5 mm of the aortic valve [20].

2.3.2. Anomalies of the Course

2.3.2.1. Anomalous Location of Coronary Ostium at Improper Sinus

If a coronary artery starts from an improper sinus, it follows one of the four possible paths to reach a normal position. While three of them are hemodynamically insignificant, one of them is hemodynamically significant and it is potentially risky for myocardial ischemia [20].

Hemodynamically significant course is called as interarterial course and this anomaly is known as the cause of the sudden cardiac deaths for athletic young adults. This risky course lies in between aorta and pulmonary artery as seen in the Figure 2.6 [20].

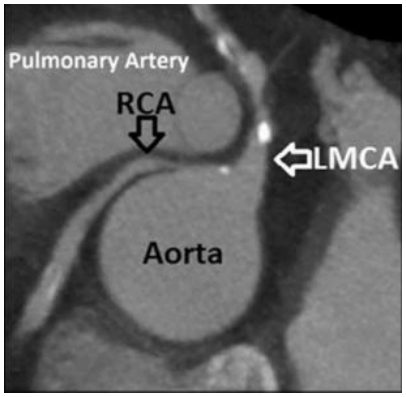

Figure 2.6: Interarterial course [20]

Hemodynamically insignificant courses are retroaortic course, prepulmonary course and transseptal course **[20].**

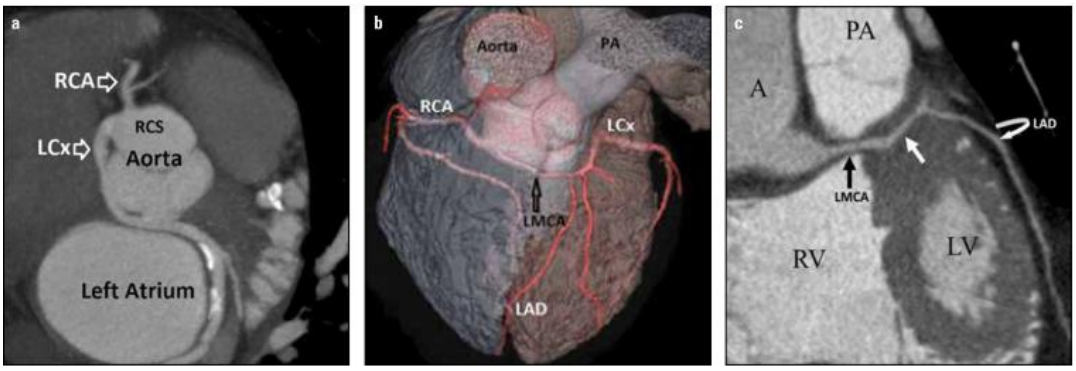

Figure 2.7: (a) retroaortic course, (b) prepulmonary curse, (c) transseptal course [20].

2.3.2.2. Intramural Coronary Artery (Myocardial Bridge)

This type of anomaly is common for Left Anterior Descending(LAD) artery [18] and defined as the tunneling of a coronary artery segment (usually LAD) through the some part of myocardial muscle [20]. Significance of this anomaly is mainly determined by the depth of the artery under the myocardium rather than the length of the myocardial bridging [18].

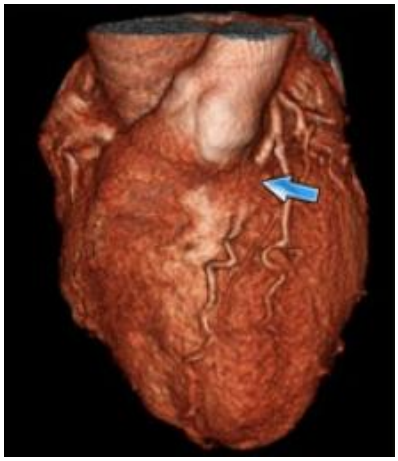

Figure 2.8: Myocardial bridging [18].

2.3.3. Anomalies of Termination

2.3.3.1. Coronary Artery Fistula

This anomaly is grouped according to its anomalous termination point. Some of these anomalous termination points are cardiac chamber, systemic vein, pulmonary artery etc. [20] The most frequently seen types of termination points are as follows: Right ventricle (41 %), right atrium (26 %), pulmonary artery (17 %) [20].

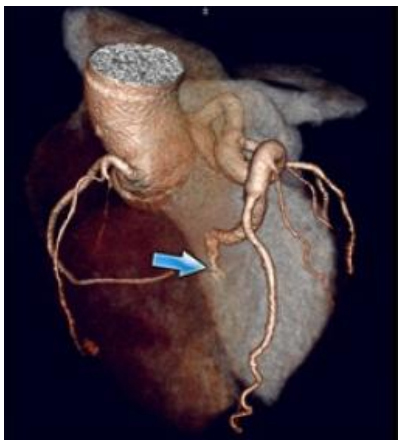

Figure 2.9: Coronary Artery Fistula terminating in the right ventricle [18]

2.4. CARDIAC IMAGING MODALITIES

Imaging is a key step for both diagnoses and treatment of Coronary artery diseases (CAD). Although early methods had limiting capabilities in terms of spatial and time resolution, contemporary imaging devices have an enormously increased time and space resolution. Recently, there exists many type of imaging modalities which are sometimes grouped as invasive or non-invasive; sometimes grouped as functional or anatomical. For our scope, we prefer to group imaging modalities as functional and anatomical.

2.4.1. Anatomical Imaging

Although functional imaging is used for intermediate and suspected CADs to determine the criticality level of stenosis, anatomical imaging is still needed for treatment and PCI planning phase. In some cases, functional imaging may not be enough or reliable for diagnosis (i.e. patients having diabete [30]) and additional anatomical imaging is applied in clinics. As can be understood, anatomical imaging is used as a supplementary method for functional imaging. However, depending upon the risk factors of the patient, local availability and experiences gained in years for a specific modality, anatomical imaging can be used solely for diagnoses and treatment of CADs [31].

2.4.1.1. Angiocardiography (X-Ray Angiography)

Angiocardiography is an cardiac imaging modality which exposes the heart to X-ray after the injection of radio-opaque material into coronary arteries. Radio-opaque material has a different X-ray attenuation factor than the tissue of the heart. In the resultant image therefore, only the coronary arteries are visible due to the contrast enhancement property of radio-opaque material. Images obtained from X-Ray Coronary Angiography (XRA) are 2D projections of the coronary arteries as it is common case for X-Ray imaging. Devices designed for imaging using this modality generally has a rotational C-arm. Therefore, radiologists have a chance of getting 2D angiographic projections taken from different viewing angles.

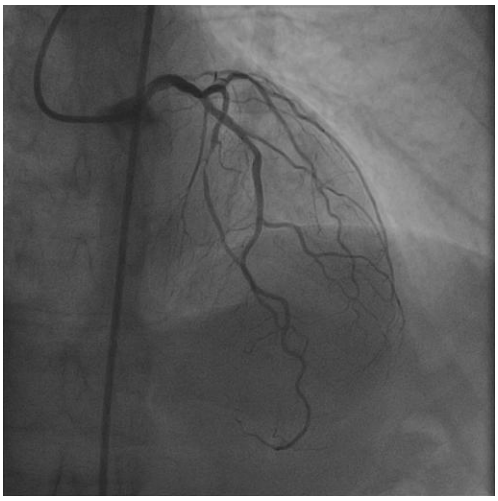

Figure 2.10: Image obtained from traditional XRA.

2.4.1.2. CT Angiography

Computed tomography (CT) is initially was not common for cardiac imaging due to its limitations. While CTA images were obtained using single slice in the early years, they are now obtained using up to 320-slice CT scanners. Using these multi-slice CTA images, now it is possible to visualize entire coronary anatomy.

Main difference of this modality from the standard XRA is that it is non-invasive. To obtain a CCTA (Coronary Computed Tomography Angiography) image, one does not need to position an intravascular catheter to main coronaries and inject a contrast-dye material.

Another advantage of CTA images over XRA images is that it enables radiologist to detect calcified and non-calcified plaques formed inside an artery.

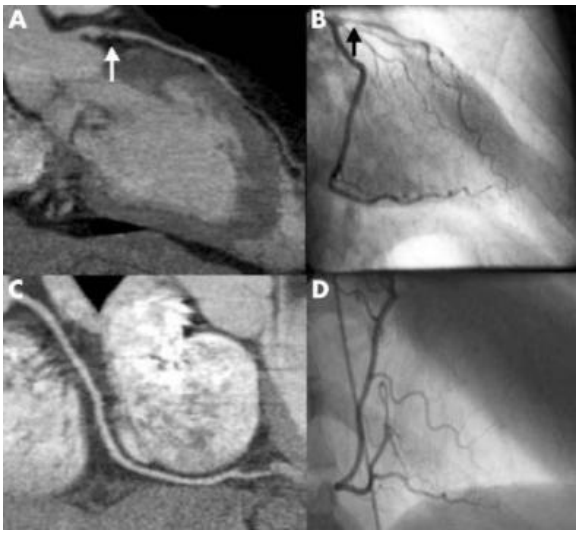

Figure 2.11: Images obtained from 16-slice MSCT (A,C) and corresponding XRA images (B,D) [30].

2.4.2. Functional Imaging

Since quantification of severity of coronary artery stenosis using anatomical imaging is very subjective and does not give a comprehensive information about the hemodynamic significance of the stenosis, functional imaging methos have great importance for CADs. Functional imaging modalities are mainly interested in myocardial perfusion and functionality of an artery.

Some well-known and popular functional imaging modalities are Single Photon Emission Computed Tomography (SPECT), Positron Emission Tomography (PET), Echocardiography and Magnetic Resonance Imaging (MRI).

2.4.2.1. Myocardial Perfusion Imaging (MPI) by SPECT and PET

SPECT and PET imaging is a technique used in nuclear medicine to determine the function of an organ or determination of cancer tissue. These techniques are called as nuclear, since they use radioactive drugs injected through the blood stream of the patient. Radioactive drugs start emitting radiation after reaching to the target tissue or organ. These emitted radiations are then imaged using special cameras (i.e. gamma camera). For the purpose of cardiac imaging, amount of emissions from radioactive drugs show the blood flow in the artery and myocardial perfusion.

SPECT and PET modalities generally use these radiopharmaceuticals: thallium-201, technetium-99m sestamibi, gallium and technetium-99m tetrofosmin [30].

These two modalities are said to be robust and have good diagnostic performance for diagnosis of CAD [31]. For example, an analysis conducted using 79 SPECT studies including 8964 patients revealed average sensitivity of 86 % and average specifity of 74 %. Another meta-analysis conducted using 15 PET studies including 1319 patients showed average sensitivity of 84% and average specifity of 81 % [31].

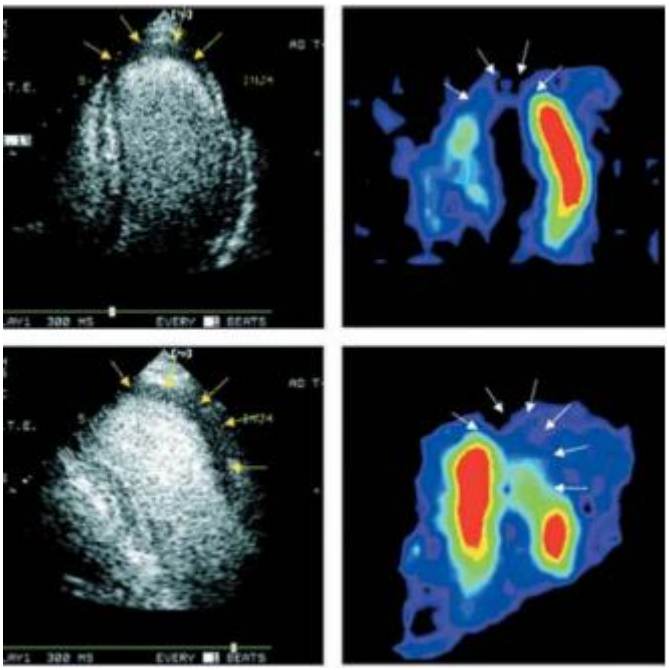

Figure 2.12: Myocardial Contrast Echocardiography (MCE) (left column) and corresponding SPECT images of a patient having anterior myocardial infarction [30].

In Figure 2.12, regions showed by the arrows have a decreased amount of opacification showing that there exist no blood flow in that region due to the infarcted heart tissue.

2.4.2.2. Echocardiography

Echocardiographic image of the heart is obtained using pulsed and continuous Ultra Sound (US) waves in conjunction with Doppler principles in a non-invasive manner. Although echocardiography enables to image both anatomy and functional

movements of intracardiac structures, its contribution on functional imaging is much more useful and precious.

When echocardiography is used for functional meaning, it gives information about heart wall motion abnormalities, blood flow direction and magnitude and myocardial perfusion [30], [32]. Heart wall abnormalities observed in echocardiography are indicators of CAD, ischemia and even infarcted myocardium [30].

15 studies (including 1849 patients) conducted to detect CAD using exercise echocardiograpy reported to have a weighted mean sensitivity of 84 % and weighted mean specifity of 82 % **[30]**.

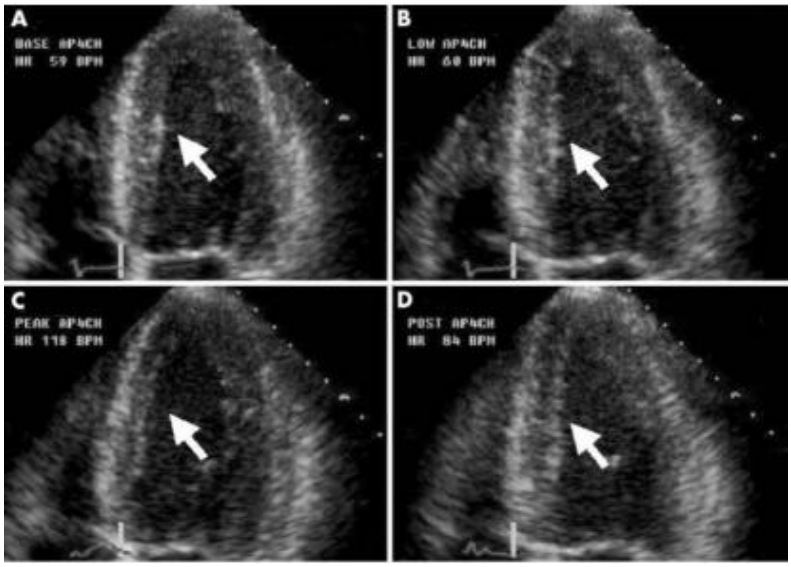

Figure 2.13: Echocardiographic images to observe wall motion abnormality. (A) Rest condition, (B) Low dose dobutamine applied image, (C) High dose dobutamine applied image, (D) Recovery condition.

In Figure 2.13, while normal wall motion is observed at rest and low-dose dobutamine injection conditions, a movement disorder (dyskinesia) is observed in high dose dobutamine case.

2.4.2.3. Cardiac MRI

Although MRI is well-known for anatomical imaging of soft tissue with high spatial and temporal resolution, it is started to be used in the assessment of hemodynamically significant CAD and myocardial perfusion with the recent

advances in the last decade. Why cardiac MRI seems promising for functional imaging of the heart is the emergence of MRI machines up to 3 Tesla and high spatial resolution capability with approximately 1 mm [33] [30].

Currently, cardiac MRI has become a validated technique and has a similar or better diagnostic accuracy than the commonly used techniques like SPECT and stress echocardiography [31]. Cardiac MRI has been reported to have a wide range of diagnostic accuracy of CAD, ranging from 38 % to 83 % in terms of sensitivity and 57% to 95% in terms of specifity [33]. Cause of this wide range accuracy is the different scanning protocols used in the studies. Another study conducted to investigate myocardial perfusion using MRI technique was done using 17 MRI perfusion studies and a total of 502 patients. Results of this study revealed that Cardiac MRI has e weighted mean sensitivity of 84% and specifity of 85% as seen Figure 2.14**[30]**.

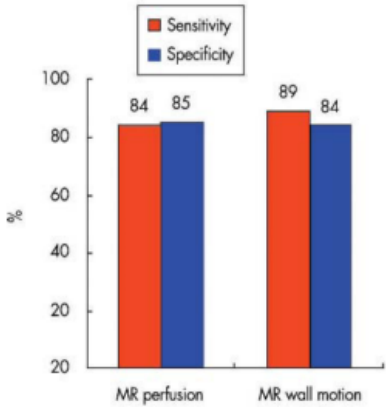

Figure 2.14: Diagnostic accuracy of cardiac MRI on perfusion and wall motion imaging **[30]**.

MRI does not expose the patient to ionizing-radiation and it has higher spatial resolution than CT images have.

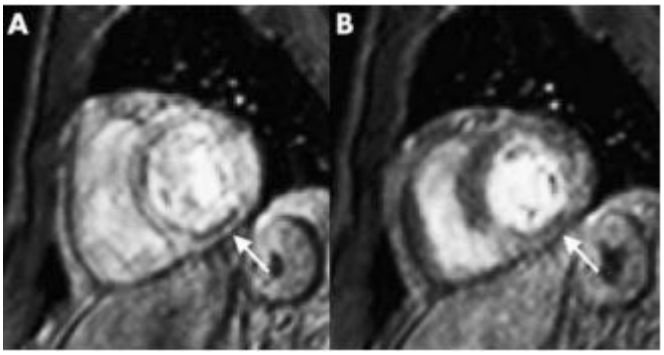

Figure 2.15: MRI perfusion images. (A) At rest condition, (B) Under stress condition [30]

Images shown in Figure 2.15 are obtained using MRI to investigate the myocardial perfusion under rest and stress conditions. Figure 2.15 (B) shows a fixed perfusion defect in the inferior wall of the heart [30].

2.5. WHAT IS FFR?

Although there exits very different types of indices that indicates the physiological significance of a stenotic artery like Coronary Flow Reserve(CFR), The index of microvascular resistance (IMR); Fractional Flow Reserve (FFR) is stated as the best validated one [24]. Variety of methods trying to measure coronary blood flow are comprehensively reviewed in [25]. Also in [26], FFR is said to be a proven and reliable method for the determination of physiologically significant coronary artery stenosis.

Why FFR has become a “gold standard” method in recent decades is that it has some specific and unique characteristics according to its rivals [24]. Firstly, it has a very standard and constant index showing the severity of the stenosis unlike the other clinical operations. For an healthy artery, it is calibrated and normalized to one (1) and according to the level of stenosis it deviates from 1(i.e. 0.9, 0.6, 0.4). Secondly, it has a strict cut off value (0,75 or 0.80) that discriminates the stenotic artery from the non-stenotic one. While FFR index greater than 0.80 shows functionally insignificant stenosis, FFR index less than 0.80 indicates the functionally significant stenosis. Thirdly, FFR measures are independent of gender, age, hypertension, diabetes. [24], [27]. Finally, FFR measurements are perfectly reproducible and independent of the systemic hemodynamics like blood pressure and heart rate. **[24]**

Fractional Flow reserve is an index showing the ratio of the possible maximum blood flow in the stenotic artery to the normal maximal blood flow in the same artery. This flow ratio is calculated as the pressure distal (after) to the stenosis (P_d) over the pressure proximal to the stenosis if and only if these two pressure values are measured during maximal hyperaemie [24]. Pressure at the proximal end of the stenosis is also called as aortic pressure (P_a). As a result, FFR formula is formed as follows:

$$FFR = \frac{P_d}{P_a}$$

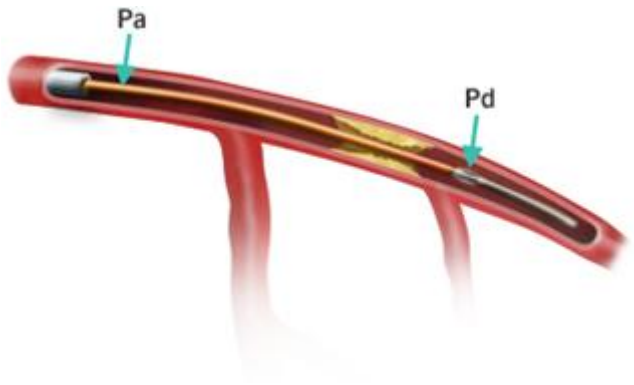

Figure 2.16: Simultaneous Pressure measurement [29]

Resulting FFR index is an absolute number showing the pressure drop after the stenosis. For example, FFR index 0.90 shows 10 % blood pressure drop, 0.70 shows 30 % blood pressure drop due to the narrowing of the artery.

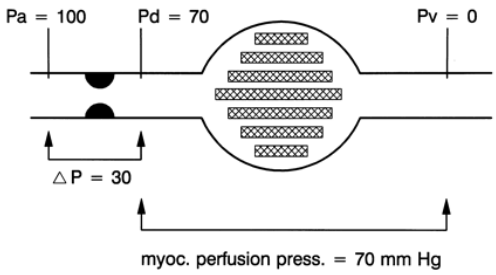

Figure 2.17: Aortic and distal pressure measures before and after the lesion [28]

In Figure 2.17, distal pressure would be 100 mm Hg if there was no stenosis and resulting FFR value would be approximately equal to unity indicating that there is no stenosis.

As previously stated, FFR index is independent of systemic hemodynamics [24] (i.e. blood pressure). Figure 2.18 is a good illustration showing that FFR is independent of the blood pressure. Initially, aortic and distal pressures are 60 and 45 mmHg respectively at maximum vasodilation. Corresponding FFR index is 0.75 (45/60) and pressure gradient over the stenosis is 15(60 -45) mmHg. Afterwards, aortic pressure is doubled to 120 mmHg. As a consequence, blood flow will double since it is pressure dependent at maximum vasodilation. Doubling flow will double pressure gradient to 30 mmHg and resulting distal pressure will be 90 mmHg. With these pressure values, FFR index will be 0.75 (90/120) which is exactly same with the previous case **[28]**.

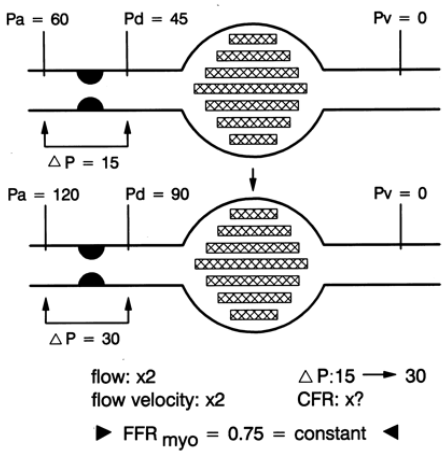

Figure 2.18: Figure showing that FFR is independent of blood pressure. [28]

2.6. CHALLENGES ENCOUNTERED IN ANGIOGRAPHIC IMAGES

2.6.1. Vessel Overlap

Coronary arteries consist of many main branches like LCA, LCX, RCA surrounding the surface of the heart. If the contrast material is given to the patient from the main branch of the artery, all branches would be visible and resulting in overlapped regions in 2D projections.

This is a major problem when clinicians try to assess the severity of a stenosis by visual inspection or a 2D QCA system.

Overlapped regions are shown darker in the image, since 2 times more blood/contrast dye exists in that overlapped region. These darker regions caused by overlapping, interferes the measurement of flow causing inaccurate estimate of blood pressure inside the artery for DSA-based blood flow measurement methods.

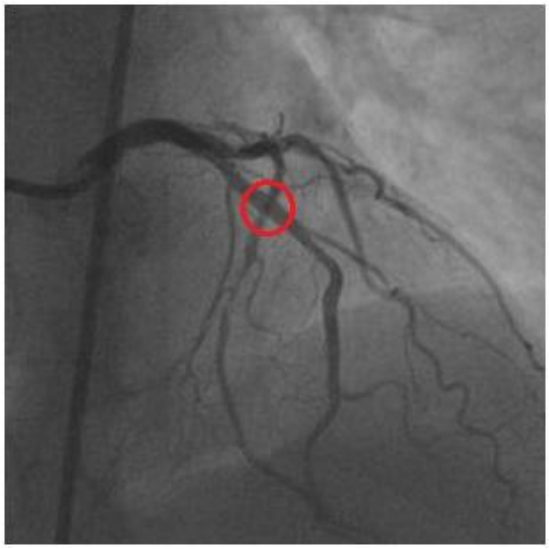

Figure 2.19: Overlapped arteries in the angiographic image

Another challenge related to vessel overlap is that overlapped region is NOT stationary but moving at each frame of angiography.

To overcome the overlapping problem, one solution is to give the contrast dye material to a single branch rather than giving it from the main coronary branch. However, this is not a common case in clinics since clinicians give the contrast dye material directly from a main coronary artery.

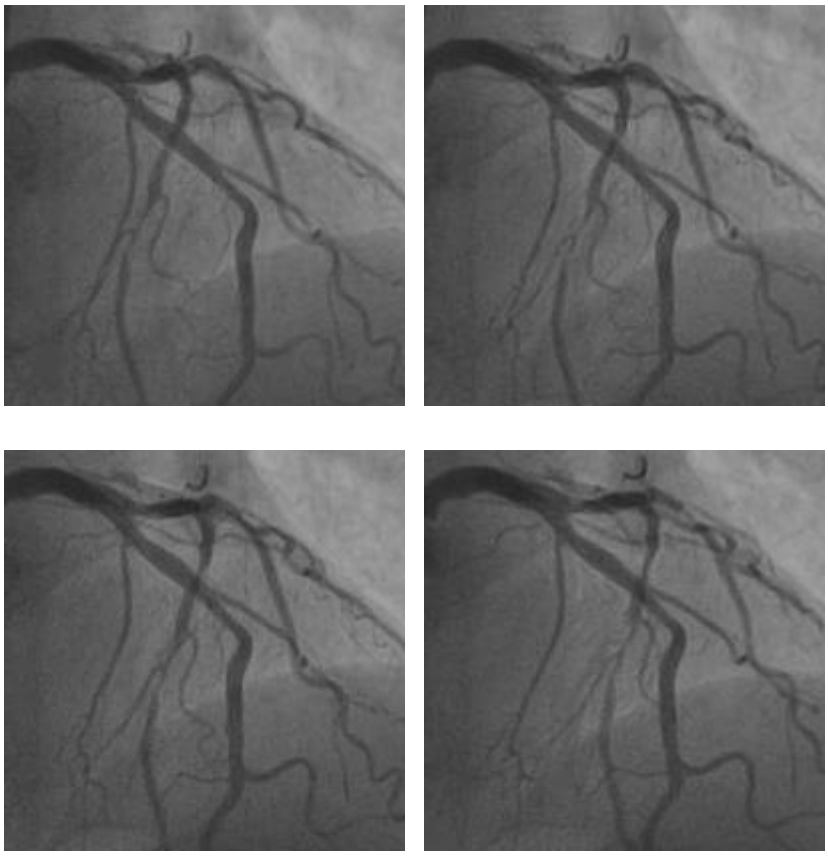

Figure 2.20: Overlapped region of the arteries moves in the subsequent frames

2.6.2. Movement of the Arteries

When clinicians try to assess the severity of the stenosis, they encounter with this challenge. While stenotic region is visible and clearer in a frame, it may be less visible, less clear or even may be overlapped in the next frame. Another problem is that while a stenosis is seen as critical in a frame, it may be observed as non-critical in the next frames.

2.6.3. Movement of the Heart

Movement of the heart is the source of the aforementioned problems (i.e. vessel overlap and movement of the arteries). Coronary arteries and the overlapped regions move due to the continuous movement of the heart which makes this movement for pumping the blood continuously.

2.6.4. Movement of Ribs due to breathing

Another factor causing the moving background is the inhalation of the patient. As the patient breathes, rib cage expands and shrinks continuously. Since ribs are moving during inhalation, background intensity changes before the dye is injected. After contrast dye is injected, visible coronary vessels may be overlapped with a moving rib and causing the clinician to give a wrong decision about the criticality of the stenosis.

Easiest solution for this problem is to make the patient not to breathe during the injection phase of the angiography. However, this may not be possible in most of the cases due to conditions of the patient.

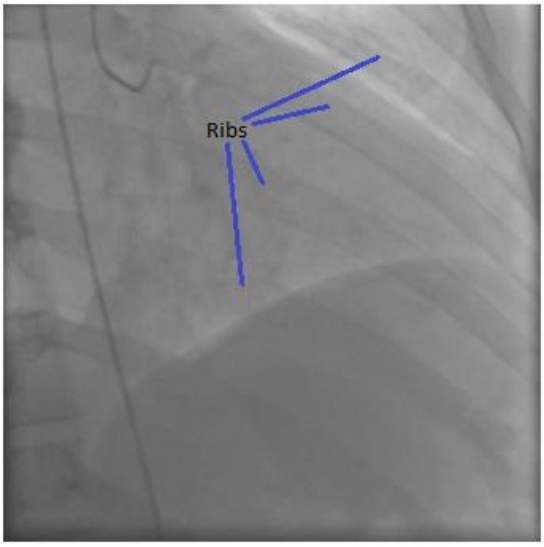

Figure 2.21: Ribs of the patient are visible prior to the contrast dye injection.

2.6.5. Equipments Used in Angiography

Unlike an ordinary CT or MRI imaging techniques, equipments used in this imaging modality is visible in Coronary Angiography. To be able to give the contrast material directly to the beginning of arteries, physicians go inside the body of the patient with a guide wire percutaneously. The catheter must be put inside the body, since contrast material fades away quickly and hence becomes invisible under X-ray. As a result, catheter is inside the body during the whole imaging process.

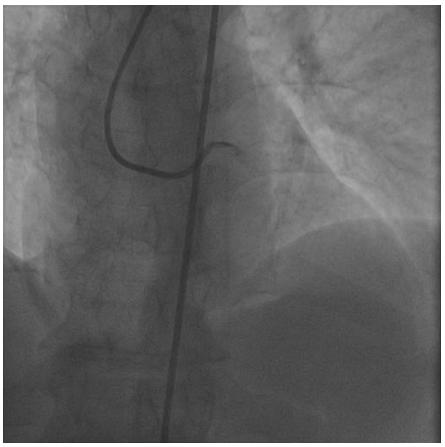

Figure 2.22: Catheter is visible in the angiographic image although contrast dye is not injected yet.

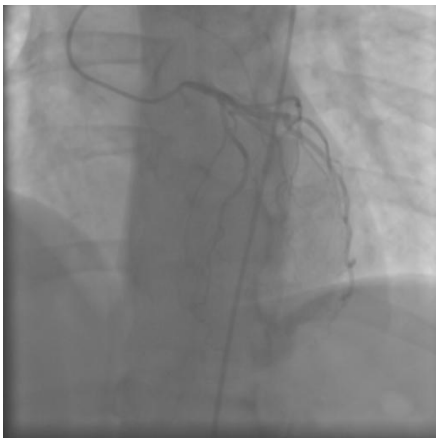

Figure 2.23: Catheter creates a disturbance, and seen as a vessel itself.

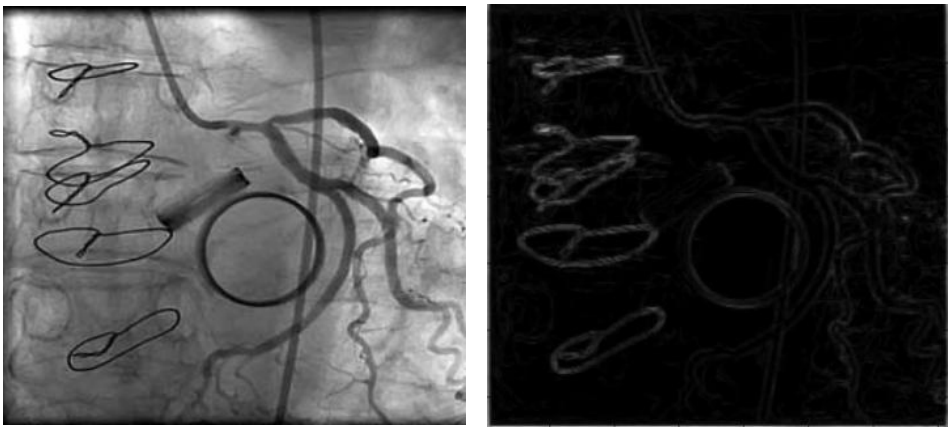

a b

Figure 2.24: (a) Instruments used during angiography is visible [24], (b) Gabor response of (a)

2.6.6. Foreshortening effect

Rotational XRA machines are capable of imaging the arteries from different angles in 3D space. Stenotic regions may be seen as narrower/wider than it really is when imaged in different angles. This effect is called as Foreshortening effect. Therefore, QCA systems are highly dependent on viewing angles.

2.6.7. Highly Noisy and Poor Contrast Environment

Imaging environment is so noisy that sometimes pixel intensities in vessel regions are much less than non-vessel regions. Sometimes Signal to Noise Ratio (SNR) level is too low for automatic or semi-automatic methods to recognize and extract the vessel edges.

CHAPTER 3

LITERATURE REVIEW

3.1. VESSEL EXTRACTION SCHEMES

Since the QCA system we have proposed based on the extraction of coronary vessels by using deformable splines, visiting a comprehensive literature review study on vessel extraction algorithms will be very beneficial to locate and understand the proposed vessel extraction scheme. The most cited and comprehensive literature review is done by Kirbas and Quek **[62]** and they categorize vessel extraction techniques into six categories: (1) Pattern Recognition Techniques, (2) Model-based Approaches, (3) Tracking-based approaches, (4) Artificial Intelligence-based Approaches, (5) Neural Network-based Approaches, (6) Tube-like Object Detection Approaches. They further categorizes some methods into sub categories:

I. Pattern recognition techniques

A. Multi-scale approaches

B. Skeleton-based approaches

C. Region growing approaches

D. Ridge-based approaches

E. Differential geometry-based approaches

F. Matching filters approaches

G. Mathematical morphology schemes

II. Model-based approaches

A. Deformable models

a. Parametric deformable models– Active contours (Snakes)

b. Geometric deformable models and front propagation methods

c. Deformable template matching approaches

B. Parametric models

C. Generalized cylinders approaches

III. Tracking-based approaches

IV. Artificial Intelligence-based approaches

V. Neural Network-based approaches

VI. Tube-like object detection approaches

3.1.1. Pattern Recognition Techniques

These techniques focus on the detection and classification of vessel features and vessel structures.

3.1.1.1. Multi-scale approaches

These approaches perform segmentation of image features at different image resolutions. Increased processing speed and the robustness of these approaches are said to be the main advantage comparing to the other approaches.

Sarwal and Dhawan **[63]** make a 3D reconstruction of coronary arteries by using images taken from three different views. Their method uses simplex method-based linear programming, relaxation-based consistent labeling and a matcher to match the branch points of each tree views. Why their method is classified into this group is that they use matching process at three different resolution to increase the robustness of the matcher.

Chwialkowski et al **[64]** also use a multi scale approach which is based on wavelet transform. Their purpose is to analyze the arterial flow qualitatively using MR images.

3.1.1.2. Skeleton-Based Approaches

As can be inferred from its name, these approaches extract the centerlines of the vessel as a skeleton. After centerlines are extracted individually, a vessel tree (skeleton) can be constructed by simply connecting each centerline.

Niki et al **[65]** make 3D reconstruction of blood vessels representing the anatomical structure of the vessel tree. Their reconstruction method is based on short scan cone-beam filtered back-propagation reconstruction algorithm. After 3D reconstruction, they apply 3D thresholding and 3D object connectivity for visualization.

Sorantin et al **[66]** also use a skeleton-based approach for the detection of tracheal stenoses by using spiral CT images. Their method consists of 5 steps: (1) Segmentation of LTT using a fuzzy connectedness approach, (2) 3D thinning operation, (3) Extraction of LLT medial axis, (4) Smoothing of LTT medial axis, (5) Calculation of LTT cross-sectional profile.

3.1.1.3. Region Growing Approaches

These approaches segment an image by starting from an initial seed point usually supplied by the user and incrementally adding pixels to specific regions depending upon some criteria. This criteria represents the similarity of a pixel to a region and generally value similarity and spatial proximity are used as segmentation criteria. Disadvantage of this algorithm is that it needs a user defined seed point although there exist methods feeding automatic seed points. Another problem related to these approaches is that they need post processing due to the oversegmentation caused by noise in the image.

Schmitt et al **[67]** use a region growing algorithm together with a thresholding technique to determine the propagation of contrast agent by using 3D rotational XRA images. After the segmentation done by region growing algorithm, propagation information taken from 2D projections are mapped to 3D image.

Yim et al **[68]** construct a vessel tree by using MRA images. MRA images are skeletonized in a gray scale manner by using an ordered region growing algorithm. The distinguishing part of this method is that the paths used in the region growing

algorithm do not depend on the location of the seed point which makes this algorithm reliable at every part of the constructed graph.

3.1.1.4. Ridge-based Approaches

These approaches treat images as topographical images in which intensity ridges are perceived as the skeleton of a feature of an object.

Bullitt and Aylward **[69]** use this approach to define vessel trees from 3D image volume. Their algorithm extracts an intensity ridge map, representing medial axis of the vessel, after manually selected seed points are defined for each vessel. The width of the vessel is calculated at each ridge point by using scale-based method.

Guo and Richardson **[70]** also use this method by treating angiograms as topological maps and treating vessel centerlines as ridges of that topological map. They use median filter and anisotropic diffusion filter to smooth the image. Then, by applying adaptive threshold method, a ROI is selected. Finally, ridge extraction is applied for the extraction of vessel centerlines.

3.1.1.5. Differential geometry-based approaches

These approaches perceive images as hypersurfaces and their feature extraction methods are based on curvature and crest lines of the hyper surface. Crest line of a surface is analogous to the centerline of the vessels. While 2D images are modeled as 3D hypersurfaces , 3D images are modeled as 4D hypersurfaces. Some studies using this approach are as follows: **[79] [80]**.

3.1.1.6. Matching filters approaches

These approach is based on the convolution of an image with a bank of matched filters so that the desired feature is extracted from the image. These bank of filters must be designed to extract the vessel having a specific size and orientation. Since this approach depends on convolution operation, size of the convolution mask play important role on the running time of the algorithm. Generally, after the application

of matching filters some post-processing steps are applied like thresholding and connected component analysis. **[81]** and **[82]** are examples of this approach.

3.1.1.7. Mathematical morphology schemes

In this approach, there are some morphological operators which are applied generally on binary images. Morphological operation can be defined as the application of a structuring element (SE) in any shape to an image so that some features are eroded or dilated. These operations are called as Erosion and Dilation. As can be inferred from their names, dilation operations dilates (expands) the objects and erosion operation erodes (shrinks) the objects. There are also two other operations which are successive application of erosion and dilation. First one is "Closing" (dilation + erosion), the other one is "Opening" (erosion + dilaiton). **[83]** and **[84]** use this approach .

3.1.2. Model-Based Approaches

Kirbas and Quek **[62]** divide these approaches into four category namely**,** (1) Deformable models, (2) Parametric models, (3) Generalized cylinders.

3.1.2.1. Deformable Models

Parametric deformable models use a parametric curve to represent and extract the boundaries of an object. This parametric curve deforms according to the forces acting on the curve. Forces influencing the shape of the parametric curve are internal and external forces. While external forces attract the curve towards the boundary of a feature (i.e. edge or line), internal forces try to keep the curve as smooth as possible. The main problem of this approach is that, usually a user interaction is needed for the initialization of snakes although there is still an ongoing research on automatic snake initialization.

The method proposed by Geiger et al **(85)** try to detect, track and match deformable contours. Their method uses noniterative Dynamic Programming (DP) and guarantees the finding of global minimum. Geiger et al use a multiscale approach to speed up the slow process caused by DP. While they are speeding up their process, they lose the guaranteed global minimum. Although they implemented the proposed

algorithm on medical images, they report that their method is applicable to any other type of images.

The method of Sarry et al **[86]** is based on a computer vision approach to track coronary arteries by using biplane DSA images. Their contour is a 3D one and based on 3D Fourier shape descriptors. They use 2D descriptors of the projected contour to obtain 3D Fourier descriptors. Unlike the other traditional 3D contour tracking methods which makes independent 2D tracking on each projection and then make 3D reconstruction, Sarry et al track 3D arteries using 3D parametrically deformable model.

Brieva et al **[11]** use a deformable model approach to extract the coronary stenosis from XRA images**.** Deformable model they used is indeed B-spline snakes which are a special form of snakes. Since B-splines are implicitly smooth, they do not need internal energy constraints. B-splines move only under the effect of external energy which is formed by the application of S-Gabor filters to the original XRA image. Then, they use Dynamic Programming (DP) to minimize the energy of the spline so that it attaches to the vessel boundary. After two B-splines are optimized, they use String matching technique to be able to quantify stenosis geometry. Main drawback of their algorithm is the high complexity of DP algorithm which makes it time consuming and impractical for clinical use.

3.1.2.2. Parametric models

These approaches treats the objects as parametrically. In other words, tubular objects (vessels) are defined as overlapping ellipsoids. The model parameters are then estimated by using the image itself. **(87)** is an example study based on parametric models.

3.1.2.3. Generalized Cylinders Model

As can be inferred from its name, this models uses generalized cylinders to represent the cylindirical objects (i.e. vessels). Although this method can be classified as parametric model, Kirbas and Quek **[62]** classify this method in a separate class. **(88)** uses Generalized Cylinders (GC) to find out the properties of coronary stenosis.

3.1.3. Tracking-Based Approaches

These types of techniques apply a local operator to detect the vessel and try to track it contrary to the pattern recognition techniques which apply local operators to the whole image to detect and classify the vessel features. Similar to the region growing approaches, these approaches also need an initial seed point to start tracking the vessel centerlines or boundaries.

Tolias and Panas **[71]** use a fuzzy C-means (FCM) clustering algorithm to track the fundus vessels in retinal angiograms. As a seed point for tracking, an optic nerve in fundus images is detected. After the boundary circle of the optic nerve is detected, points on this circle are classified as "vessel" or "non-vessel" by using FCM. Lastly, candidate points are examined by using fuzzy vessel tracking algorithm.

Park et al **[72]** also uses an adaptive tracking algorithm to extract vessel features and to find out narrow blood vessels by using DSA images. Their algorithm is designed to detect centerlines as direction vectors and to track adaptively direction field of entire vessel tree.

3.1.4. Artificial Intelligence-Based Approaches

This type of approaches are defined as knowledge-based approaches to guide the vessel extraction process. Different algorithms may use different knowledge like properties of image acquisition system, blood vessel model, anatomical structure etc. to guide the segmentation of vessel features.

Rost et al **[73]** propose a knowledge-based system for the extraction of contours. Their main purpose in this study is to minimize the change requirements of a system when transported to different environment.

Bombardier et al **[74]** also propose a knowledge-based system for the extraction of vessel boundaries automatically from angiogram images by using two fuzzy segmentation operators. For the extraction of vessel boundaries belonging to different anatomical structures (aorta or renal), they use different segmentation operators cooperatively. Their method consists of two main steps: (1) Identification of a ROI, (2) Detection of vessel boundaries.

3.1.5. Neural Network-Based Approaches

This type of approaches can be called as learning-based algorithms since they use neural networks for classification purposes. Neural networks consist of nodes which take any number of inputs and supplying a single output after application of some elementary computations. Commonly used types of neural networks require training to realize learning activity. This learning process is called as supervised learning. For the perception of medical imaging, neural networks are used for classification of segmented region after trained with a training data set.

Nekovei and Sun **[75]** propose a neural network-based back propagation algorithm for the detection of blood vessels in XRA images. Contrary to other approaches, this algorithm does not extract the vessel features but detects and labels pixels as "vessel" or "non-vessel". Input of the neural network is a sub window of the whole image which slides through the XRA image. Neural network is trained using the predefined labels in sub window. Finally, Nekovei and Sun compares their algorithm with two other algorithms to test their accuracy.

Hunter et al **[76]** use an algorithm which combines both neural network-based approach and knowledge-guided snakes for the extraction of Left Ventricular(LV) using Echocardiographic images.

3.1.6. Tube-Like Object Detection Approaches

As can be inferred from its name, these types of approaches try to extract tubular structures from the images. These approaches are also called as "miscellaneous" approaches since they combine different extraction methods for the extraction of tubular structures.

Kompatsiaris et al **[77]** propose a method for the detection of boundaries of stents using angiographic images. Initially, they detect the stent using a training set which is based on Principal Component Analysis (PCA). Then, a framework is constructed for the estimation of maximum likelihood to extract the stent. Finally, 2D active contours are used to refine the boundaries of found stent.

3.2. BLOOD FLOW ESTIMATION SCHEMES

Determination of blood flow non-invasively was very crucial since the early stages of medical image processing. Different sources are used for blood flow extraction like DSA, CTA and XRA images. We have categorized existing techniques and algorithms in the literature according to their source imaging modality like: (1) DSA-Based Methods, (2) CTA-Based Methods, (3) XRA-Based Methods

3.2.1. DSA-Based Methods

In **[44],** quantification of arterial blood flow is investigated using images obtained from 2D Digital Subtraction Angiography (2D DSA) in combination with three-dimensional rotational angiography (3DRA). The way that they estimated and quantified the blood flow velocity is based on optical flow approach using successive frames in X-ray video densitometry data. Although they validated proposed method using an in vitro setup, clinical validation is not performed and lacks in number of experiments. Even though pulsatile characteristics of the arterial blood flow is always a challenge for blood flow velocity extraction problems, they tackled this problem using constant contrast dye injection rate modulated by cardiac cycle.

In **[45]**, blood flow estimation and quantification algorithms are grouped into six categories:

- Indicator Dilution Techniques
- Concentration-time curves which are based on the measurement of variation of iodine concentration with respect to time
- Concentration-distance-time curves which are based on the measurement of variation of iodine concentration with respect to distance along the vessel and time
- First Pass Analysis (FPA) Tecniques
- Optical Flow Techniques
- Inverse Advection Problem

They claim that indicator dilution theory and Concentration-Time curve analysis fail due to the pulsatile nature of the blood flow. FPA techniques have difficulties about the accurate calibration of the iodine signal. Disadvantage of Inverse Advection

Problem is the computational complexity. Of all the techniques, they state that only Concentration-Distance-Time curves and Optical flow approaches give promising results. Due to these analyses, they propose improved versions of Concentration-Distance curve matching and Optical Flow algorithms to be able to measure blood flow using X-ray angiographic images. Both of the proposed algorithms are validated using computer simulation of pulsatile blood flow and physiological pulsatile blood flow circuit. Although they did not validated their algorithm using clinical data set, a set of criteria is presented in the paper for blood flow extraction algorithms to meet to be applied in clinical problems:

1) It should not use additional angiographic images more than the ones acquired during ordinary angiography not to expose additional radiation dose
2) It should work on little vessel segments which are a few centimeters in length.
3) It should give linear measurements so that different values of blood flow could be determined compared to a base-line value.
4) It shouldn't have high measurement variability
5) It shouldn't be affected by the contrast medium injection profile

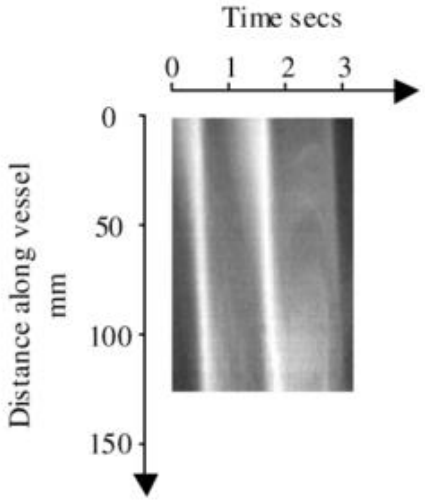

Figure 3.1: A Parametric image represents the motion of contrast dye material through the vessel [45].

Estimation and determination of blood flow is not only the concern for coronary arteries but also for cerebral arteries. In the paper **[48]**, a method is proposed to determine the blood flow waveform and mean volumetric flow rate in large cerebral

arteries using routinely acquired 3D Rotational Angiographic (3DRA) images. To be able extract flow information, they used a flow map which represents the progress of the contrast dye concentration with respect to both space and time. The proposed method is validated using experimental phantoms and some modifications to routine rotational angiography procedures are listed for clinical applicability.

In **[49]**, a numerical scheme for the inverse advection problem is proposed to estimate the blood flow velocity using X-ray densitometric data. Since in the early papers published by Sarry et al **[50]**, they made a relation between blood flow velocity and contrast bolus density using Inverse Advection problem, this paper **[49]** only deals with the proof of the existence and uniqueness of the solution using an efficient numerical scheme. As also stated by **[45]** and **[49]**, Inverse Advection Problem approach suffers from computational complexity while using parameter estimation algorithm.

A more recent study is published for the quantification of blood flow in the Internal Carotid Artery (ICA) by using Digital Subtraction Angiography (DSA) **[51]**. The proposed algorithm is an Optical Flow (OF) –based and it is validated by comparing the results obtained from Doppler Ultrasound (US). Together with 2D DSA images, they used 3D rotational Angiography (3DRA) for the extraction of vessel centerlines. Extracted centerlines from 3DRA were later used in the calculation of volume flow. Main drawback of the proposed OF-based algorithm is that its performance is good for only in a limited range of contrast agent Injection Rates (IR) (1.5 mL/s < IR< 2 mL/s).

Another recent study which uses Optical Flow (OF) approach for the quantification of blood flow is published by Maday et al **[52]**. Their estimated volumetric flow rate measurements are based on 2D DSA images and vessel segmentation obtained using 3DRA. Their novelty to OF approach comes from the use of vessel aligned coordinate system which enables estimation of blood flows for even consecutive frames having a large displacement in between. They evaluated the performance of their algorithm using synthetic DSA datasets for different flow velocities and different acquisition rates.

Hentschke et al had also tried to estimate the blood flow velocity using cerebral angiographic data **[53]**. They used 2D DSA images to track the propagation of the

contrast material and to find the vessel centerlines. Found vessel centerlines are then back projected to 3DRA data to recover the spatial data 2D DSA images. Accuracy and the performance of the algorithm are examined using both phantom and patient data.

[54] also tries to quantify blood flow in cerebral arteries. Their method requires the combined use of both 2D DSA and 3DRA. They use a physical model of contrast agent propagation and blood flow for flow quantification. Therefore, their approach can be named as model-based approach. They examined and validated the proposed approach on a patient cohort consisting of 24 patients by comparing the results with Transcranial Color Coded Doppler (TCCD).

3.2.2. CTA-Based Methods

The state of the art paper **[46]** which was published in 2013 presents a novel method which non-invasively quantifies the Fractional Flow Reserve (FFR) using CTA images. FFR value derived from CTA images are called as FFR_{CTA} in this scope. Emergence of FFR_{CTA} is highly dependent on the advances in the fields of Computational Fluid Dynamics (CFD) and image-based modeling. After the advances in these fields, FFR_{CTA} is now possible by the involvement of three steps: (1) Construction of accurate anatomical model of epicardial coronary arteries in a patient-specific manner, (2) Determination of inflow and outflow boundary conditions which simulates the coronary physiology of the patient during maximal hyperemia condition, (3) Numerical solution of Fluid dynamic equations. In other words, FFR_{CTA} is available thanks to the incorporation of three profession namely, Anatomy, Physiology and Computational Fluid Dynamics. Blood flow and pressure are computed using the fundamental equations of fluid dynamics which are conservation of mass, balance of momentum and Navier-Stokes equation. Although these equations are valid for a Newtonian fluid and blood is not a Newtonian fluid, blood is approximated as Newtonian fluid having a constant viscosity. Since FFR_{CTA} requires accurate anatomic model, artifacts like calcification, motion and misregistration causes inaccurate measures for stenosis severity. FFR_{CTA} measures have reported to have superior results about the hemodynamic significance of a stenosis than the measures obtained using CTA which generally overestimates the

severity of stenosis. For detailed scientific basis of FFR_{CTA} , one can apply the paper published by Taylor et al **[47]**.

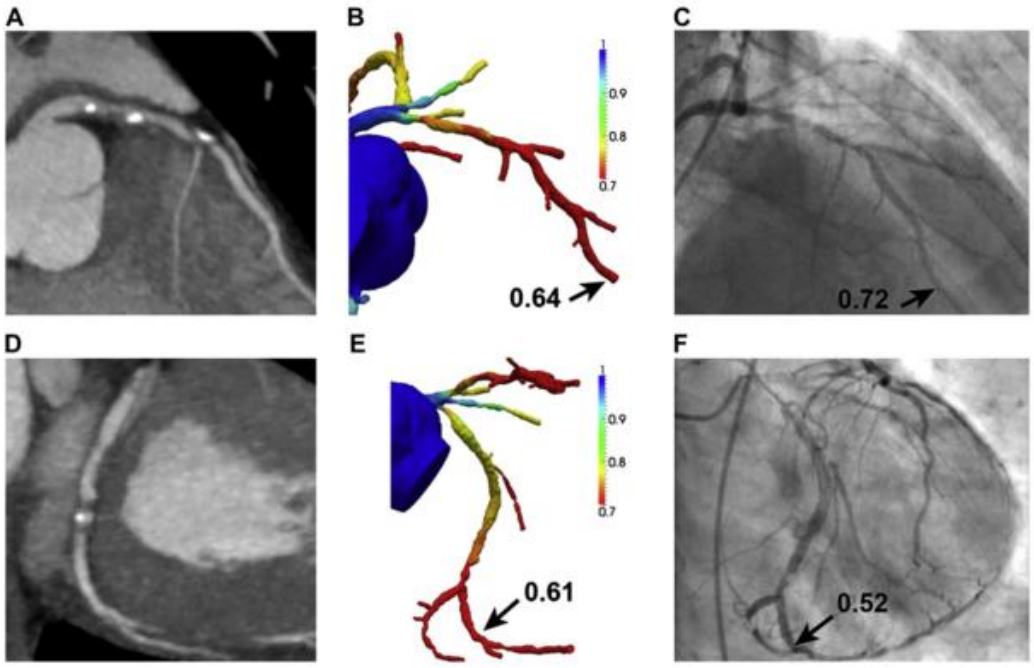

Figure 3.2: (A) CTA image showing a stenosis in LAD, (B) FFRCTA estimates FFR value as 0.64, (C) True FFR value is measured as 0.72, (D) CTA image showing a stenosis in LCX, (E) FFRCTA estimates FFR value as 0.61, (F) True FFR value is measured as 0.52 [46].

3.2.3. XRA-Based Methods

These types of methods directly use XRA (unlike DSA) images and quantify the stenosis by using 2D or 3D QCA systems. After the interested stenoses are quantified, correlation between anatomical properties of stenotic vessel and its physiological significance are investigated in a statistical approach. Fractional Flow Reserve (FFR) is used as ground truth data for physiological significance of a stenosis, since it is a gold standard in clinics. [**12**] and **[14]** are examples of studies using XRA images to relate it to the functional significance of a stenosis.

As can be predicted, these methods rely on 2D or 3D QCA systems and ground truth FFR values which are taken from real patients.

3.3. POSITION OF PROPOSED ALGORITHM IN THE LITERATURE

According to the classification of Kirbas and Quek **[62],** the proposed algorithm in this thesis can be classified in Model-Based approaches. In more detail, it can be classified in Parametric Deformable Models since it uses deformable B-spline snakes to extract the coronary vasculatures. The proposed algorithm also can be categorized in Pattern Recognition Techniques, since it uses differently oriented bank of Gabor filters like in the matching filters approach. As a result, the proposed algorithm can be classified in both Model-Based approaches and Pattern Recognition Techniques according to the classification of Kirbas and Quek.

Since the source image is XRA (not DSA and CTA), our proposed algorithm can be classified in XRA-Based Methods.

3.3.1. Rationale of Selection of the Proposed Algorithm

As a vessel extraction algorithm, we have chosen a deformable model based approach together with a pattern recognition technique. Deformable models (i.e. B-spline snakes) are good at representing the vessel borders due to their characteristics like: smoothness, continuity, variable shape conformation complexity etc. After removing the disadvantage of snake optimization scheme, which is high complexity and long-lasting one, and replacing it with a low complexity and speedy one; the proposed algorithm becomes more feasible for clinical applications.

The method we have proposed uses XRA images, since it is widely used in clinics for the diagnosis of coronary diseases compared to DSA and CTA images. This is another point that makes our QCA system clinically feasible.

When DSA-based methods are reviewed, it is obvious that these methods generally use DSA images taken from in vitro setup and validated using phantom images. Those using real patient data use DSA images of brain which are stationary inside the skull unlike coronary arteries which continuously move together with the heart. Since blood flow information is extracted from the parametric images in these approaches, distortion in parametric images completely spoils the blood flow information. Continues movement of coronary arteries truly distorts the parametric image and no healthy blood flow information can be measured for coronary arteries.

This is the reason why DSA-based blood flow calculations are not feasible for coronary arteries.

In CTA images, in addition to the coronaries, also some other heart tissues are visible and they create disturbances on the diagnosis of the coronary disease. Clinicians do only care about the coronary arteries itself rather than the myocardial tissues on the heart. That's why CTA images are not so common in clinics for the diagnosis purposes.

3.3.2. Comparison of Selected Methods with the Other Methods in the Literature

3.3.2.1. Contrast Limited Adaptive Histogram Equalization (CLAHE)

Histogram equalization (HE) is a fundamental and easy way of image enhancement. There are also many types of histogram equalization techniques to overcome the main disadvantages of HE. Adaptive Histogram Equalization (AHE) is a variant of HE method which adaptively enhances the image regions but it over amplifies the noise. CLAHE prevents this noise amplification by limiting the amplification factor adaptively **[89]**.

After traditional HE method is proposed, various types of this method are proposed like "Dualistic sub-image histogram equalization method", "Dynamic histogram equalization for image contrast enhancement" and "Adaptive Histogram Equalization method" as mentioned in **[90]**. In a more recent paper **[91]** histogram equalization techniques are studied comparatively under the following grouping: "Bi-Histogram Equalization Methods Bi-histogram", "Multi Histogram Equalization Methods In" and "Clipped Histogram Equalization Methods".

This method is used for contrast enhancement (image enhancement) and hence serves as a visual aid to the user while initializing splines in a poor contrast environment. Since having a poor contrast environment is a very common problem for X-Ray Angiographic images. CLAHE is not an indispensible step of our algorithm. It is an assistive step for the end user. If this step is not used in the proposed algorithm, user initializes the splines on the original image rather than

contrast enhanced image. Also type of the used HE method does not matter for our algorithm. Any type of HE could be used for image enhancement. We have used built-in function of MATLAB for CLAHE with its default settings.

3.3.2.2. Perona-Malik Anisotropic Diffusion (PMAD)

Unlike the traditional linear smoothing filters (i.e. Gaussian filter) which smooth the whole image including edges, PMAD smoothens the image while preserving edge features in the image. Some examples of edge-preserving smoothing filters are Bilateral Filter, Guided Filter and Anisotropic Diffusion Filter. Bilateral filter is first introduced by Tomasi and Manduchi **[92]** as a non-linear edge-preserving smoothing filter. Bilateral filters smooth the image by combining the neighbor pixel values in a non-linear manner. Unlike the PMAD, bilateral filters are non-iterative. Guided filters **[93]** are also edge-preserving smoothing filters and claimed to have better performance near edges compared to the popular bilateral filters. Guided filters are very widely used in computer vision and computer graphics applications like edge-aware smoothing, detail enhancement, HDR compression, image matting/feathering, dehazing, joint upsampling, etc **[93]**. Also Median Filter, Symmetrical Nearest Neighbour Filter (SNN), Maximum Homogeneity Neighbour Filter (MHN), Conditional Averaging Filter are listed as the edge-preserving smoothing non-linear filters in **[94]**.

PMAD is used just prior to the application of Gabor filters as a pre-processing step to smooth the noisy image by conserving the edge features. If PMAD would not be used before the Gabor filter, edge features in the Gabor response will be not well-localized as shown in Figure 4.6 (a). If PMAD is used, edge features in the resultant Gabor response is well-localized as shown in Figure 4.6 (b). Well-localized edge features are important for the following steps of the algorithm. Gabor response represents the edge features of the image and is used as an external energy function for the B-spline optimization step. If the edge features are not well-localized, B-spline snakes cannot be optimized well-enough as shown in Figure 4.7 (a)(c)(e)**.** Figure 4.7 (b)(d)(f) show how good splines are optimized when PMAD is used. If the optimized splines do not represent the vessel edges good enough, coronary stenosis cannot be detected and quantified which is the very fundamental purpose of this

thesis study. In conclusion, PMAD affects the overall quality of the proposed algorithm. Instead of PMAD, its counterparts like Bilateral Filter, Guided Filter, Median Filter could also have been used for the same purposes.

3.3.2.3. Gabor Filter

Gabor filters are scale and orientation dependent linear edge detection filters. They are used to extract and represent the edge features of an image. Alternatively, other first order and second order edge detection algorithms could be used as an external energy function for spline optimization. In a recent survey on edge detection algorithms **[95]**, edge detection algorithms are classified into two main groups like first order and second order algorithms as shown in Figure 3.3.

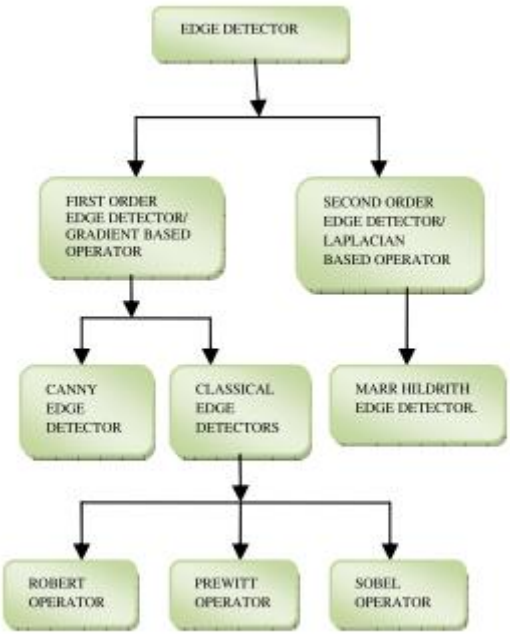

Figure 3.3: Classification of edge detectors **[95]**

First order edge detection algorithms like Sobel, Roberts and Prewitt suffer from noise and discontinuity in edges as shown in Figure 3.5. Second order Laplacian-based methods like Marr Hildrith operators suffer from two things namely, false edge detection probability and high localization error at curved edges. Among all edge detectors, Canny edge detector is known as the best edge detector since (i) it has an

adaptive nature, (ii) has a better performance in noisy images, (iii) good edge localization, (iv) low false alarm rate **[95].**

For a detailed analysis of both Canny edge detector and Gabor filter, one can apply to **[96]** in which solely Canny edge detector and Gabor filters are investigated in the edge detection point of view.

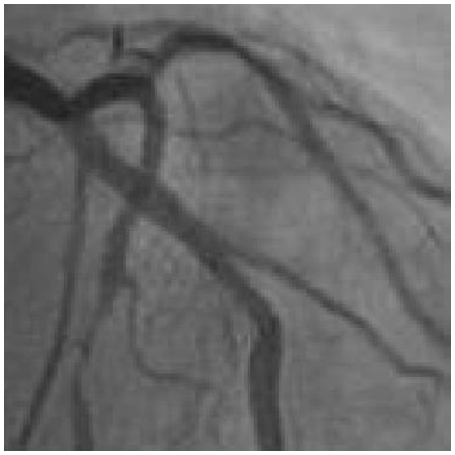

Figure 3.4: Test image used for edge detection

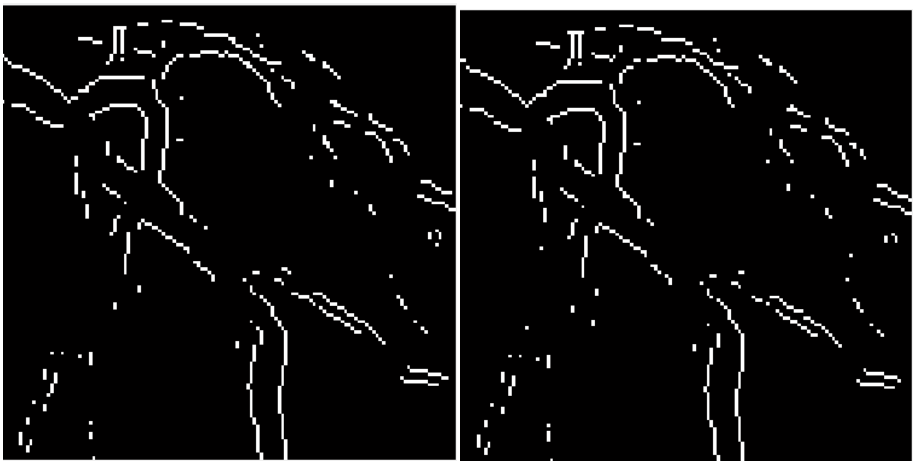

a b

Figure 3.5: Edge responses to test image using (a) Sobel edge detector. (default parameters), (b) Prewitt edge detector (default parameters)

c d

Figure 3.5 (continued): Edge responses to test image using (c) Roberts edge detector (default parameters), (d) Log edge detector

3.3.2.4. Optimization of B-Spline Energy

Energy minimization is a process that evolves the shape of the B-spline snake to the edge of the vessel in our case. There exist various energy optimization methods in the literature. The one that used in this thesis is the Dynamic programming as done in **[11]**.

When B-splines are optimized in this study, normalized energy of the spline is minimized. Normalized energy of the spline is found by dividing the total energy of the spline to the total length of the spline. In this optimization stage, we have no constraints and hence this type of optimization is called as "unconstrained optimization" in the literature. Any method related to unconstrained optimization could also be used instead of Dynamic Programming used in this thesis study.

Energy minimization of the snakes was firstly presented by Kass et al **[97]** and their optimization method was a variational method that uses finite element method. Their optimization method does not guarantee the global minimum solution and estimation of higher order derivatives was a must. After Kass et al, Greedy Algorithms **[98]** were proposed for the energy minimization problem which is an iterative incremental method. This method finds the minimum solution by searching the direction which has a maximum energy decrease.

3.3.2.5. Quantification of Stenosis

In order to quantify the stenosis using 2D projection of a 3D vessel lumen, we need some quantitative parameters indicating the 2D anatomy of the vessel. These parameters are obtained by using the traces which represent the diameter of the vessel. These traces are obtained by matching the contour points located at the opposite edge of the vessel.

Traces used for the quantification of stenosis are obtained in **[11]** by using string matching technique. This technique is based on finding similarity between strings (points on contours in our case) by using three-edit operations: insertion, deletion, substitution. Higher the edit costs, the more dissimilar the strings. Finally, the distance corresponding to the minimum cost operation is found by using dynamic programming. For the comprehensive information about the string matching method, one can apply to **[99]**.

In the proposed algorithm, novel analytical geometry-based methods are proposed to obtain the vessel diameter traces which seek for the following criteria: direct, shortest diameter, similar slope and hybrid. Key idea in this step is to find out the diameters of the vessel successively starting before the stenosis and continuing after the stenosis so that a potential stenosis would be detected.

CHAPTER 4

PROPOSED ALGORITHM

Flow chart of the proposed algorithm is presented in Figure 4.1., which shows every stage of the algorithm in a step by step manner. Since Edge Detection and Spline Fitting parts of the main algorithm consists of further sub-steps and branches inside, they will be detailed in the relevant chapters.

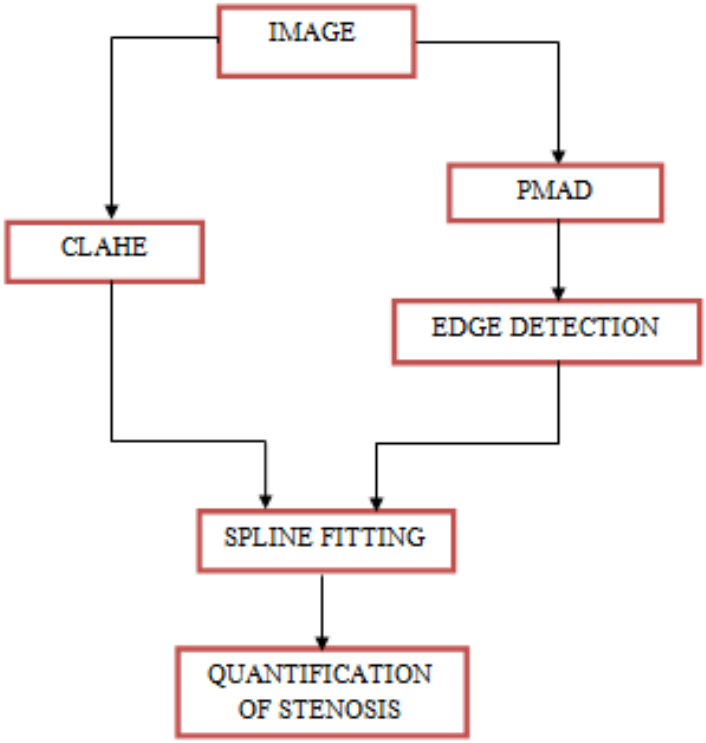

Figure 4.1: Flow diagram of the proposed algorithm

Our proposed method differs from the one in **[11]** in terms of some methods which are tabulated in Table 4.1.

Table 4.1: Differences between our proposed algorithm and **[11]**

Purpose	**[11]**	**Our Method**
Contrast Enhancement	N/A	CLAHE
Getting rid of non-zero DC response of traditional Gabor filter	S-Gabor Filter	Zero Mean Gabor Filter
To obtain well localized external energy image	N/A	Anisotropic Diffusion Filter
To obtain edge response	Gabor Filter	Gabor Filter, Canny Edge Detector
Dynamic Programming Complexity	$O(n^4N)$	$O(n^3 + N.n)$
Spline Fitting	Dynamic Programming	Dynamic Programming, Fast Semi-Automatic Spline Fitting
2D Quantification of Stenosis	String Matching	Analytical Geometry

4.1. Contrast Limited Adaptive Histogram Equalization (CLAHE)

Since images obtained from X-ray angiography generally suffer from poor and variable contrast problem (as shown in Figure 4.2), CLAHE is a good and popular remedy for contrast enhancement compared to standard histogram equalization method.

Advantage of CLAHE over usual adaptive histogram equalization (AHE) method is that it does not over amplify the noise as AHE does. Images in Figure 4.3 shows how CLAHE result is superior than traditional HE result.

CLAHE is not a critical part of our main 2D QCA algorithm; it is used only for assisting the user while initializing the splines around the arteries in poor contrast regions as shown in Figure 4.4.

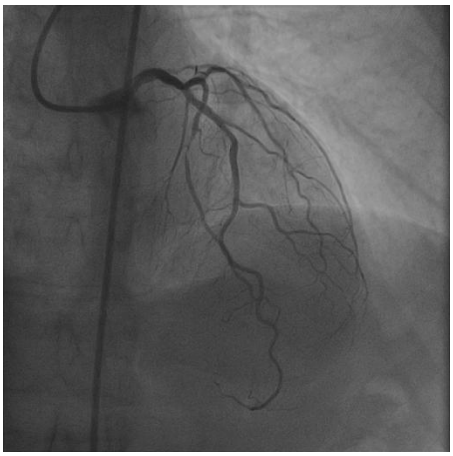

Figure 4.2: Test image

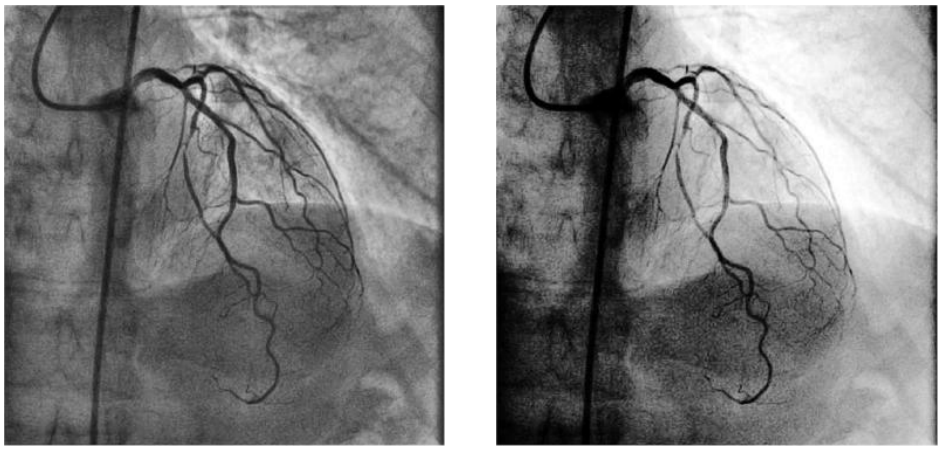

a b

Figure 4.3: (a) CLAHE applied to test image, (b) Classical histogram equalization method applied to test image

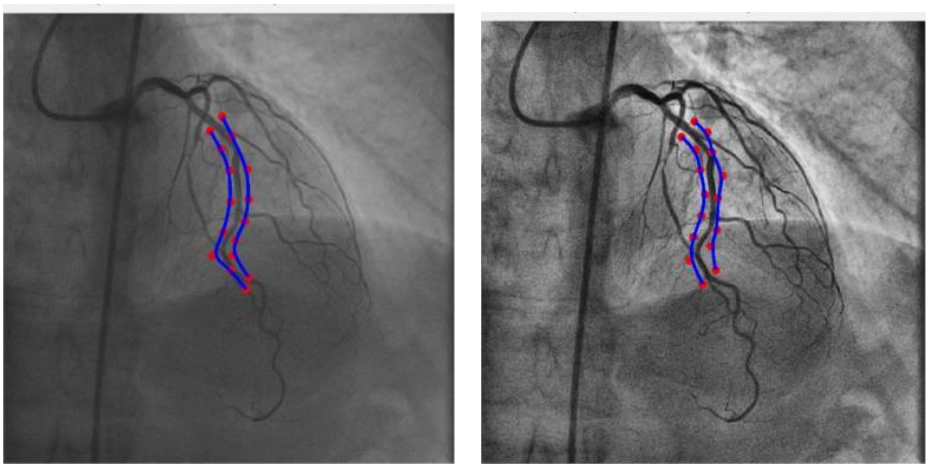

a b

Figure 4.4: (a) Image and initialized spline, (b) CLAHE image and initialized spline.

4.2. Perona-Malik Anisotropic Diffusion (PMAD)

Anisotropic diffusion was firstly proposed by Perona-Malik **[38]** and they presented this approach as an analogy to the heat equation. Heat equation is known as the partial differential equation, which describes distribution and diffusion of heat in an environment over time. As time passes, warmer part of an object gets gradually colder and colder part of the object gets warmer till all parts of the object reach the same temperature. Perona and Malik formulated the smoothing problem in the scope of heat equation aiming that heat diffusion is restricted into a specific area. Unlike the traditional smoothing techniques (i.e. Gaussian filter) which smooths the whole image including edges, anisotropic diffusion smooths the image, while preserving edges. This was the main difference and contribution of Perona and Malik.

After Perona-Malik, anisotropic filters started to be used widely in various forms and different applications as an edge detector **[39] [40] [41]**. Although the most widely used anisotropic diffusion scheme is the explicit scheme, very different schemes exist in literature to increase the efficiency, and widening the numerical stability limits. These alternative schemes are semi-implicit schemes and additive operator splitting schemes (AOS) as presented in **[42]**. For our work, we have chosen to use explicit scheme of Perona-Malik anisotropic diffusion (PMAD) in its stable time steps. For a more comprehensive review on anisotropic diffusion for edge detection techniques, **[43]** can be visited.

General diffusion equation in continuous form can be written as follows:

$$\frac{\partial \phi(r,t)}{\partial t} = \nabla.[D(\phi,r).\nabla\phi(r,t)] \tag{4-26}$$

where $\phi(r,t)$ is the density of the diffusing material at location r and time t, $D(\phi,r)$ is the collective diffusion coefficient for density ϕ at location r. If $D(\phi,r)$ is chosen as 1, resulting diffusion will be a linear diffusion.

In the image processing perspective, $\phi(r,t)$ is replaced with u, which represents the image density to be diffused. Furthermore, in Perona-Malik diffusion, diffusion coefficient function $D(\phi,r)$ will be replaced by a function which is a decreasing function of the image gradient. As the image gradient increases, which is an indicator of an edge, diffusion coefficient decreases and less diffusion occurs in that region. In regions where image gradient is low, diffusion coefficient is higher and causes high

diffusion in that region. This variable property of diffusion function with respect to image gradient gives Perona-Malik Anisotropic Diffusion the power of selective smoothing. Thanks to this property, while smoothing is achieved where it is needed, edge features of the image are preserved. While Equation 4-27 is called as Perona-Malik type diffusion function and Equation 4-28 is called as Charbonnier type diffusion function.

$$D(\phi, r) = g(|\nabla u_\sigma|) = e^{-\frac{|\nabla u_\sigma|^2}{\lambda^2}} \tag{4-27}$$

$$D(\phi, r) = g(|\nabla u_\sigma|) = \frac{1}{1+\frac{|\nabla u_\sigma|^2}{\lambda^2}} \tag{4-28}$$

In both of these functions, λ controls the sensitivity to edges in the image.

Rewriting continuous form of diffusion equation 4-26 for image u:

$$\frac{\partial u}{\partial t} = \nabla.[g(|\nabla u_\sigma|).\nabla u)] \tag{4-29}$$

$$= g(|\nabla u_\sigma|)\,.\nabla^2 u \tag{4-30}$$

$$\frac{\partial u}{\partial t} = g(|\nabla u_\sigma|).(\frac{\partial^2 u}{\partial x^2} + \frac{\partial^2 u}{\partial y^2}) \tag{4-31}$$

Expressing the formula (4-31) in discrete form:

$$\frac{u_{i,j}^{n+1} - u_{i,j}^n}{\Delta t} = g(|\nabla u_\sigma|).(\frac{u_{i,j-1}^n + u_{i,j+1}^n + u_{i+1,j}^n + u_{i-1,j}^n - 4u_{i,j}^n}{h^2}) \tag{4-32}$$

$$u_{i,j}^{n+1} = u_{i,j}^n + \left(\frac{\Delta t}{h^2}\right) g(|\nabla u_\sigma|).(u_{i,j-1}^n + u_{i,j+1}^n + u_{i+1,j}^n + u_{i-1,j}^n - 4u_{i,j}^n) \tag{4-33}$$

Discrete form of diffusion equation is obtained as in equation 4-33. With this discrete form, PMAD can be implemented in any development environment in an iterative manner.

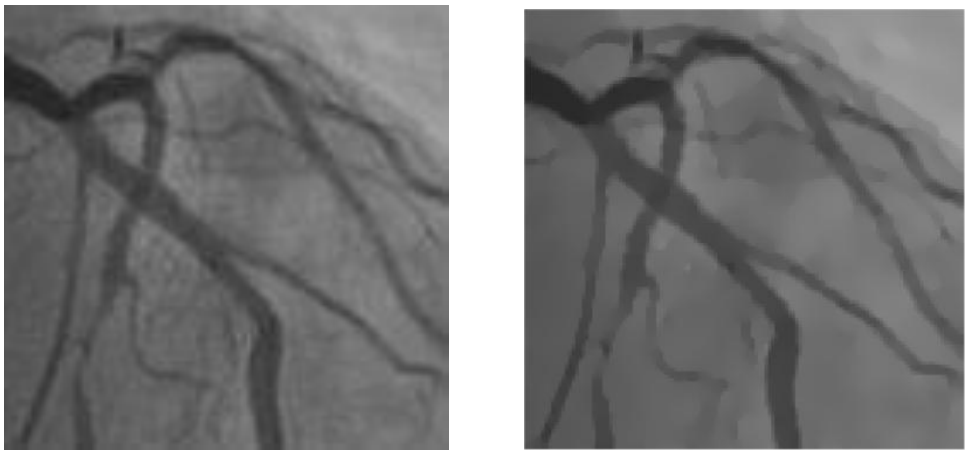

a b

Figure 4.5: (a) Original image, (b) Anisotropic diffused image.

After anisotropic diffusion is applied to the original image as in Figure 4.5, tuned Gabor filters having different orientations are applied. By combining responses of each Gabor filter, a composite energy field is obtained as shown in Figure 4.6 (b). This composite energy will then be used as an external energy function to optimize the B-splines.

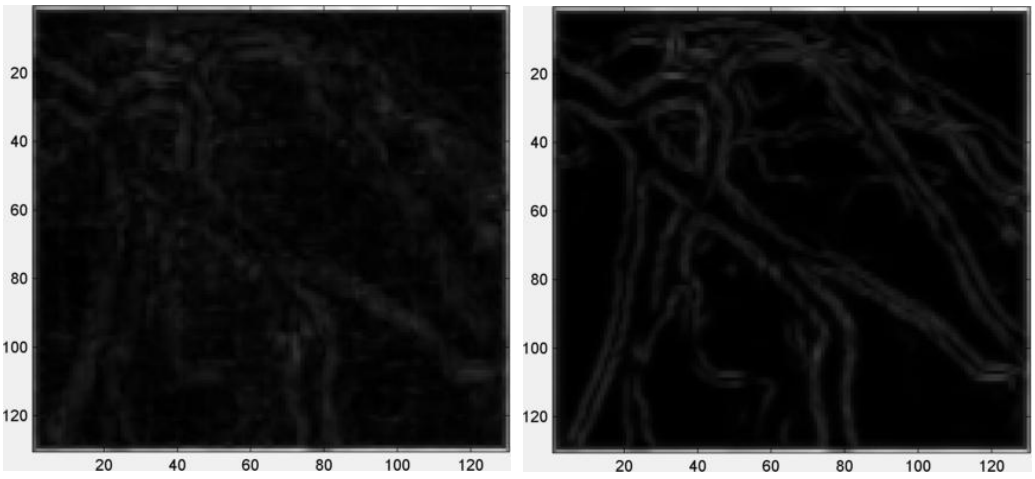

a b

Figure 4.6: (a) Composite energy field using pure Gabor filter responses, (b) Composite energy field constructed after the application of Anisotropic diffusion and Gabor filter to original image.

Application of Gabor filters directly to the X-Ray Angiography images does not give well-localized vessel edges due to exhaustive noise existing in angiographic images. Since Gabor filter-applied images are used as external energy function for B-splines, quality of Gabor filtered images play important role on the optimization of splines. To eliminate the noise in the background and obtain well-localized vessel edges, we have applied Perona-Malik Anisotropic Diffusion just prior to the application of Gabor filters. Perona-Malik Anisotropic Diffusion is selected, since it denoises the the image while preserving edge features.

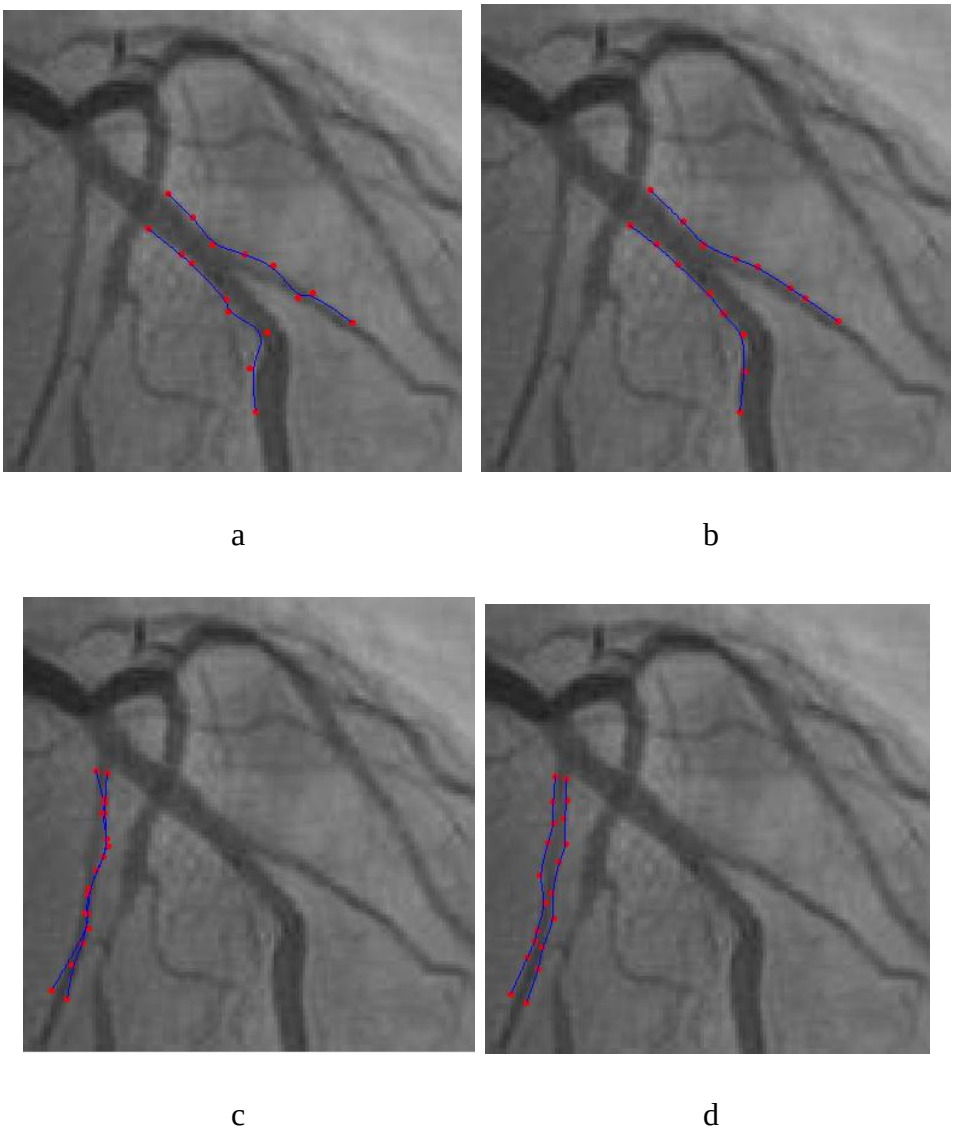

a b

c d

Figure 4.7: (a), (c), (e) are the optimized splines using only Gabor filter response; (b), (d), (f) are the optimized splines using Anisotropic Diffusion plus Gabor filter response.

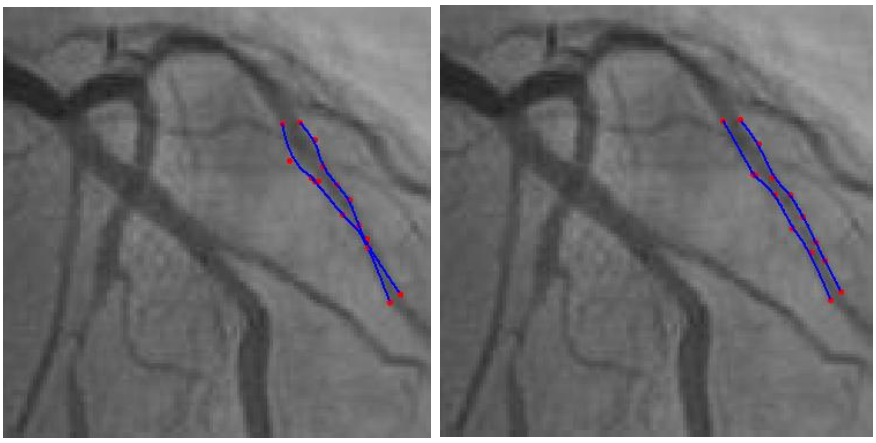

e f

Figure 4.7 (continued): (a), (c), (e) are the optimized splines using only Gabor filter response; (b), (d), (f) are the optimized splines using Anisotropic Diffusion plus Gabor filter response.

As can be seen in the above experiments whose results are shown in the Figures 4.7 (a), (b), (c), (d), (e), (f), localization of B-Spline snakes to the edge of the vessels are better in Anisotropic diffusion applied images as shown in Figure 4.7 (b), (d), (f). Application of Anisotropic diffusion prior to Gabor filtering is a novelty of this thesis and it is clear from these experiments that this method increases the conformation of the spline to the vessel borders and increases the contour extraction quality performance.

4.3. Edge Detection

In this step of the algorithm, there are two possible ways of extracting edge features of vessel structures namely, Gabor filter and Canny edge detector as shown in Figure 4.8. User is free to choose either of the two methods depending upon the advantages and disadvantages which are widely discussed in Section 4.3.7. Result of this step is the edge feature image which will be used in the spline fitting part as an external energy function.

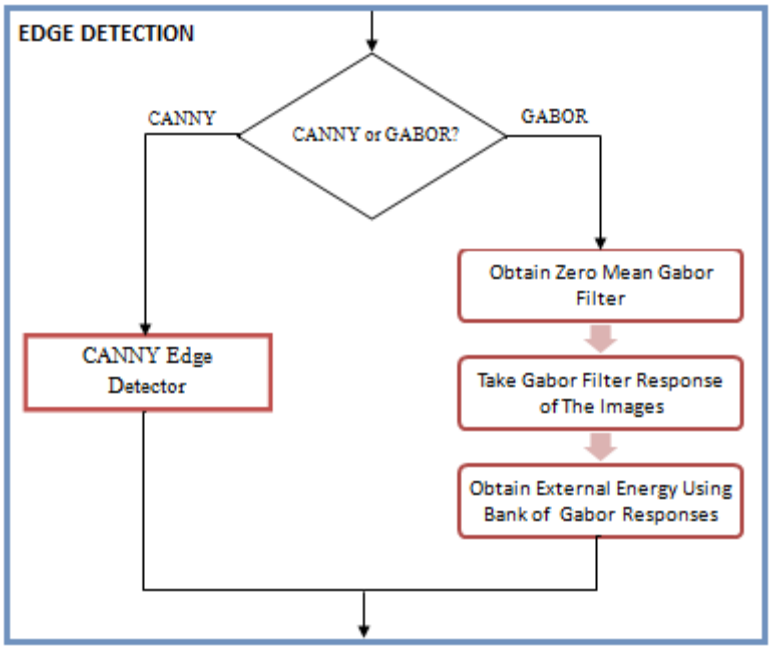

Figure 4.8: Edge Detection part of the main algorithm

4.3.1. Gabor Filters

Gabor filter is very popular in image processing and computer vision research areas since it is very useful in localizing edge and line features of an image in both frequency and spatial domain. This filter takes its name from Gabor who is the first one proposing 1D Gabor function in 1946 as a multiplication of a Gaussisan function with a sinusoid **[1]** as seen in Figure 4.9.

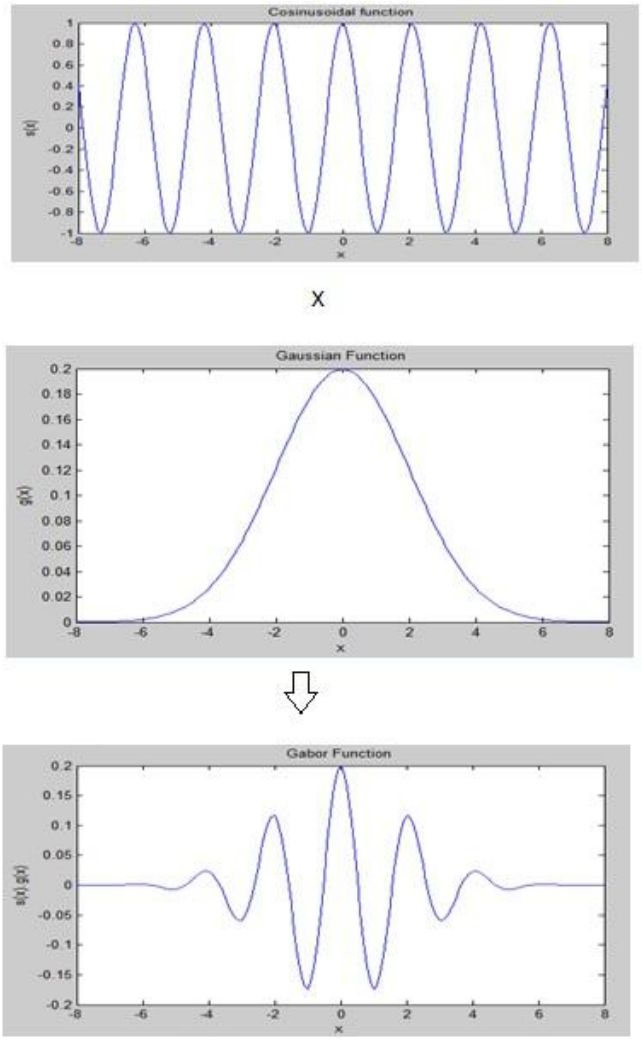

Figure 4.9: Gabor function and its cosinusoidal and Gaussian components

2D Gabor filters, however, were firstly introduced by Daugman in 1980 in his study whose subject is orientation and spatial-frequency selective properties of neuron cells in the visual cortex of the brain **[2]**. A 2D Gabor function can be simply defined as a harmonic oscillator whose components are a sinusoidal plane wave having a particular frequency and orientation and a Gaussian envelope **[2]**.

After Daugman further elaborated the 2D Gabor function mathematically in 1985, it has been used in many areas such as retinal vessel extraction and segmentation **[3], [4]**; fingerprint image enhancement **[2], [5]**; dorsal hand vein recognition **[6]**; palmprint recognition **[7]**; iris recognition **[9]** and edge detector **[8]**.

4.3.1.1. 1D Gabor Filter

1D Gabor filter is defined as follows **[1]**:

$$G(x) = e^{\frac{-x^2}{2\sigma^2}}.e^{j2\pi fx} \tag{4-1}$$

Using Euler's Formula:

$$e^{j\theta} = \cos(\theta) + jsin(\theta) \tag{4-2}$$

$$G(x) = e^{\frac{-x^2}{2\sigma^2}}.[\cos(2\pi fx) + j\sin(2\pi fx)]$$

$$G(x) = e^{\frac{-x^2}{2\sigma^2}}.\cos(2\pi fx) + j.e^{\frac{-x^2}{2\sigma^2}}.\sin(2\pi fx) \tag{4-3}$$

As can be seen from the formula, Gabor function has both real and imaginary parts.

This filter can be separated as ODD and EVEN Gabor functions as follows:

$$S(x) = e^{\frac{-x^2}{2\sigma^2}}.\sin(2\pi fx) \tag{4-4}$$

$$C(x) = e^{\frac{-x^2}{2\sigma^2}}.\cos(2\pi fx) \tag{4-5}$$

where $S(x)$ is the odd anti-symmetric function and $C(x)$ is the even symmetric function.

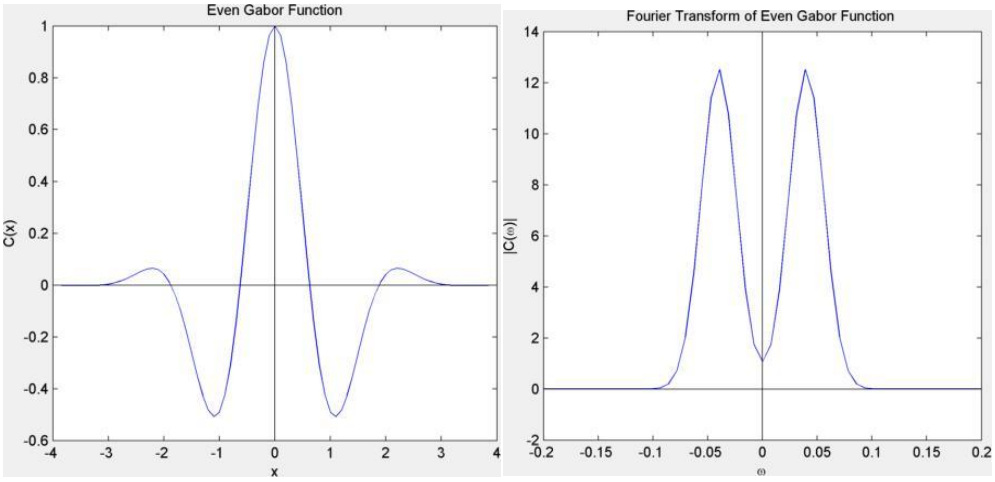

a b

Figure 4.10: (a) EVEN Gabor function. (b)Fourier transform of even Gabor function.

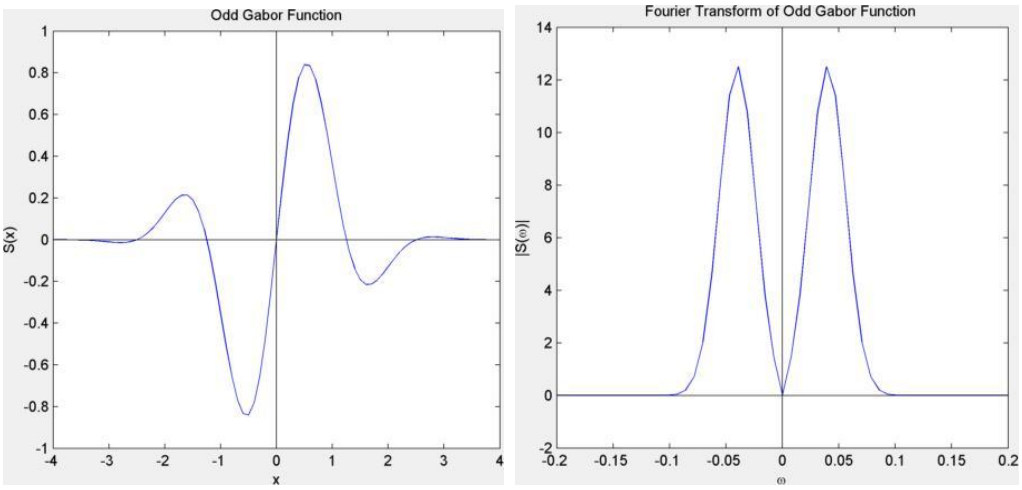

a b

Figure 4.11: (a) ODD Gabor function, (b) Fourier transform of ODD Gabor function (magnitude)

Although Fourier transform of the ODD part of the Gabor function has zero DC response as seen in Figure 4.11 (b), Fourier transform of the EVEN Gabor function has non-zero DC response as seen in Figure 4.10 (b).

4.3.1.2. S-Gabor Filter

To eliminate non-zero DC response of the Even Gabor function, [11] proposes S-Gabor filters. Non-zero DC response is a problem for the enhancement of small vessels and sharp edges of large vessels. Using S-Gabor filters presents a solution for this problem by multiplying argument of sine function by an additional factor, which makes a sweep to lower frequency in the sine and cosine functions. Purpose of this additional factor ($\Psi(x)$) is to increase the wavelength of the sine and cosine functions as distance from the origin increases and to add weight to negative side lobes of the even filter. Increase of the negative side lobes of the function adds additional negative area and hence causing zero integral.

$$S(x) = e^{\frac{-x^2}{2\sigma^2}}.\sin(2\pi fx\Psi(x)) \quad (4\text{-}6)$$

$$C(x) = e^{\frac{-x^2}{2\sigma^2}}.\cos(2\pi fx\Psi(x)) \quad (4\text{-}7)$$

where,

$$\Psi(x) = k.\, e^{-\lambda(\frac{x}{\sigma})^2} \tag{4-8}$$

To be able to construct an S-Gabor filter, constants in the new factor must be determined one by one.

k *:* relative contribution of the frequency sweep

λ *:* rate of the frequency sweep

Parameters k, λ, σ, f must be selected such that integral over the length of the even filter is zero. (i.e. zero DC response.)

4.3.1.3. Zero-Mean 2D Gabor Filter

If 2D Gabor filters are directly used, they will have a slight DC response for regions having uniform luminance (DC) **[6]**. However, our purpose is to have a non-zero filter response for only edge features of the image. While odd part (sinusoid) of the Gabor function gives no response to uniform luminance region, even part (cosinusoid) of the Gabor function gives non-zero response which is undesired. Since this non-zero DC response would be detrimental to enhancement of small vessels and sharp edges of large vessels, it must be removed **[10]**.

Instead of using S-Gabor filters, which require some design parameters (i.e. k, λ, σ, f) to get zero integral over the even Gabor function, we preferred to use Zero-mean Gabor filters **[6], [7]** to make Gabor filter to give no response for uniform regions, which is defined as follows:

$$G^{ZM}{}_{\sigma_x,\sigma_y,f,\theta}(x,y) = G_{\sigma_x,\sigma_y,f,\theta}(x,y) - \frac{\sum_{i=-N}^{N}\sum_{i=-N}^{N} G_{\sigma_x,\sigma_y,f,\theta}(i,j)}{(2N+1)^2} \tag{4-9}$$

where (2N+1) is the one dimension of a square-sized filter.

While mean of the ODD Gabor function is zero, mean of the EVEN Gabor function is non-zero. This was the previously mentioned problem named as non-zero DC

response. By simply subtracting the mean of the filter from itself, we can easily obtain a zero-mean Gabor filter.

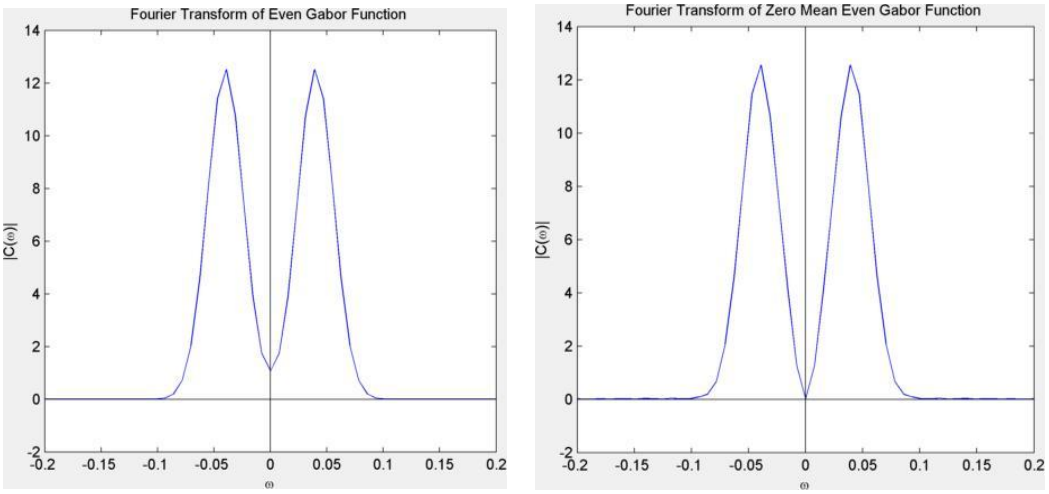

a b

Figure 4.12: (a) Fourier transform of EVEN Gabor function (magnitude), (b) Fourier transform of Zero-mean EVEN Gabor function

As can be seen from Figure 4.12, while magnitude of the frequency response (Fourier Transform) of Even Gabor function is non-zero at zero frequency, Zero-mean Even Gabor function has zero response at zero frequency. Results shown in Figure 4.12 shows that, Zero-mean Gabor filter is a remedy for non-zero DC response of Gabor filters.

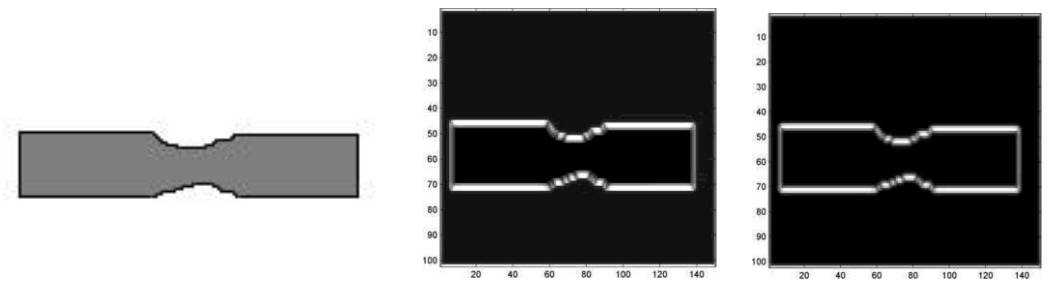

(a) (b) (c)

Figure 4.13: (a) Test image, (b) Gabor filter response of test image, (c) Zero-mean Gabor filter response of test image

Comparing Figure 4.13 (b) to Figure 4.13 (c), Gabor filter gives non-zero response to uniform luminance region (white region) as seen gray in Figure 4.13 (b). However, the same region is seen as black in Figure 4.13 (c) showing that Zero-mean Gabor filter gives no response to uniform luminance region (white region in Figure 4.13 (a))

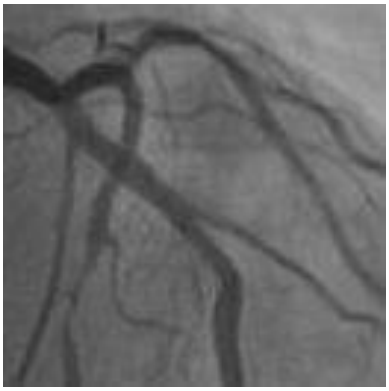

Figure 4.14: Test image

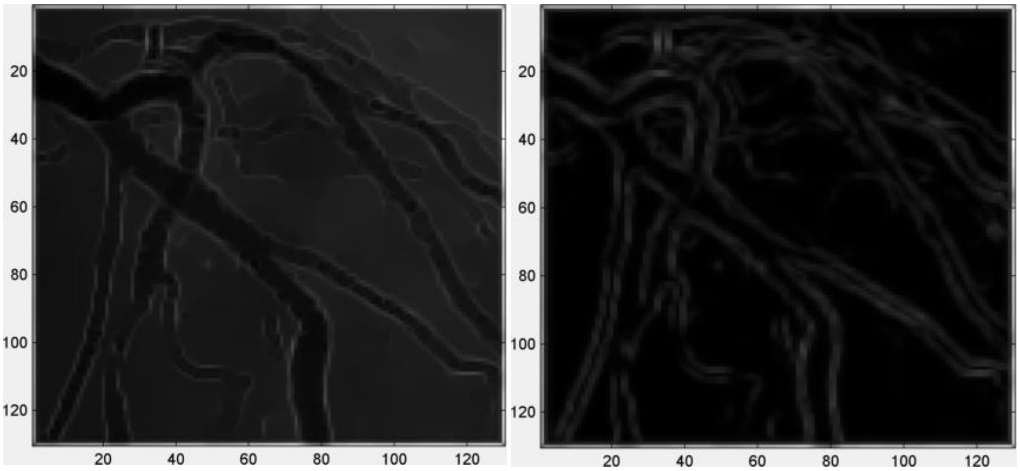

a b

Figure 4.15: (a) Composite response obtained using Gabor filter having non-zero DC response, (b) Composite response obtained using Zero-mean Gabor filter

The same experiment done for Figure 4.13 (a) is also repeated for real angiographic image shown in Figure 4.14. Both Gabor filter and Zero-mean Gabor filter is applied to test image respectively and corresponding results are obtained as shown in Figure 4.15. Zero-mean Gabor filter gives no response to uniform luminance region. Black regions in Figure 4.15 (a) show this non-zero response. Black regions in Figure 4.15

(a) are displayed as gray in Figure 4.15 (b), which shows the non-zero DC response of Gabor filter.

4.3.1.4. 2D Gabor Filter

2D Gabor filter is obtained by simply multiplying 1D Gaussian kernel by another Gaussian kernel in the y direction.

$$\mathrm{G(x,y)} = e^{-\frac{x'^2}{2\sigma_x{}^2}-\frac{y'^2}{2\sigma_y^2}}.e^{j2\pi f\,\mathrm{x}'} \tag{4-10}$$

using again Euler's formula,

$$G_{\sigma_x,\sigma_y,f,\theta}(x,y) = e^{-\frac{x'^2}{2\sigma_x{}^2}-\frac{y'^2}{2\sigma_y^2}}.\cos(2\pi\mathrm{fx}') + j.e^{-\frac{x'^2}{2\sigma_x{}^2}-\frac{y'^2}{2\sigma_y^2}}.\sin(2\pi f\mathrm{x}') \tag{4-11}$$

where,

$$x' = x.cos(\theta) + y.sin(\theta) \tag{4-12}$$

$$y' = -x.sin(\theta) + y.cos(\theta) \tag{4-13}$$

A single Gabor filter enhances edge and line features of an object having a specific scale and orientation. Therefore, a bank of these filters having different orientations or scales must be used. In our case, we have chosen a bank of Gabor filters having a fixed scale and variable orientation which spans the 180 degrees around the image. In this way, we have edge information of the object from every angle.

In Figure 4.16, 2D Gabor filter bank is seen. In each row, scale of the filter is constant but orientation of the filter is changing from 0 to 180 degrees. In each column however, orientation of the filter is constant but the scale of the filter is increasing. In Figure 4.17, corresponding magnitude responses of Gabor filters shown in Figure 4.16 are displayed.

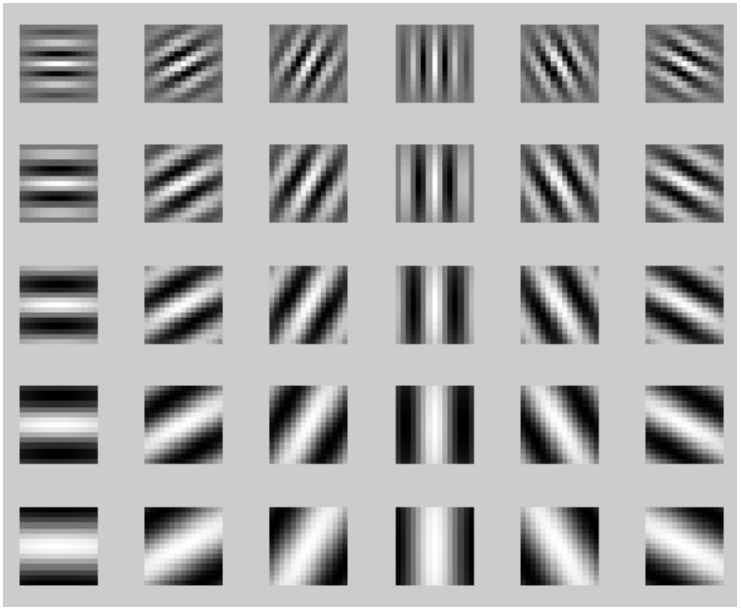

Figure 4.16: Real parts of Gabor filter bank with 6 orientations and 5 scale factors (Convolution mask size is 15x15)

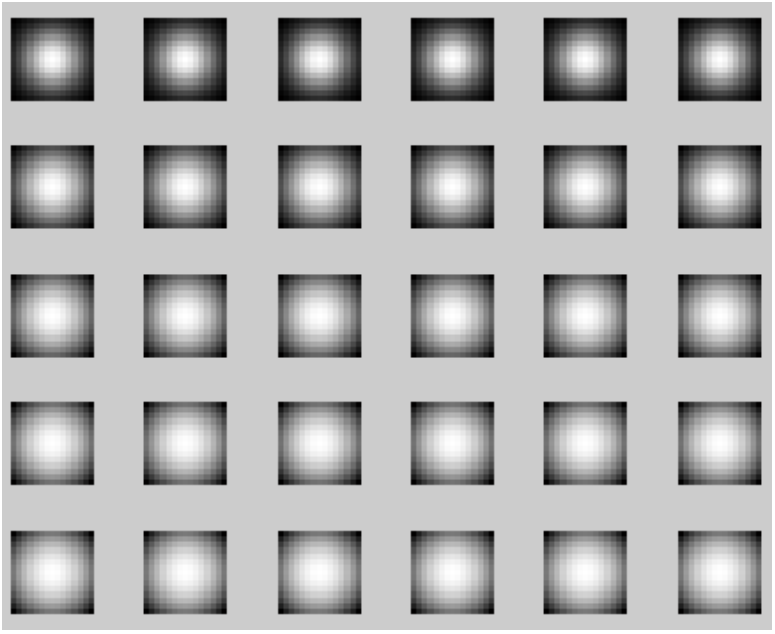

Figure 4.17: Magnitudes of Gabor filter bank with 6 orientations and 5 scale factors (Convolution mask size is 15x15)

For our purpose, we need a bank of Gabor filters which have a fixed scale but varying orientations (as shown in Figure 4.19) to be able to have edge information of the vessels from different angles. When Gabor filter bank in Figure 4.19 is applied

to test image in Figure 4.18, resultant responses are obtained as shown in Figure 4.20.

Figure 4.18: Input Image

Figure 4.19: Gabor filter bank having fixed scale, but different orientations.

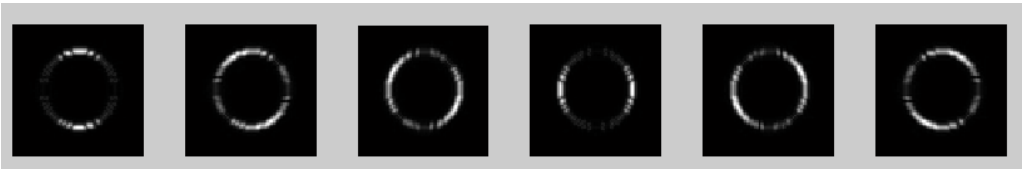

Figure 4.20: Gabor filtered images whose edges are detected depending on the orientation of the filter. (6 orientation)

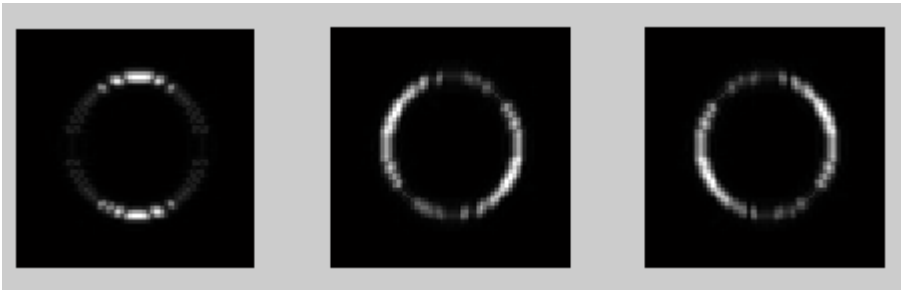

Figure 4.21: Gabor filtered images whose edges are detected depending on the orientation of the filter. (3 orientation)

If a Gabor filter bank having 3 elements were applied to synthetic test image in Figure 4.18, resultant response would be as in Figure 4.21. If the same Gabor filter bank is applied to real angiographic image shown in Figure 4.14, resultant Gabor

responses will be in Figure 4.22. These Gabor responses shown in Figure 4.22 will then be used in the next chapter to construct the composite energy field.

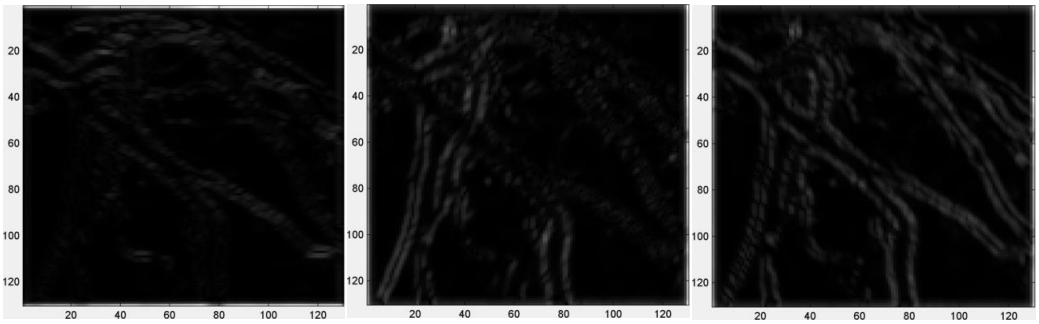

a b c

Figure 4.22: (a) Gabor filter response having the first orientation, (b) Gabor filter response having the second orientation (c) Gabor filter response having the third orientation.

4.3.1.5. Energy Field Obtained From Gabor Filter Responses

Energy field is obtained by convolving the image I with a Gabor filter of orientation θ ($G(\theta)$) and taking the vector magnitude as follows:

$$E(\theta) = \sqrt{|G(\theta) * I|^2} \tag{4-14}$$

Energy is a function of θ, meaning that energy of the image for a specific orientation is calculated. However, what we need is the energy field for each orientation obtained through convolving a bank of Gabor filters having different orientations. If the maximum responses of each energy field at each point of the image is accumulated (collected), a composite energy field is constructed which has all enhanced edge and line features of the image. This composite energy field (obtained by using Equation 4-15) then will be used as external forces that attract the energy minimizing snakes onto the image contour.

$$\epsilon(x, y) = max_{\theta} E(x, y, \theta) \tag{4-15}$$

When Gabor responses obtained in Figure 4.20 are used to construct a composite energy field, resultant image is obtained as in Figure 4.23. If Gabor responses obtained in Figure 4.22 are used, resultant image is obtained as in Figure 4.24.

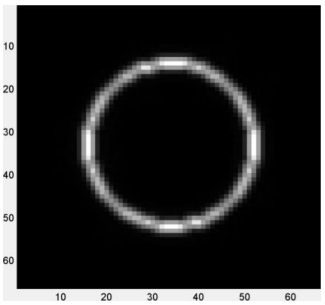

Figure 4.23: Composite energy field obtained using 6 Gabor filters having different orientations.

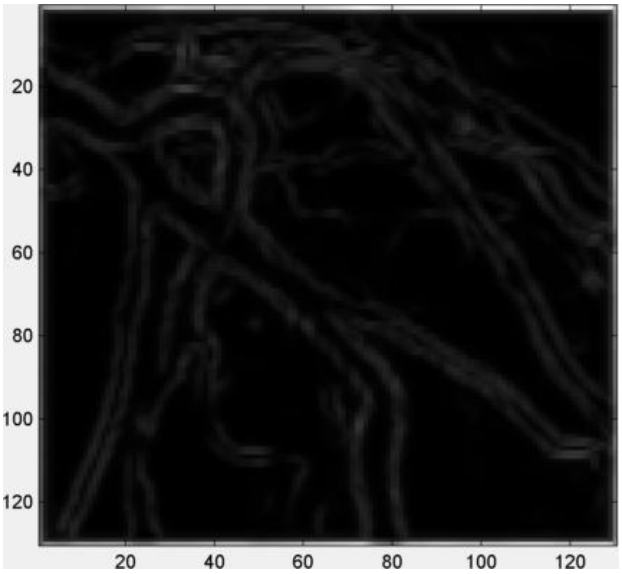

Figure 4.24: Constructed composite energy using the Gabor responses obtained in the previous section.

4.3.2. Canny Edge Detector

As an alternative method to Gabor filter, Canny edge detector could be used as an external energy function for spline optimization scheme. Canny edge detector is an alternative of three steps of the other branch of edge detection part of the algorithm as shown in Figure 4.25. While output of the Gabor filter is floating point numbers, output of the Canny edge detector is a binary image. Therefore, Canny edge detector has discrete edge responses and is prone to discretization errors. However, Canny edge detector is slightly faster than the Gabor filter; since application of many differently oriented Gabor filters takes more time compared to Canny.

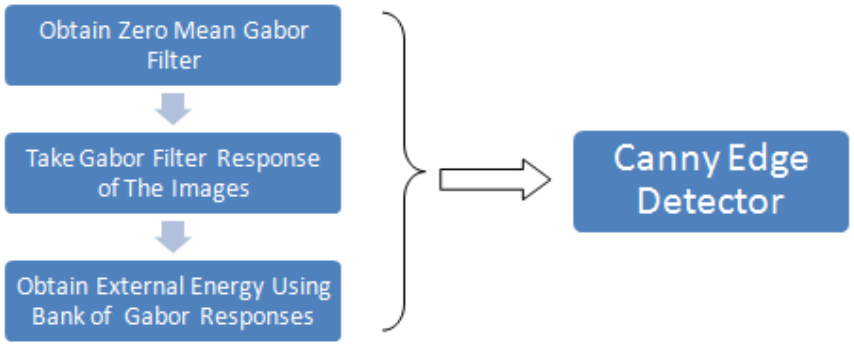

Figure 4.25: Canny edge detector is an alternative to Gabor filter steps.

Noise and contrast characteristics of X-ray angiographic images vary widely. Although Canny edge detector gives good response on the real angiographic images as shown in Figure 4.26 (a) if the noise in the original image is not much, its response on a noisy synthetic image and real noisy angiographic image is not good enough compared to Gabor filter as shown in Figure 4.27 and Figure 4.28. As shown in Figures 4.27 and 4.28, Gabor responses are better than Canny responses for noisy images. However, if PMAD were applied prior to the Canny edge detector, resultant edge response would be better as shown in Figure 4.29 than Figure 4.28 (b).

a b

Figure 4.26: (a) Canny edge detector (default MATLAB parameters), (b) Gabor filter after PMAD is applied

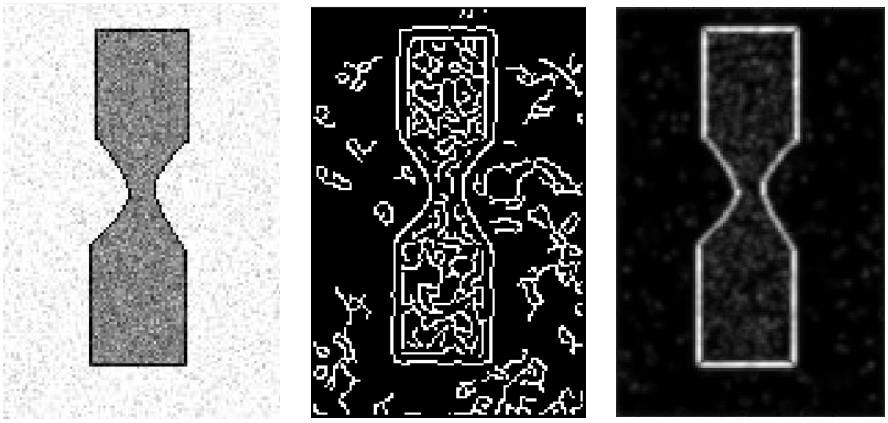

a b c

Figure 4.27: (a) Noisy synthetic image, (b) Canny applied image, (c) PMAD and Gabor applied image

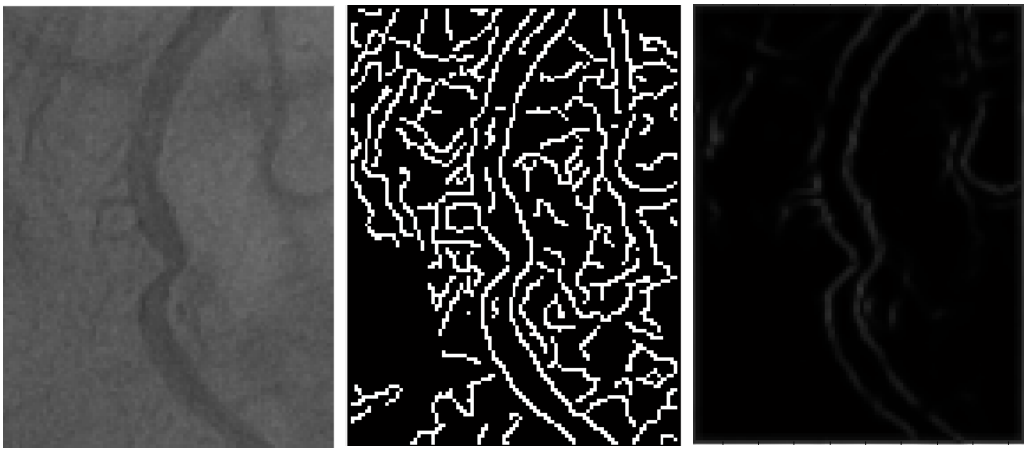

a b c

Figure 4.28: (a) Test image, (b) Canny-applied image, (c) PMAD and Gabor applied image.

Figure 4.29: PMAD is applied prior to the application of Canny edge detector.

While Canny performs well in coarse vessel structures, it under performs in the fine vessels compared to Gabor filter. This result can be drawn easily when the following two examples are examined. In Figure 4.30 (a), two splines are initialized and they are optimized by using Gabor energy field (Figure 4.30 (c)) and Canny edge response (Figure 4.30 (b)). By looking at the IMP metrics, one can easily conclude that splines are optimized better when Canny edge response is used; since the higher the IMP metric, the better the optimization (For detailed explanation about IMP metric, Section 5.1 could be visited). However in Figure 4.31, which has fine vessel structure compared to the previous one, splines are optimized better when Gabor energy response is used, since IMP values are higher when Gabor response is used.

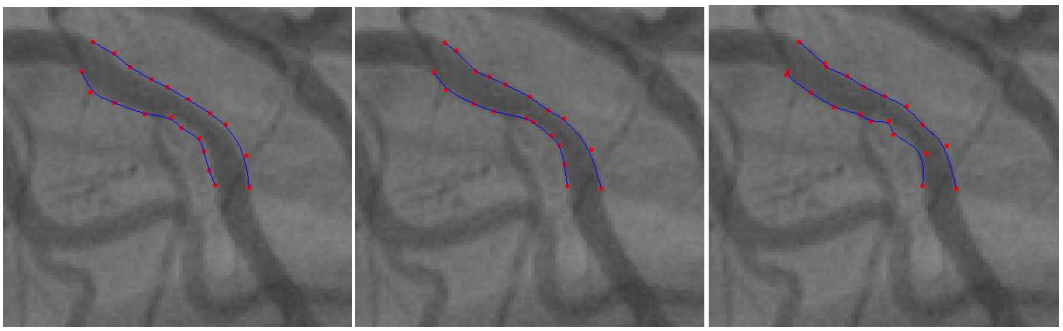

a b c

Figure 4.30: (a) Initial spline, (b) Optimization with Canny (IMP_left = 0.9634, IMP_right = 0.9838), (c) Optimization with Gabor (IMP_left = 0.9113, IMP_right = 0.9781)

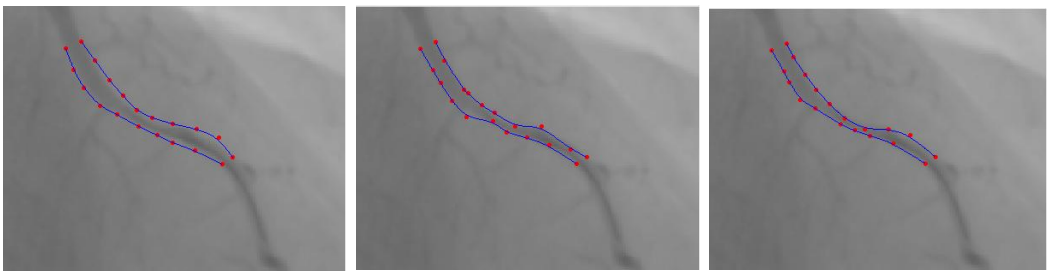

a b c

Figure 4.31: (a) Initial splines, (b) Optimization with Canny (IMP_left = 0.9226, IMP_right = 0.9417), (c) Optimization with Gabor energy field, (IMP_left = 0.9625, IMP_right = 0.9714)

4.4. Spline Fitting

In this step of the algorithm, image obtained in the edge detection part is used as external energy function and CLAHE-enhanced image is used when splines or initialized as a visual aid to the user. There are two possible ways of fitting B-splines to the vessel borders. User is free to choose either of these two methods. First method is initializing splines manually and optimizing them using dynamic programming. The other method is fitting splines by using only a few control points put by the user which is called as Semi-automatic Spline Initialization and Fitting.

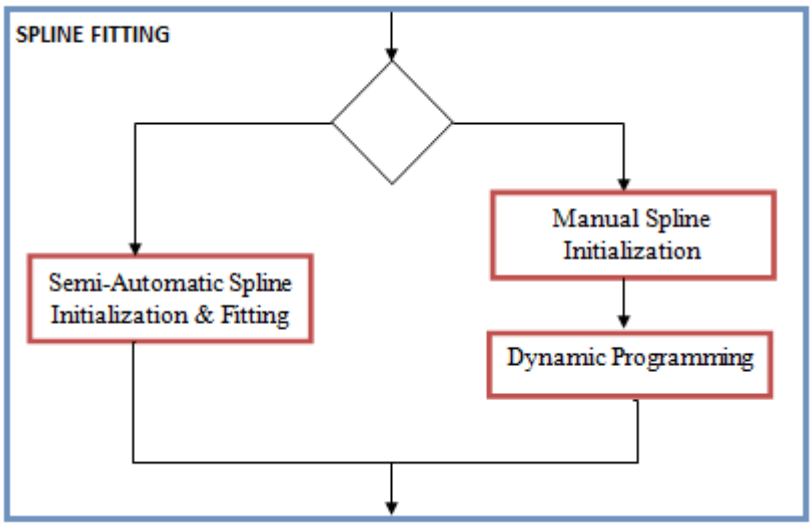

Figure 4.32: Spline fitting part of the main algorithm.

4.4.1. B-Spline Snakes

A snake is a deformable curve model which moves through the edges and get the shape of the edges in the image according to external forces applied by the image. While external forces attract the snake to the nearest edge, snake tries to keep as smooth as possible to satisfy internal shape constraints. Therefore, both external forces and internal smoothness constraints play crucial role on the deformation and final shape of the snake. As can be deduced, snake energy consists of both external and internal energies.

$$\varepsilon_{snake} = \varepsilon_{external} + \varepsilon_{internal} \quad (4\text{-}16)$$

$$\varepsilon_{snake} = \int_0^l \varepsilon_{image}[v(s)]ds + \int_0^l [\alpha|v_s(s)|^2 + \beta|v_{ss}(s)|^2]ds \quad (4\text{-}17)$$

where, $v(s)$ is the snake curve having a length of l, α and β are constants.

B-splines are the most suitable way of describing a parametric curve and its deformation due to the following reasons **[11]**:

- Continuity and smoothness constraints of the curve are inherently satisfied and no need for internal smoothness constraint.
- B-spline snake is defined using a few control points.
- Displacement of an individual control points has no effect on the other control points.

A B-spline curve can be in any order, however most often used B-splines are quadratic (second order) and cubic (third order). As the order of the spline increases, shape complexity and computational cost increases. Therefore, selection of the spline order is a design parameter which is a trade of between shape complexity of the spline and computational cost. We have chosen the piecewise cubic splines as in paper **[11]**.

For a B-spline to take the shape of the desired edge features, following energy term must be minimized (internal energy is not valid for a B-spline):

$$\varepsilon_{snake} = -\int_0^l \varepsilon[v(s)]ds \quad (4\text{-}18)$$

Equation (4-18) represents the Integration of the external energy over the entire length of the spline.

For a piecewise cubic spline, energy term in equation (4-18) can be rewritten in discrete form as follows:

$$\varepsilon_{snake} = \varepsilon_0(p_0, p_1, p_2, p_3) + \varepsilon_1(p_1, p_2, p_3, p_4) + \ldots + \varepsilon_{N-4}(p_{N-4}, p_{N-3}, p_{N-2}, p_{N-1}) \quad (4\text{-}19)$$

Where, p_i is the control point, N is the total number of control points and ε_n is the energy of the n^{th} span.

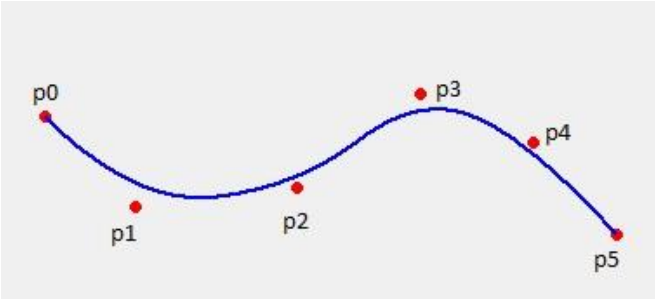

Figure 4.33: B-spline consisting of 6 control points

Point p_0-p_3 is the first span, p_1-p_4 is the second, p_2-p_5 is the third span. Energy and shape of a span is determined by only 4 control points of that span. Summing the energies off all successive spans, total energy of the spline is found. Then, by dividing the total energy of a spline to its length normalized energy of the spline is found and this normalized energy is used as the energy of the spline in the optimization stage.

In the optimization stage, each control point is allowed to navigate in 9 pixel window (3x3) to search for the best conformation of a span except the first and last control point. These two control points are fixed throughout the optimization scheme so that initialized spline does not migrate away from the edge of the vessels.

4.4.2. Dynamic Programming

Dynamic programming is a method for handling complex problems by dividing them into simpler sub problems (divide and conquer approach). Advantage of solving sub problems is to reduce the number of calculations and hence increase the performance of the algorithm.

In the paper **[35]**, dynamic programming is used to solve variational problems some of which are optical flow computation, shape from shading and energy-minimizing active contour models. This paper chooses dynamic programming since it ensures global optimality of the solution, it provides numerical stability and its structure is suitable to pose hard constraints which enforce the behavior of the solution **[35]**. These characteristics of dynamic programming have a great importance especially for energy minimization problems.

Since dynamic programming provides good optimization results and allows more efficient algorithms, its use is widespread in many research areas in any form and variety. In **[36]**, an extended version of dynamic programming, which is called as Loopy Dynamic Programming (LDP), is used in an image parsing problem to manage large search space efficiently. Another form of dynamic programming, which is called as multi-dimensional dynamic programming, is used for surface fitting problem **[37]**. In this paper, 4D Dynamic Programming is used (4D-DP) is used to obtain best surface fit and it is extended versions (i.e. 5D-DP and 7D-DP) are presented to be able to find global optimum in a discrete domain.

Following example shows how DP reduces the number of calculations and saves time. For example, for a spline having N number of control points, and n possible positions for each control point, there are n^N possible solutions for the next configuration of the control points set (hence spline). However, dynamic programming offers $O(n^4 N)$ number of steps to reach the optimum energy level. Comparing complexities $O(n^N)$ and $O(n^4 N)$, one can conclude that advantage of the dynamic programming is more dominant for control points greater than 4. While complexity increases exponentially in the classical approach ($O(n^N)$), complexity of dynamic programming increases linearly as the control points increases. Since we will use the B-spline to get the shape of complex arteries, number of control points defining a B-spline will be much more than 4 and we will be able to take the advantage and of dynamic programming.

Dynamic programming is used to minimize the total energy of the B-spline (ε_{snake}) and hence optimize it by using the following recurrence relation **[10]**.

$$S_i(p_i,\ p_{i+1},\ p_{i+2}) = \min_{p_{i-1}}\{\varepsilon_{i-1}(p_{i-1}, p_i, p_{i+1}, p_{i+2}) + S_{i-1}(p_{i-1} + p_i + p_{i+1})\} \quad \text{for } i \geq 2 \tag{4-20}$$

and

$$S_1(p_1, p_2, p_3) = \min_{p_0}\{\varepsilon_0(p_0, p_1, p_2, p_3)\} \tag{4-21}$$

To understand the recurrence relation in equations (4-20) and (4-21) better, iteration equations are written as follows:

$$S_1(p_1, p_2, p_3) = \min_{p_0}\{\varepsilon_0(p_0, p_1, p_2, p_3)\} \quad (4\text{-}21)$$

$$S_2(p_2, p_3, p_4) = \min_{p_1}\{\varepsilon_1(p_1, p_2, p_3, p_4) + S_1(p_1, p_2, p_3)\} \quad (4\text{-}22)$$

$$S_3(p_3, p_4, p_5) = \min_{p_2}\{\varepsilon_2(p_2, p_3, p_4, p_5) + S_2(p_2, p_3, p_4)\} \quad (4\text{-}23)$$

… = …

… = …

$$S_{N-3}(p_{N-3}, p_{N-2}, p_{N-1}) = \min_{p_{N-4}}\{\varepsilon_{N-4}(p_{N-4}, p_{N-3}, p_{N-2}, p_{N-1}) + S_{N-4}(p_{N-4}, p_{N-3}, p_{N-2})\} \quad (4\text{-}24)$$

$$= min\{\varepsilon_0(p_0, p_1, p_2, p_3) + \varepsilon_1(p_1, p_2, p_3, p_4) + \varepsilon_2(p_2, p_3, p_4, p_5) + \ldots + \varepsilon_{N-4}(p_{N-4}, p_{N-3}, p_{N-2}, p_{N-1})\}$$

$$= \min\{\varepsilon_{snake}\} \quad (4\text{-}25)$$

As can be seen from the last equation which shows simply that recurrence relation minimizes the total energy of piecewise cubic spline.

Above recurrence relation can be verbalized as follows. Starting from the first span, positions of all of the four control points of the first span are changed in a 3x3 pixel window systematically and energy of the span is calculated for each combination of 4 control points. Among all the possible combinations of control points, the one that has the minimum energy level is picked. Then the same procedure is repeated for the next span (second span) whose control points are the last three control points of the previous span and the next control point. Again, positions of all of the 4 control points are changed in a window and the combination giving the minimum energy configuration is found. At this stage, energy of the current span and the energy of the previous span are summed and supplied to the next step which will calculate the total energy up to the current span. This process continues until the last span of the B-spline is reached and energy of the whole spline is obtained.

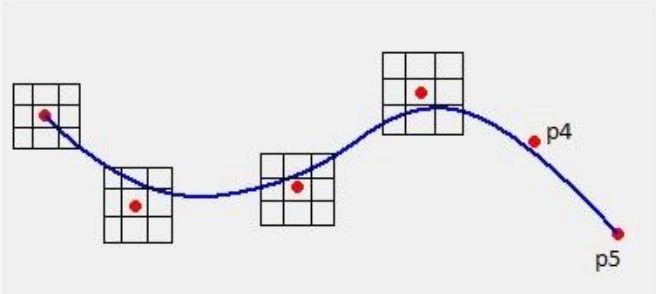

Figure 4.34: Control points of a span make a search in 3x3 pixel window.

Above mentioned process is applied repeatedly and iteratively until the overall spline reaches the possible minimum energy level. This iterative algorithm is explained in **[10]** as follows:

1-Initialize B-spline $v(s)$

2- Minimize $\varepsilon_{snake}[v^i(s)] \rightarrow \varepsilon_{snake}[v^{i+1}(s)]$

3-Update all control points accordingly ($p_j^i \rightarrow p_j^{i+1}$, for all j)

4-If i > MAX or $|\varepsilon_{snake}[v^i(s)] - \varepsilon_{snake}[v^{i+1}(s)]| < THRESHOLD$, then STOP

5- i=i+1

6-Go to step 2

Since algorithmic complexity of this algorithm proposed by **[10]** is $O(n^4N)$ and it takes much time for the optimization of the splines, this algorithm is clinically impractical. For clinical applicability and practicality, we have proposed a dynamic programming having an algorithmic complexity of $O(n^3 + N.n)$. Lower the complexity of an algorithm, faster the running time and hence enabling the algorithm clinically applicable.

The difference of our proposed algorithm ($O(n^3 + N.n)$) than the one proposed by **[10]** ($O(n^4.N)$) is the optimization of spans after the first one. In **[10]**, an optimum search is done by changing the location of all control points for every span and this makes a n^4 combination for all span. In our algorithm however, n^4 combination is

done only for the first span. Remembering that our first control point is fixed, only the last three control points of the first span make a search for best conformation. This reduces n^4 to n^3 combination for the first span. Following spans use the locations of the last three control points as same and only makes an optimum energy search for the last control point of the current span which makes n combination.

Another difference of our algorithm is the stopping criteria of the iterations. While other algorithm waits until absolute difference of energy levels of successive splines is smaller than a threshold, our algorithm waits until a local maximum energy level is reached.

In the light of above explanations, our proposed algorithm can be defined step by step as follows:

1-Initialize B-spline $v(s)$

2- Minimize $\varepsilon_{snake}\left[v^i(s)\right] \rightarrow \varepsilon_{snake}\left[v^{i+1}(s)\right]$

3-Update all control points accordingly ($p_j^i \rightarrow p_j^{i+1}$, for all j)

4-If $\varepsilon_{snake}\left[v^{i+1}(s)\right] - \varepsilon_{snake}\left[v^i(s)\right] < 0$, then STOP

5- i = i + 1

6-Go to step 2

4.4.3. Fast Semi-Automatic Spline Fitting

This method is alternative to the method in which splines are manually initialized and then optimized by dynamic programming. Although dynamic programming having a lower algorithmic complexity is developed, it is still time consuming due to its iterative nature.

In semi-automatic spline fitting method, user does not have to initialize splines by putting control points one by one. Instead, a few control points put before and after the stenotic region and traversing inside of the vessel are enough. The method can be summarized as follows: Firstly two control points are put into the inner region of the vessel, and then linearly spaced control points are generated between two control

points. Afterwards, each of these control points searches for the maximum energy point (i.e. edge point) in a direction perpendicular to the line formed by linearly-spaced control points as shown in below Figure 4.35. This search is bidirectional and both right and left spline control points are found. After control points are detected, right and left splines are easily formed by using these control points.

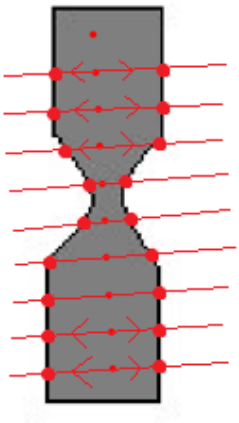

Figure 4.35: Bidirectional search from middle linearly-spaced control points.

As can be seen from Figures 4.36, 4.37, 4.38, splines fit better to vessel boundaries as the number of control points put in between two control points are increased. However, in most of the cases coronary arteries are not that straight, actually they are curvy. In curvy structures, putting 2 control points just before and after the lesion is not enough. The line between control points must be inside of the vessel. Therefore, more than two control points must be determined for curvy coronary structures as shown in Figure 4.39.

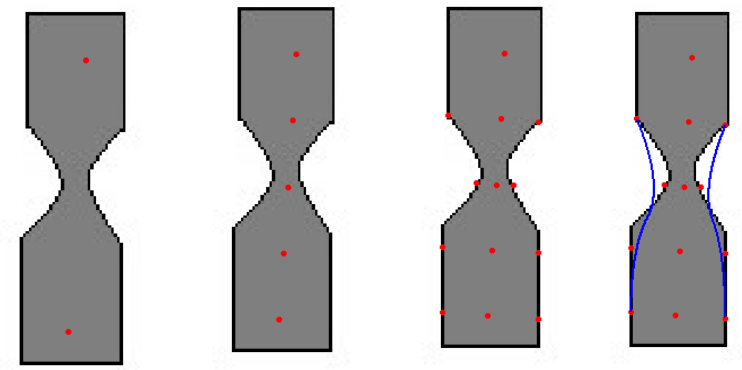

a b c d

Figure 4.36: Spline fitting using 4 control points (a) 2 control points are selected, (b) linearly-spaced control points are generated, (c) Right and left spline control points are found using bidirectional search, (d) Formed spline using control points.

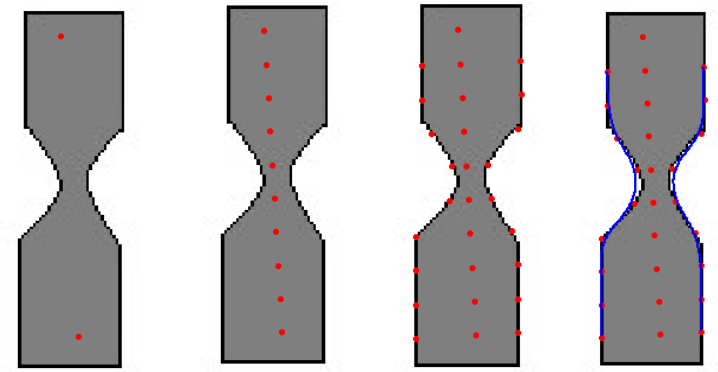

a b c d

Figure 4.37: Spline fitting using 9 control points (a) 2 control points are selected, (b) linearly-spaced control points are generated, (c) Right and left spline control points are found using bidirectional search, (d) Formed spline using control points.

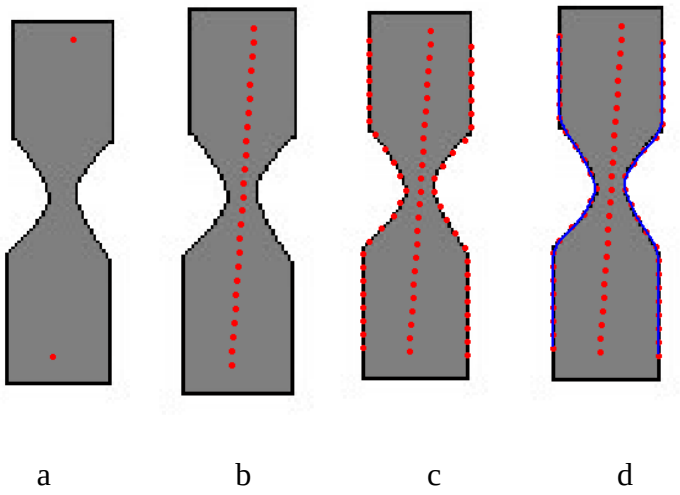

Figure 4.38: Spline fitting using 25 control points (a) 2 control points are selected, (b) linearly-spaced control points are generated, (c) Right and left spline control points are found using bidirectional search, (d) Formed spline using control points.

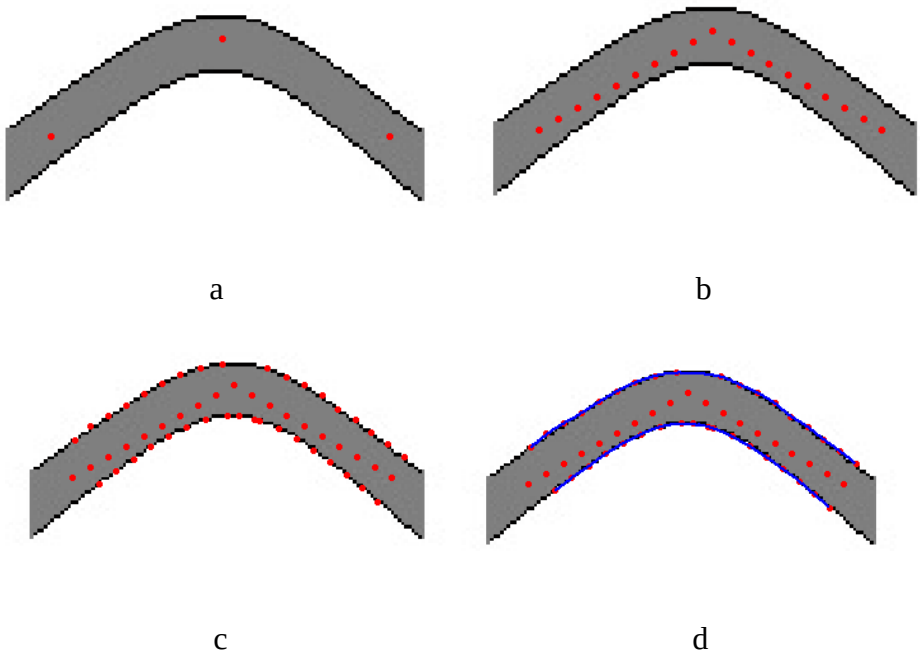

Figure 4.39: Spline fitting using curved vessel structure (a) 3 control points are selected, (b) linearly-spaced control points are generated, (c) Upper and lower spline control points are found using bidirectional search, (d) Formed spline using control points.

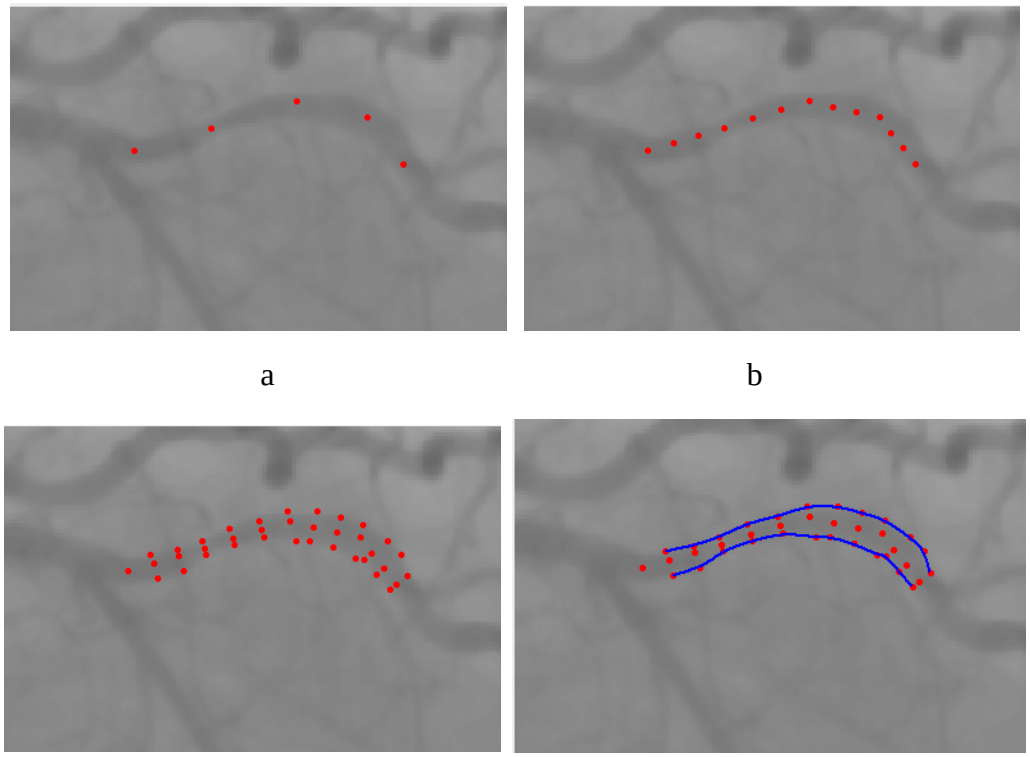

a b

c d

Figure 4.40: Spline fitting on real coronary artery (a) 5 control points are selected, (b) linearly-spaced control points are generated, (c) Upper and lower spline control points are found using bidirectional search, (d) Formed spline using control points.

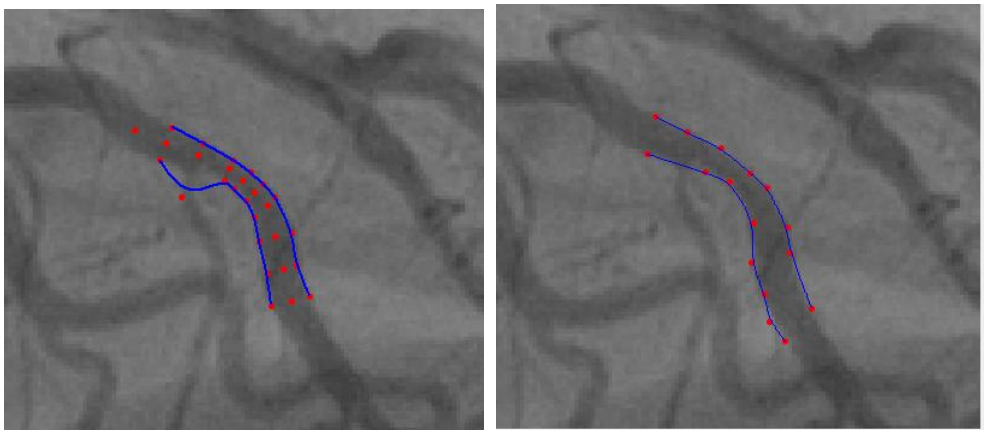

a b

Figure 4.41: (a) Semi-automatic spline initialization and fitting, (b) Manual spline initialization and optimization using DP.

One disadvantage of this approach is that it fails if there exists a nearby branching or background vessels. Nearby vessel borders create local energy spots that spoil the localization of control point as seen in Figure 4.41 (a). Therefore, vessel borders are not extracted properly. However, in the same condition manual spline initialization and optimizing splines via dynamic programming succeeds as shown in Figure 4.41 (b).

4.5. Detection and Quantification of Stenosis

4.5.1. Detection of Stenosis

In order to quantify the stenosis using 2D projection of a 3D vessel lumen, we need some quantitative parameters indicating the 2D anatomy of the vessel. As they will be detailed in the next chapter, these parameters are mean diameter and minimum diameter. While mean diameter is calculated in the non-stenotic part of the vessel, minimum diameter is measured in the stenotic part. Therefore, we need to separate non-stenotic region from the stenotic one. Detection of a stenosis includes the start and end point of stenosis.

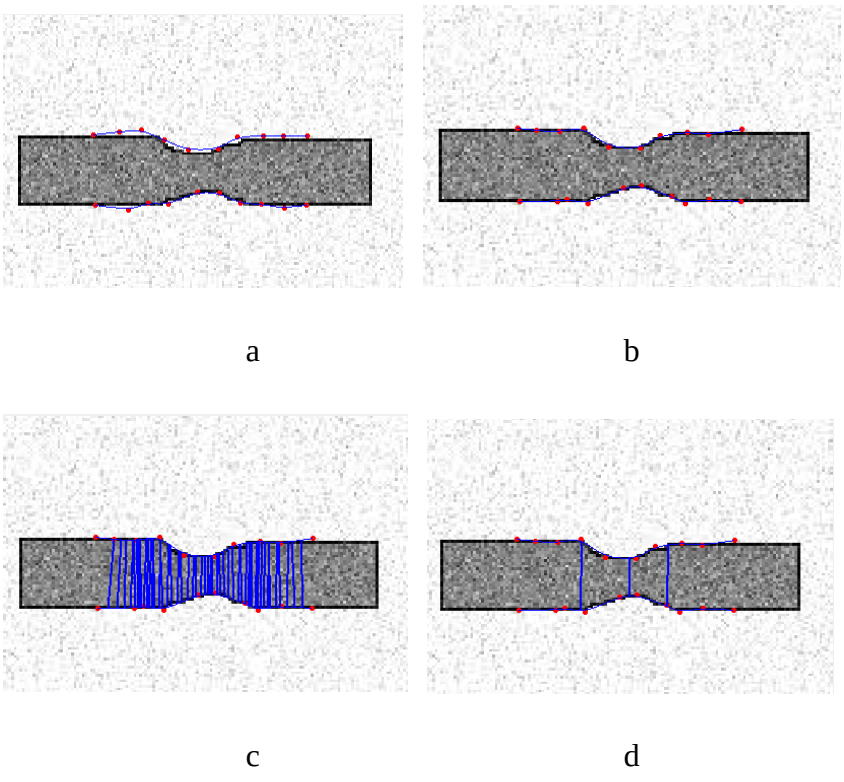

Figure 4.42: Detection of stenosis, step by step. (a)initial form of the spline, (b) optimized splines, (c) All traces are shown, (d) stenotic region is detected (Minimum diameter in stenotic region, start/end point of non-stenotic region).

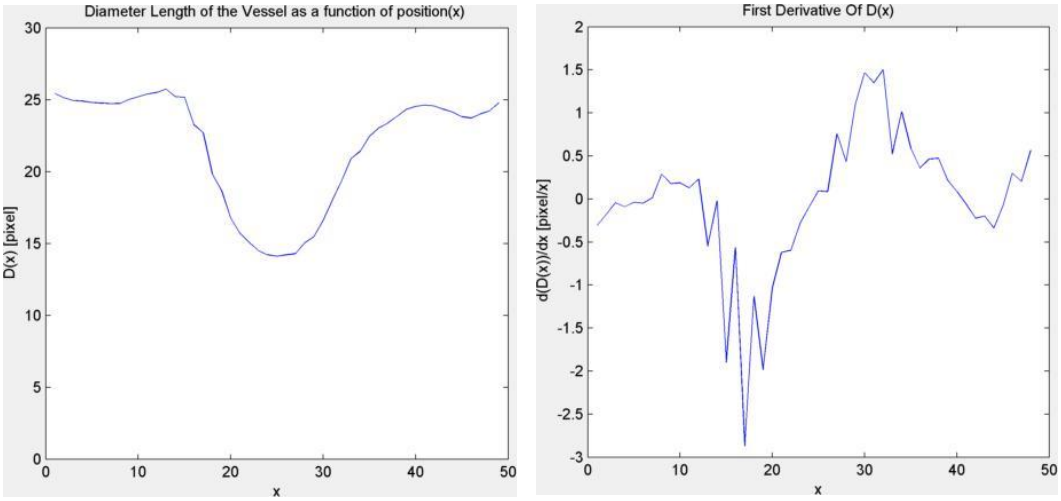

a b

Figure 4.43: Trace profile. (a) Vessel diameter as a function of position, (b) First derivative of (a)

Detection of a stenosis is achieved by using trace profile graph. The first steepest slope (i.e. first derivative) is a sign for the start point of the stenosis. The second steepest slope is a sign for end point of the stenosis. In this way, stenotic region is detected.

4.5.2. Quantification of Stenosis

After two splines are optimized and deformed so that they take the whole shape of the vessel, stenosis of the artery must be detected quantitatively. Quantification of severity of stenosis in this section will be based on geometrical features of the vessel like mean diameter, minimum diameter, mean cross section and minimum cross section of the artery. Using these geometrical features of the vessel, stenosis is quantified as a percentage.

In the reference **[13]**, stenosis severity quantification formulas are given as follows:

$$L_s = \%\ Length\ Stenosis = \left(1 - \frac{L_r}{L_m}\right) x100 \qquad (4\text{-}34)$$

$$A_s = \%\ Area\ Stenosis = \left(1 - \frac{A_r}{A_m}\right) x100 \qquad (4\text{-}35)$$

Where L_r is the minimal diameter in stenotic region, L_m is the mean diameter in non-stenotic region, A_r is the minimum cross sectional area in stenotic region, A_m is the mean cross sectional area of the non-stenotic region. A_r and A_m values are computed under the assumption that vessels have circular cross sections. % Length Stenosis is also called as % Diameter Stenosis (% DS) in some sources and % DS convention will be used throughout this thesis. Percent area stenosis formula can be further detailed and simplified as follows:

$$A_s = \%\, Area\ Stenosis = \left(1 - \frac{\pi(L_r/2)^2}{\pi(L_m/2)^2}\right) x100$$

$$= \left(1 - \frac{{L_r}^2}{{L_m}^2}\right) x100 \qquad (4\text{-}36)$$

Main disadvantage about the above stenosis measurements are that they extremely depend on the viewpoint of the imaging. In other words, percent length or area stenosis of an artery may differ from one viewing angle to another.

To be able to assess the severity of the steonsis anatomically (i.e. geometrically), we need to determine both L_r and L_m values. In [11] these two values are calculated using "String Matching" technique. However, we will use analytical geometry approach to determine these two values.

4.5.2.1. Analytical Geometry Approach

Choose the smallest of the spline by comparing their lengths

1- Select points on the smaller spline and calculate the slope of the tangent line using nearest right and left neighbors
2- Calculate the slope of the line which is perpendicular to the tangent
3- One point and a slope in our hands, draw a perpendicular line which intersects the opposite spline
4- Detect the intersection point and draw a trace between these two points
5- Repeat steps 1-4 for the other points which are equally spaced on the smaller spline

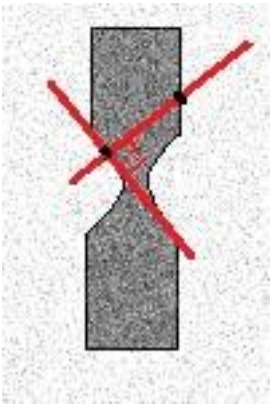

Figure 4.44: Illustration of tangent line of a point on the vessel edge and line perpendicular to it.

While this algorithm works for vessel walls which are parallel to each other (i.e. non-stenotic region), it does not work for vessel walls which are not parallel to each other(i.e. stenotic region) as shown in the Figure 4.46.

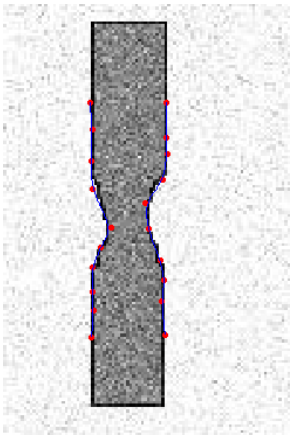

Figure 4.45: Optimized spline with dynamic programming complexity of O(n^3 + N.n)

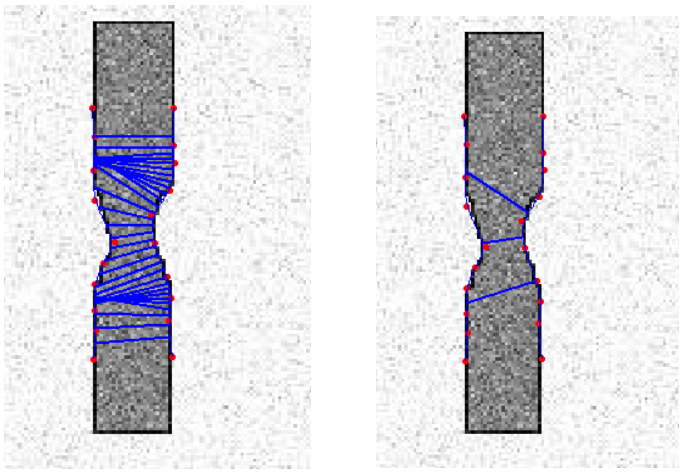

a b

Figure 4.46: (a) Traces obtained using Analytical Geometry Approach, (b) Resulting stenosis detection

4.5.2.2. Minimum Distance Search Algorithm

To overcome this problem, we did not use the point found in the opposite spline directly, instead we make a minimum distance search in a window. After minimum distance search, point on the opposite spline which gives the minimum diameter is selected as the point and a trace is drawn correspondingly.

Modified algorithm is as follows:

1- Select points on the smaller spline and calculate the slope of the tangent line using nearest right and left neighbours
2- Calculate the slope of the line which is perpendicular to the tangent
3- One point and a slope in our hands, draw a perpendicular line which intersects the opposite spline
4- Detect the intersection point
5- Make a minimum distance search in a neighborhood of the intersection point
6- Draw a trace between these two points
7- Repeat steps 1-6 for the other points which are equally spaced on the smaller spline

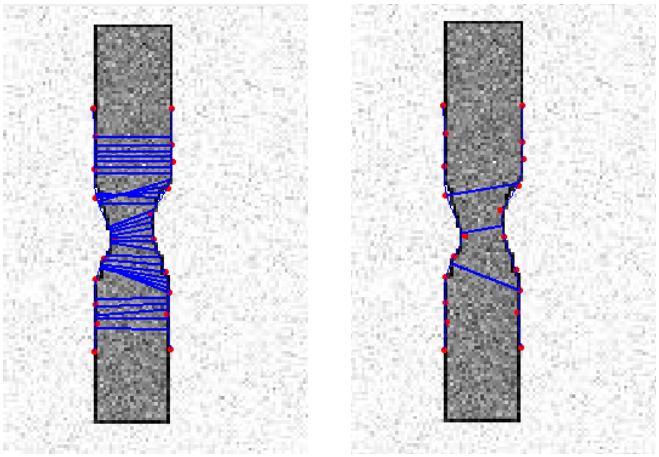

a b

Figure 4.47: (a) Traces obtained using Minimum Distance Search Algorithm, (b) Resulting stenosis detection

As seen in Figure 4.47, this algorithm still needs to be further enhanced.

4.5.2.3. Similar Slope Algorithm

Since minimum distance algorithm is not good, we have tried another algorithm which finds the traces between two splines by looking at the average slope of last 3 traces. For this algorithm, the first 3 traces must be drawn using analytical geometry approach. As can be deduced, if the slope of first 3 traces are not true, the rest of the traces will be all calculated wrong. This is the main drawback of this algorithm.

1- Select points on the smaller spline and calculate the slope of the tangent line using nearest right and left neighbours
2- Calculate the slope of the line which is perpendicular to the tangent
3- One point and a slope in our hands, draw a perpendicular line which intersects the opposite spline
4- Detect the intersection point
5- Make a similar slope search(by looking at the average slope of last 3 traces) in a neighborhood of the intersection point
6- Draw a trace between these two points
7- Repeat steps 1-6 for the other points which are equally spaced on the smaller spline

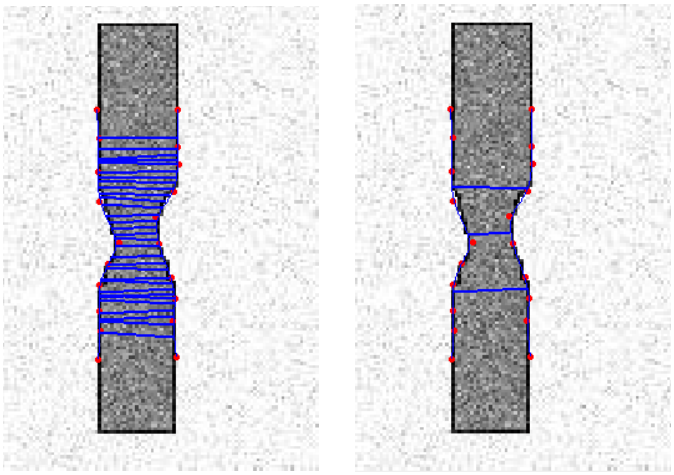

a b

Figure 4.48: (a) Traces obtained using Similar Slope Algorithm, (b) Resulting stenosis detection

4.5.2.4. Hybrid Algorithm

Since both "**Minimum Distance Search Algorithm**" and "**Similar Slope Algorithm**" algorithms do not give perfect results if they used only, we have propose here a hybrid algorithm which combines best of both algorithms. The proposed algorithm is as follows:

1- Firstly, apply "**Minimum Distance Search Algorithm**"
2- Calculate the slope of all traces found in the step (1)
3- Subtract the slope of current trace from the previous one
4- If the resultant slope difference between two successive traces are greater than an adaptive threshold, apply "**Similar Slope Algorithm**"
5- Repeat steps 3-4 for all traces

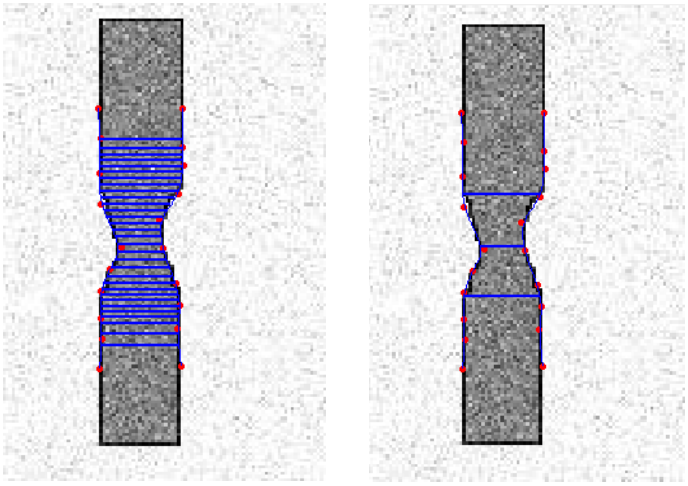

a b

Figure 4.49: (a) Traces obtained using Hybrid Algorithm, (b) Resulting stenosis detection

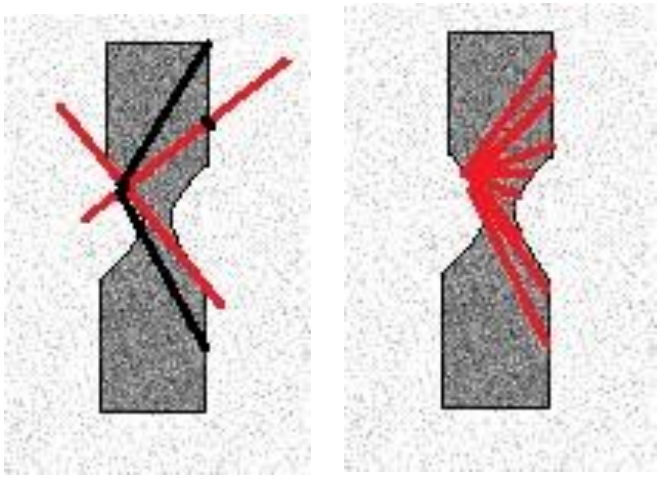

a b

Figure 4.50: (a) Boundary lines of trace search window (black lines) (b) Illustration of trace search window

4.6. Implementation Details

4.6.1. Selection of Design Parameters

4.6.1.1. Tuning Gabor Filter

Remembering the 2D Gabor filter formula (4-11) from the previous sections:

$$G_{\sigma_x,\sigma_y,f,\theta}(x,y) = e^{-\frac{x'^2}{2\sigma_x{}^2}-\frac{y'^2}{2\sigma_y^2}}.\cos(2\pi fx') + j.e^{-\frac{x'^2}{2\sigma_x{}^2}-\frac{y'^2}{2\sigma_y^2}}.\sin(2\pi fx')$$

where,

$$x' = x.cos(\theta) + y.sin(\theta) \qquad y' = -x.sin(\theta) + y.cos(\theta)$$

As can be inferred from the formula, Gabor filter response is a function of σ_x, σ_y, f, θ and size of the filter. Determination of these parameters must be carefully done, since change in these parameters may completely result in different responses.

σ_x, σ_y (standard deviations) are the widths of the Gaussian envelopes in –x and –y direction determining the frequency and orientation enhancement of features respectively **[10]**. While σ_x determines how much sharp edges are enhanced, σ_y determines the amount of smoothing along the direction of the Gabor filter. While selection of high σ_x values lead to artifacts, selection of low σ_x values result in low-pass filtering effect. Similary, high values of σ_y blurs the image as well **[2]**. In **[10]**, σ_x is chosen as 1 stating that $\sigma_x > 2$ enhances the center of the line rather than its edges. Their analysis is based on the dimension of the vessel. They state that dimension of the coronary arteries are between 0.5-5 mm. Images they used have a resolution of 5 pixels/mm, resulting an average dimension of 2,5 – 25 pixels. They tuned σ_x as 1 for their filter to be able to enhance the smallest artery which is 2,5 pixels. Although selection of these two values depend on the application and the image properties, for our study we have chosen $\sigma_y = \sigma_x = 1$.

f is the spatial frequency of the sinusoidal part and $\frac{1}{f}$ is defined as the period (T). In **[2]**, period of the sinusoid is selected as the width of fingerprint lines as shown in Figure 4.51. As mentioned in the previous paragraph, minimum width of a coronary artery is 2,5 pixel. As a result, we obtain period of the sinusoid as $T = 2{,}5$ and

frequency as $f = \frac{1}{T} = 0{,}4$. Another criteria for the selection of frequency is given as $\sigma_x \, . f = 0{,}39$ in **[10]**. Since we have chosen $\sigma_x = 1$ previously, f is chosen as 0,39.

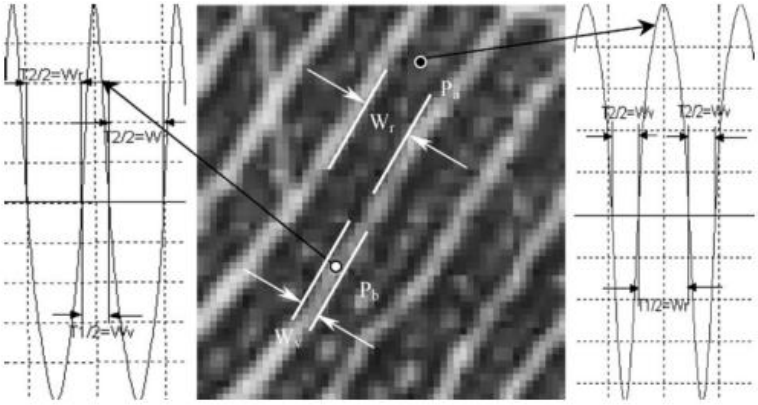

Figure 4.51: Frequency of the sinusoid is determined using the width of the fingerprint lines [2]

θ is the orientation of the filter that enhances the features of an image along that direction. Since we need the edge features of any direction, we need equally spaced Gabor filters spanning over 180 degrees. If three Gabor filters are to be used, their orientations are 60^o, 120^σ, 180^o; similarly if six Gabor filters are to be used, orientations of the filters are 30^o, 60^σ, 90^o, 120^o, 150^o and 180^o respectively. We have chosen to use six Gabor filters having orientations of 30^o, 60^σ, 90^o, 120^o, 150^o, 180^o. Convolution mask size of our Gabor filter is 9x9.

Gabor filter design parameters are shown in Table 4.2:

Table 4.2: Gabor filter design parameters

σ_x	1
σ_y	1
f	0.39
θ	30^o, 60^σ, 90^o, 120^o, 150^o, 180^o (6 filters)
Filter Size	9x9

4.6.1.2. Perona-Malik Anisotropic Diffusion Filter

Remembering the final form of the Anisotropic Diffusion filter from the previous sections:

$$u_{i,j}^{n+1} = u_{i,j}^{n} + \left(\frac{\Delta t}{h^2}\right) g(|\nabla u_\sigma|).(u_{i,j-1}^{n} + u_{i,j+1}^{n} + u_{i+1,j}^{n} + u_{i-1,j}^{n} - 4u_{i,j}^{n})$$

Knowing that $u_{i,j}^{n}$ is the intensity of pixel i,j of the image u at the n^{th} iteration, the only parameters affecting the response of the filter are constant $\left(\frac{\Delta t}{h^2}\right)$, total number of iteration n, and $g(.)$ function.

For numerical stability of the solution, the constant term $\left(\frac{\Delta t}{h^2}\right)$ must be in the range [0, 0.25] as stated in [38]. Δt is the time steps that diffusion occurs. Since quick diffusion is desired, which means bigger time steps in discrete domain, constant term including time steps must be chosen as high as possible. Therefore, we have chosen constant term as $\left(\frac{\Delta t}{h^2}\right) = 0{,}25$ for faster diffusion and better time performance.

Iteration number derives from the discretization of the diffusion problem. It corresponds to time in continuous domain. As time passes (iteration number increases), more diffusion occurs in the image. If diffusion is allowed to last sufficiently long time, details in the image starts to disappear and finally all edges will be blurred and a uniform image is obtained theoretically. If diffusion occurs less, edges are still preserved but smoothing effect will be observed less. This is the tradeoff between edge preservation and smoothing. For our design, we have chosen iteration number $n = 20$.

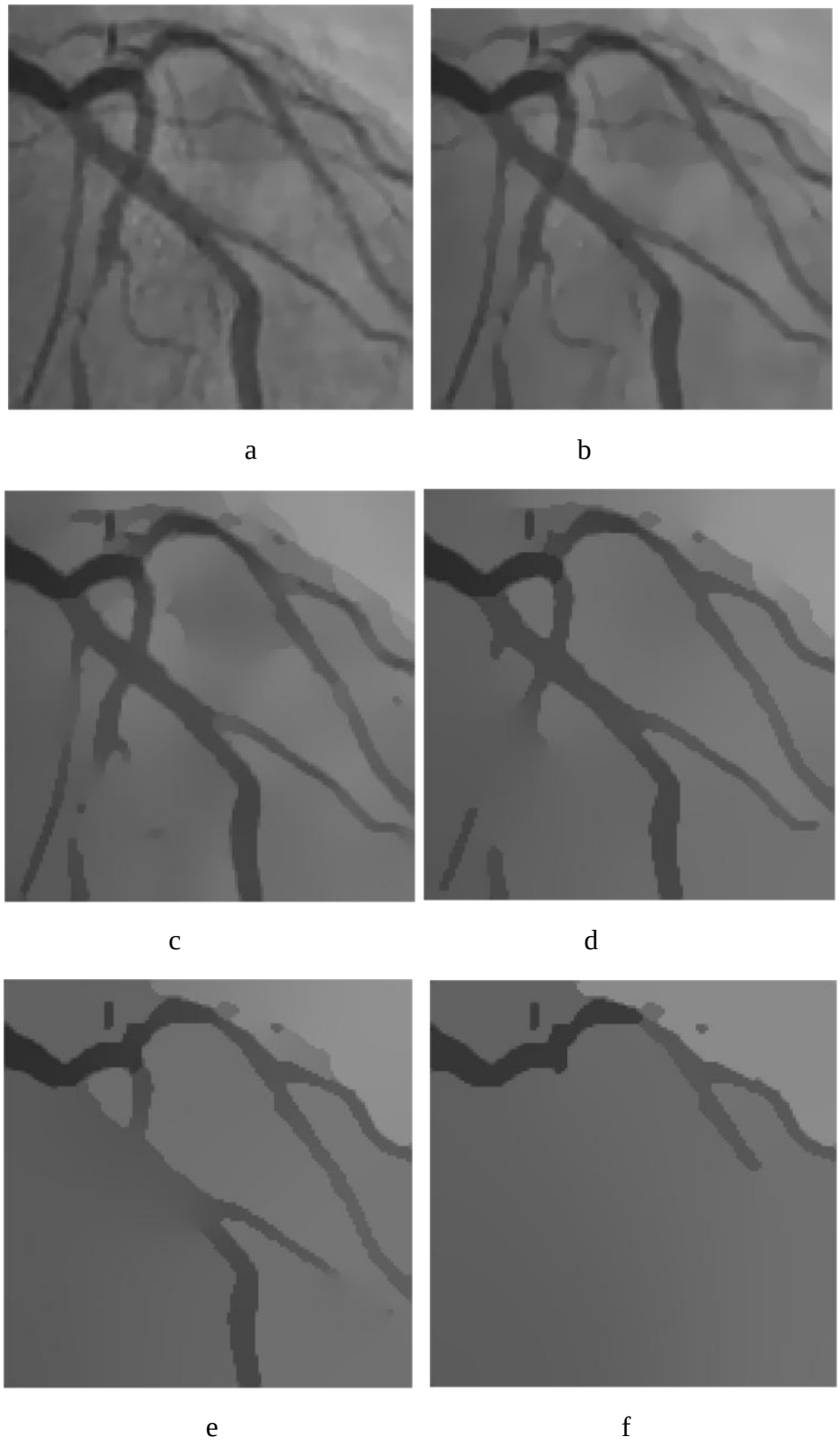

Figure 4.52: Anisotropic diffused images at different iteration numbers, (a) 5 iteration, (b) 20 iteration (c) 100 iteration, (d) 500 iteration (e) 2000 iteration, (f) 10000 iteration

Another design parameter affecting the diffused image is the g(.) function whose only variable is λ. There are two types of g(.) function which are Perona-Malik and Charbonnier types. Both of them are decreasing functions of image gradient having slightly different characteristics with respect to image gradient values. Although Charbonnier function allows diffusion at high gradient regions, Perona-Malik function does not allow much diffusion at high gradient regions. As a result, Perona-Malik type diffusion function preserves more edge features than Charbonnier one. Therefore we have chosen Perona-Malik type diffusion in our design to preserve edge features more. As λ increases, diffusion occurs even high gradient regions (i.e. edges) and filter starts behaving as if a Gaussian smoothing filter which is undesired for our case. Since we want to preserve edge features, we have chosen λ as small as possible so that no diffusion occurs for high gradient regions. Resultantly, we have chosen $\lambda = 0.1$.

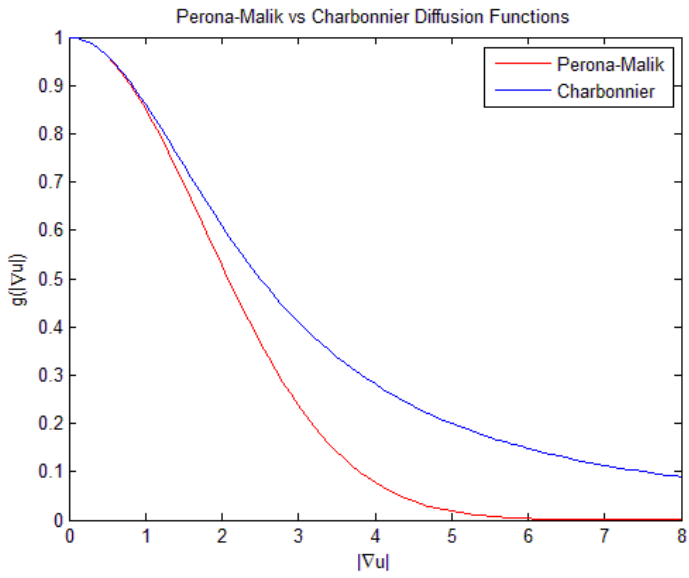

Figure 4.53: Perona-Malik and Charbonnier type diffusion functions for λ=2.5

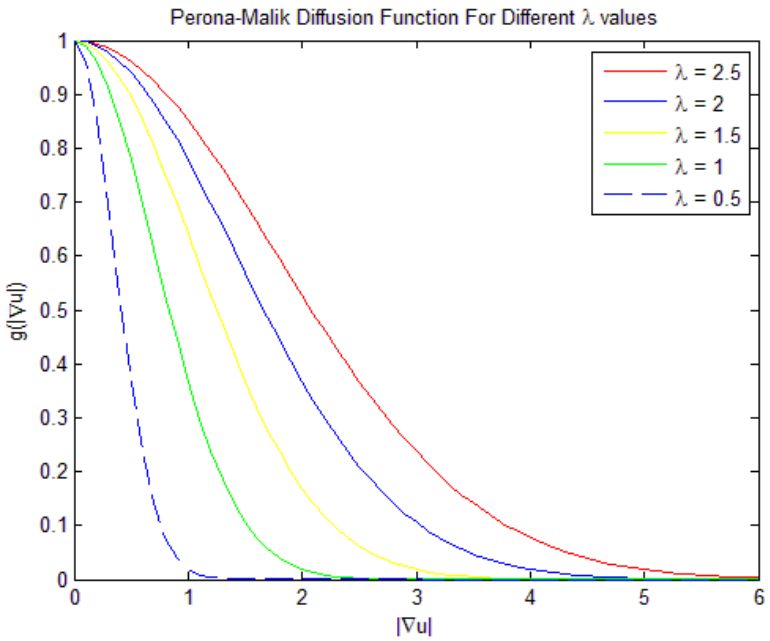

Figure 4.54: Perona-Malik Diffusion function for different λ values.

Table 4.3: Anisotropic Diffusion design parameters

$\left(\frac{\Delta t}{h^2}\right)$	0.25
# of Iteration	20
Type of Diffusion Function	Perona-Malik
λ	0.1

CHAPTER 5

EXPERIMENTS AND RESULTS

5.1. Performance Evaluation Metrics

To determine the reliability of the proposed contour extraction algorithm, we need to define some quantitative metrics that show the performance of the algorithm. Since extracted contour represents the edges of the vessel, we may approach this problem as an "edge detection" problem and use the commonly used metrics which are used in edge detection algorithm performance analysis.

While evaluating the performance of the proposed algorithm, a spline drawn by an interventional cardiologist will be used as the ground truth contour representing the edge of a vessel.

Following parameters are used when determining whether an edge pixel is correctly detected or not:

True Positive (TP): Number of correctly detected edge pixels

False Positive (FP): Number of pixels which are detected as edge pixels, but in fact they are not edge pixels

False Negative (FN): Number of pixels which are not detected as edge pixels, but in fact they are edge pixels.

Using these parameters, some indices are proposed by **[55]** which are percentage of correctly detected edge pixels (P_{co}), percentage of pixels which are not detected (P_{nd}), percentage of false alarm (P_{fa}) which is calculated by using erroneously detected edge pixels.

$$P_{co} = \frac{TP}{\max(N_I, N_{GT})} \tag{5-1}$$

$$P_{nd} = \frac{FN}{\max(N_I, N_{GT})} \quad (5\text{-}2)$$

$$P_{fa} = \frac{FP}{\max(N_I, N_{GT})} \quad (5\text{-}3)$$

where N_I is the number of points in the extracted contour and N_{GT} is the number of points in the ground truth contour. Valid ranges of P_{co}, P_{nd} and P_{fa} are all same and between zero and one [0, 1]. Optimum values of an ideal edge detector for P_{co}, P_{nd}, $P_{fa}$are 1, 0, 0 respectively. While $P_{co} = 1$ means that all edge pixels are detected correctly; $P_{nd} = P_{fa} = 0$ means that there is no edge pixel which is not detected and there is no erroneously detected pixels (i.e. No false alarm).

Another useful metric that describes the similarity and difference between two contours by calculating the distance of all pairs of points belonging to two different contours. This metric is proposed by Pratt **[56]** and called as Index of Merit of Pratt (IMP).

$$IMP = \frac{1}{\max(N_I, N_{GT})} \sum_{i=1}^{N_{GT}} \frac{1}{1 + \alpha . d_i^2} \quad (5\text{-}4)$$

Where d_i is the distance between the ground truth edge pixel and the nearest pixel of the proposed contour and α is the calibration constant and set to $1/9$ empirically by Pratt [56]. IMP is the indicator of the similarity between two contours and ranges from 0 to 1 [0, 1]. While 1 represents a perfect fit between proposed contour and ground truth, values close to zero represent bad edge detection performance and bad contour similarity.

Having four metricsIMP, P_{co}, P_{nd}, P_{fa} and with their optimal values for an ideal edge detector (1, 1, 0, 0); a new metric ($d_{£2}^4$) is defined as the Euclidian distance (i.e. L2 norm) from the 4D metric space (IMP, P_{co}, P_{nd}, P_{fa}) defining the deviation from the optimum edge location and its formula is as follows:

$$d_{£2}^4 = \sqrt{(IMP - 1)^2 + (P_{co} - 1)^2 + P_{nd}^2 + P_{fa}^2} \quad (5\text{-}5)$$

$d_{£2}^{4}$ ranges between 0 and 2 [0, 2]. While 0 means optimum edge localization, values far from 0 and close to 2 means bad edge detection performance. All of the aforementioned 5 metrics, their range and optimum values are tabulated in Table 5.1.

Table 5.1: Contour extraction performance evaluation metrics, their ranges and optimum values.

Metric Name	Range	Optimum Value
P_{co}	[0, 1]	1
P_{nd}	[0, 1]	0
P_{fa}	[0, 1]	0
IMP	[0, 1]	1
$d_{£2}^{4}$	[0, 2]	0

Since we use B-spline snakes for the representation of edge of a vessel, optimized contour consists of floating numbers rather than integer values. However, pixel locations are expressed only in integer numbers. Therefore, before starting the performance evaluation, points on the contour which consists of floating point numbers must be rounded into integer pixel locations (e.g. (10.76, 7.23) → (11, 7)). Floating point numbers of the optimized spline in Figure 5.1 (c) are rounded to integer pixel locations and displayed in Figure 5.1 (d).

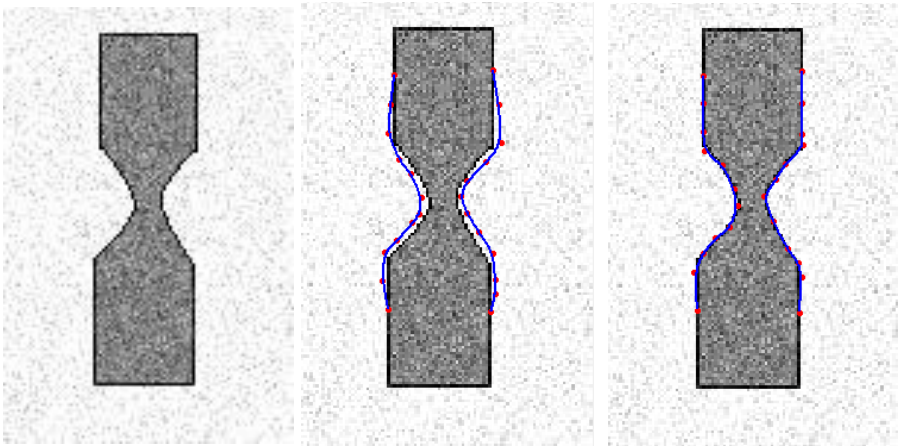

a b c

Figure 5.1: (a) Synthetic image added a Gaussian noise having standard deviation of 0.02, (b) Initial spline, (c) Spline after optimization (O(n3 + N.n))

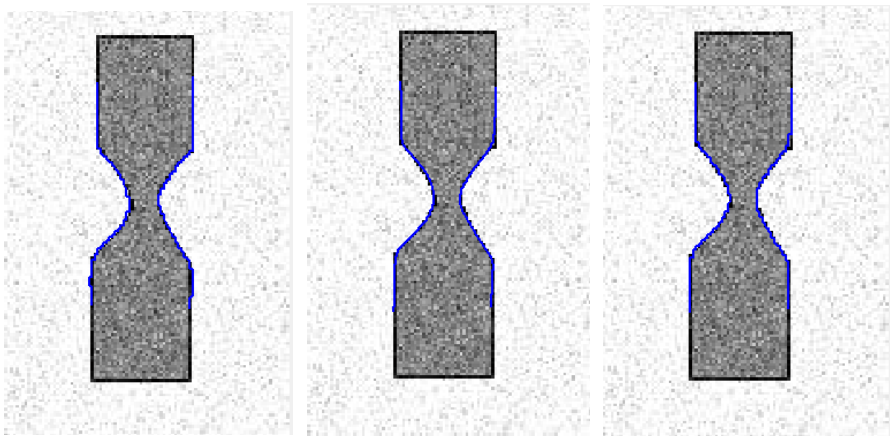

d e f

Figure 5.1 (continued): (d) Optimized spline converted to pixels, (e) Ground truth spline, (f) Ground truth spline converted to pixels

With the ground truth given in Figure 5.1 (f), performance evaluation parameters and metrics are calculated as in Table 5.2. Results shown in Table 5.2 are an example of performance evaluation for the optimized spline in Figure 5.1 (c).

Table 5.2: Metrics and parameters used in the metric calculation and their values for above experiment

N_I	103
N_{GT}	104
TP	80
FP	23
FN	24
P_{co}	0.7692
P_{nd}	0.2308
P_{fa}	0.2212
IMP	0.9711
$d_{\pounds 2}^{4}$	0.3953

5.2. Repeatability and Robustness

To investigate the repeatability and robustness of the proposed algorithm, above experiment will be repeated 10 times each time with different initial splines and then corresponding performance metrics will be observed. Ground truth used in these experiments is the same as in Figure 5.1 (f). Figure 5.2 illustrates left and right splines that we call them in this way throughout the thesis.

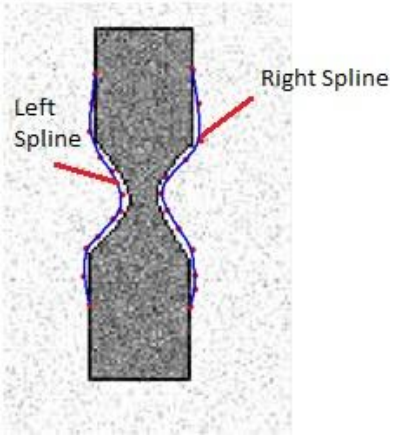

Figure 5.2: Left and Right spline.

10 successive experiments are performed for both left and right splines. Corresponding performance metrics are obtained as in Table 5.3 and Table 5.4 respectively. Then, Figure 5.3 and Figure 5.4 are plotted by using the data in these two tables.

Table 5.3: Results of 10 experiments of left spline

	EXP-1	EXP-2	EXP-3	EXP-4	EXP-5	EXP-6	EXP-7	EXP-8	EXP-9	EXP-10
N_{GT}	104	104	104	104	104	104	104	104	104	104
N_I	103	99	105	103	98	101	102	102	103	103
TP	80	71	75	82	71	75	62	69	59	56
FP	23	28	30	21	27	26	40	33	44	47
FN	24	33	29	22	33	29	42	35	45	48
P_{co}	0.7692	0.6827	0.7143	0.7885	0.6827	0.7212	0.5962	0.6635	0.5673	0.5385
P_{nd}	0.2308	0.3173	0.2762	0.2115	0.3173	0.2788	0.4038	0.3365	0.4327	0.4615
P_{fa}	0.2212	0.2692	0.2857	0.2019	0.2596	0.2500	0.3846	0.3173	0.4231	0.4519
IMP	0.9711	0.9683	0.9629	0.9745	0.9659	0.9662	0.9557	0.9663	0.9544	0.9426
d_{E2}^4	0.3953	0.5243	0.4908	0.3618	0.5195	0.4681	0.6900	0.5730	0.7453	0.7960

Table 5.4: Results of 10 experiments of right spline

	EXP-1	EXP-2	EXP-3	EXP-4	EXP-5	EXP-6	EXP-7	EXP-8	EXP-9	EXP-10
N_{GT}	98	98	98	98	98	98	98	98	98	98
N_I	95	99	99	97	100	95	95	98	96	97
TP	64	60	71	58	60	63	61	58	53	57
FP	31	39	28	39	40	32	34	40	43	40
FN	34	38	27	40	38	35	37	40	45	41
P_{co}	0.6531	0.6061	0.7172	0.5918	0.6000	0.6429	0.6224	0.5918	0.5408	0.5816
P_{nd}	0.3469	0.3838	0.2727	0.4082	0.3800	0.3571	0.3776	0.4082	0.4592	0.4184
P_{fa}	0.3163	0.3939	0.2828	0.3980	0.4000	0.3265	0.3469	0.4082	0.4388	0.4082
IMP	0.9607	0.9461	0.9618	0.9550	0.9404	0.9605	0.9576	0.9567	0.9524	0.9535
$d^4_{\pounds 2}$	0.5851	0.6787	0.4856	0.7026	0.6841	0.6027	0.6382	0.7083	0.7852	0.7203

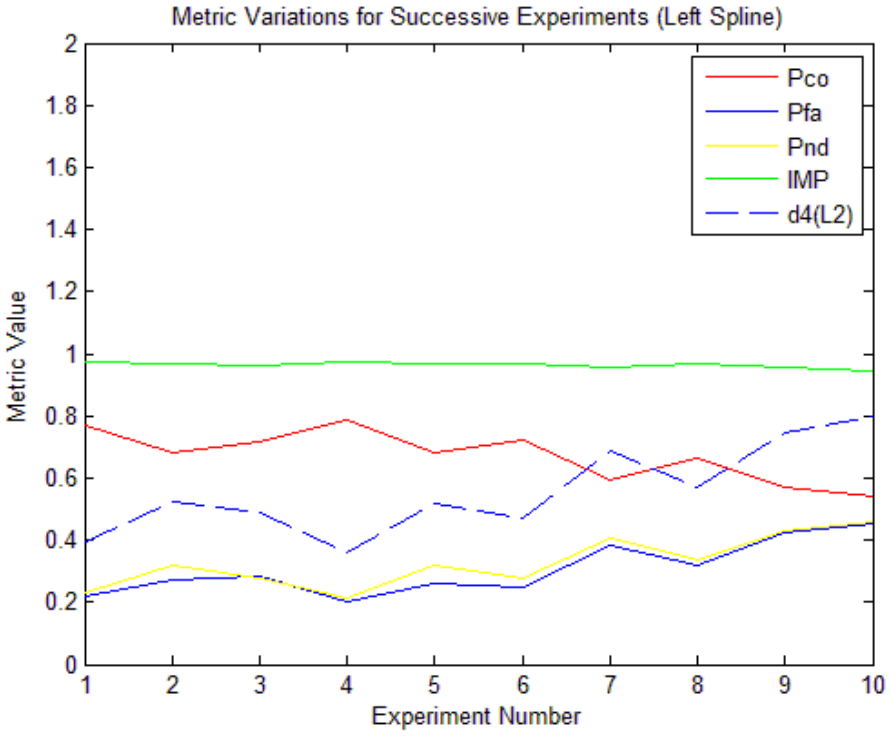

Figure 5.3: Metric variations for successive experiments of left spline (Illustration of Table 5.3)

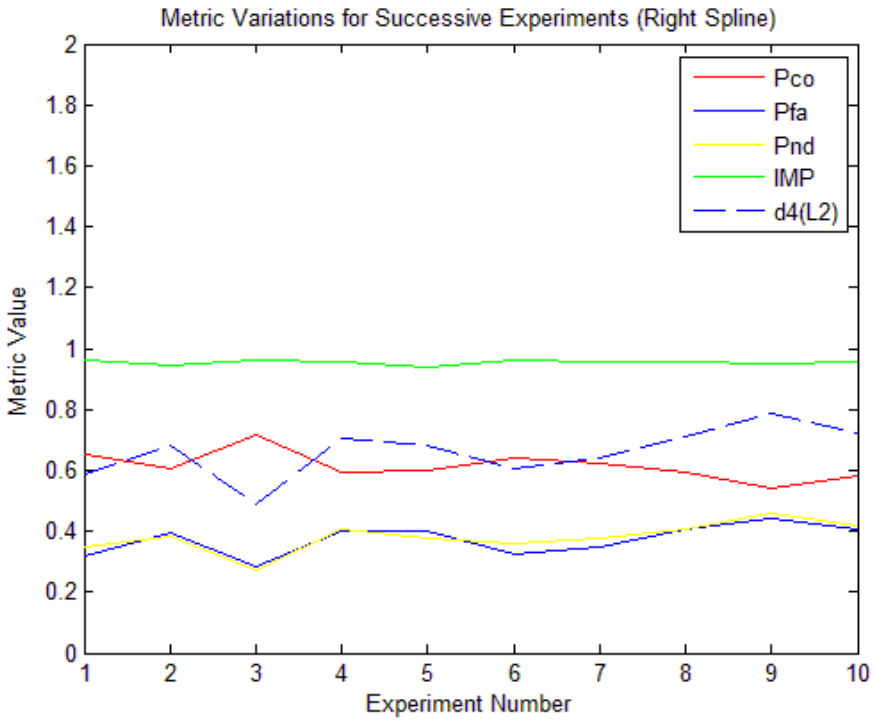

Figure 5.4: Metric variations for successive experiments of right spline (Illustration of Table 5.4)

P_{co}, P_{nd}, P_{fa} are the metrics showing the edge detection capability of an edge detector after making a pixel-to-pixel comparison. As can be seen in Figure 5.3 and Figure 5.4, these metrics are not same and varies in a reasonable range for each experiment of spline optimization scheme. In fact, this is not a desired result for an edge detector. However, our main concern is the extraction of the contour, representing the vessel boundaries, rather than the detection of edge pixels. Therefore, IMP (Index of Merit of Pratt) is more important for our point of view since it represents the similarity between two contours. Additionally, IMP is more stable and very close to its optimal value (unity) unlike P_{co}, P_{nd}, P_{fa}. Also $d_{£2}^4$ is not so robust during the experiments since this metric consists of IMP, P_{co}, P_{nd}, P_{fa} and fluctuations of P_{co}, P_{nd}, P_{fa} play important role on the fluctuation of $d_{£2}^4$. Cumulative effect of P_{co}, P_{nd}, P_{fa} are more dominant than the effect of IMP.

To show the importance of the metric IMP for our perception with respect to the metrics P_{co}, P_{nd}, P_{fa} consider the following example which represents not the worst case but a bad case. Consider a case in which every pixel of the optimized spline is 1

pixel near the pixels of the ground truth spline as in Figure 5.5. In this case, number of correctly detected edge pixels are zero ($P_{co} = 0$), all of the edge pixels are not detected ($P_{nd} = 1$) and all of the found pixels do not belong to the ground truth ($P_{fa} = 1$). In other words, none of the edge pixels are detected correctly; all of the found pixels are false alarm. Replacing all of these information into the equation of IMP (5-6) with $N_I = N_{GT} = 100$, $\alpha = 1/9$, $d_i = 1$, we get the following:

$$IMP = \frac{1}{\max(N_I, N_{GT})} \sum_{i=1}^{N_{GT}} \frac{1}{1 + \alpha . d_i^2} \tag{5-6}$$

$$IMP = \frac{1}{100} \sum_{i=1}^{100} \frac{1}{1+(1/9).1^2} = 0.9 \tag{5-7}$$

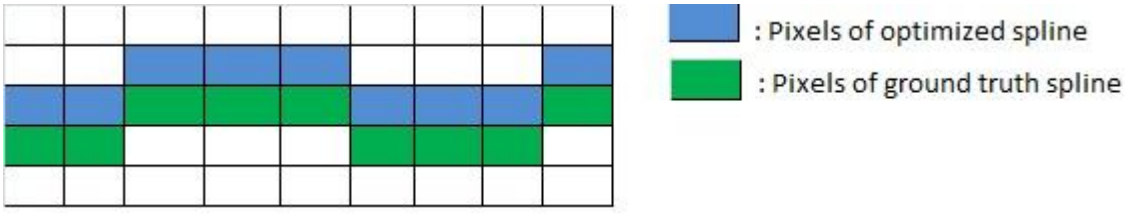

Figure 5.5: Illustration of the case in which every pixel of optimized spline is 1 pixel away from the ground truth pixels

Considering another bad case in which every pixel of the optimized spline is 2 pixel near the pixels of the ground truth spline as in Figure 5.6. In this case, again number of correctly detected edge pixels are zero ($P_{co} = 0$), all of the edge pixels are not detected ($P_{nd} = 1$) and all of the found pixels do not belong to the ground truth ($P_{fa} = 1$). Replacing all of these information into the equation of IMP with $N_I = N_{GT} = 100$, $\alpha = 1/9$, $d_i = 2$, we get the following:

$$IMP = \frac{1}{100} \sum_{i=1}^{100} \frac{1}{1 + (1/9).2^2} = 0.69$$

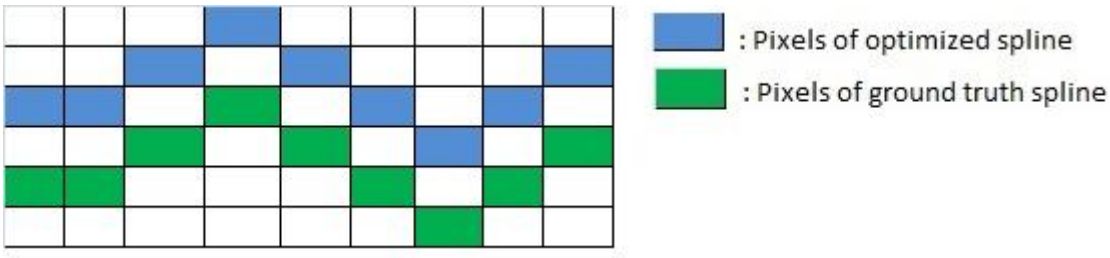

Figure 5.6: Illustration of the case in which every pixel of optimized spline is 2 pixel away from the ground truth pixels

Even in these bad cases, it is found that $IMP = 0.9$ and $IMP = 0.69$, respectively. This means that although none of the edge pixels are detected correctly, contour similarity metric (IMP) ranges from 90 % to 69 % for those 2 bad cases. These two examples explicitly show that IMP metric represents the performance of our contour optimization scheme better than the traditional edge detection metrics (P_{co}, P_{nd}, P_{fa}).

5.3. Robustness to User Interaction

To investigate the repeatability and robustness of the proposed optimization scheme, different shape of initial splines are tested. With these experiments, effect of the initial spline and hence the user effect is investigated.

In Figure 5.7 (a), splines are initialized from the inner part of the synthetic vessel, and they are optimized well enough for both DP algorithms as shown in Figure 5.7 (b) and Figure 5.7 (c). In Figure 5.8 (a), splines are initialized in a wavy form, and their optimized forms are visualized in Figure 5.8 (b) and Figure 5.8 (c). In this experiment, optimization performance of DP algorithm with high complexity is higher. In Figure 5.9 (a), splines are initialized again in a wavy form but near the edge of the vessel. In this experiment, DP with high complexity again performs better, but DP with low complexity performs well compared to previous experiment. In Figure 5.10 (a), splines are initialized sufficiently far from the vessel edges, and we observe that both DP algorithms fail to optimize B-splines.

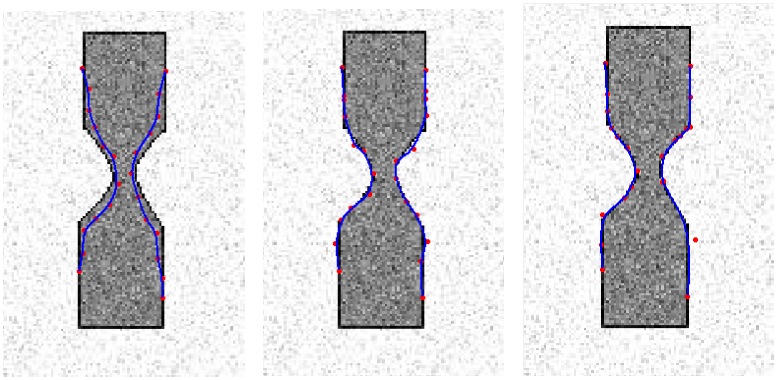

a b c

Figure 5.7: (a) Initial spline, (b) Optimized spline with DP complexity of O(n^3 + N.n); IMPleft =0.9080, IMPright =0.8124 (c) Optimized spline with DP complexity of O(n^4.N); IMPleft =0.9750, IMPright =0.8696

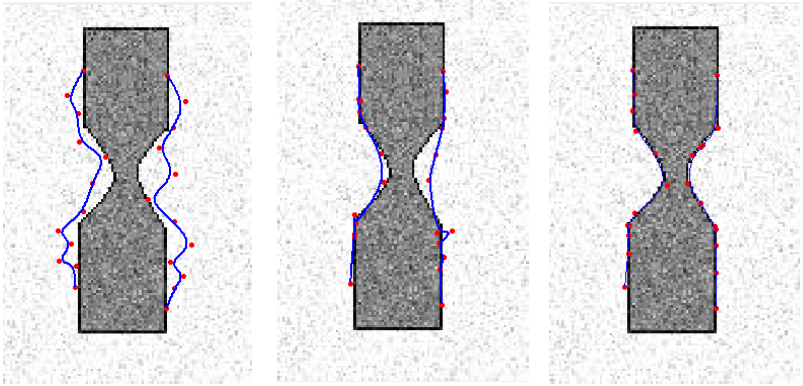

a b c

Figure 5.8: (a) Initial spline, (b) Optimized spline with DP complexity of O(n^3 + N.n); IMPleft =0.8876, IMPright =0.5962 (c) Optimized spline with DP complexity of O(n^4.N); IMPleft =0.9132, IMPright =0.8679

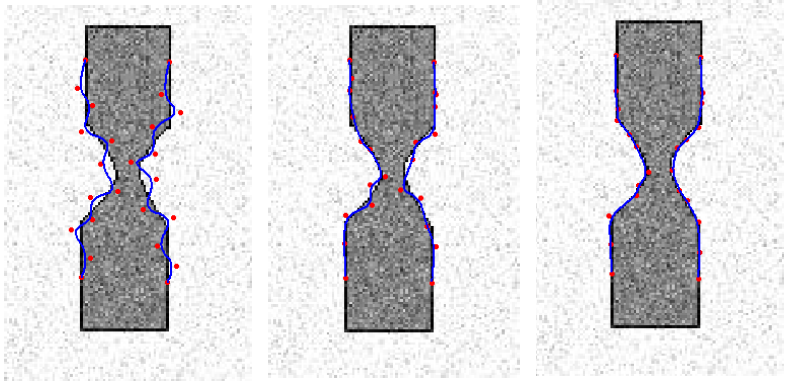

a b c

Figure 5.9: (a) Initial spline, (b) Optimized spline with DP complexity of O(n^3 + N.n); IMPleft =0.8877, IMPright =0.8412 (c) Optimized spline with DP complexity of O(n^4.N); IMPleft =0.9244, IMPright =0.8698

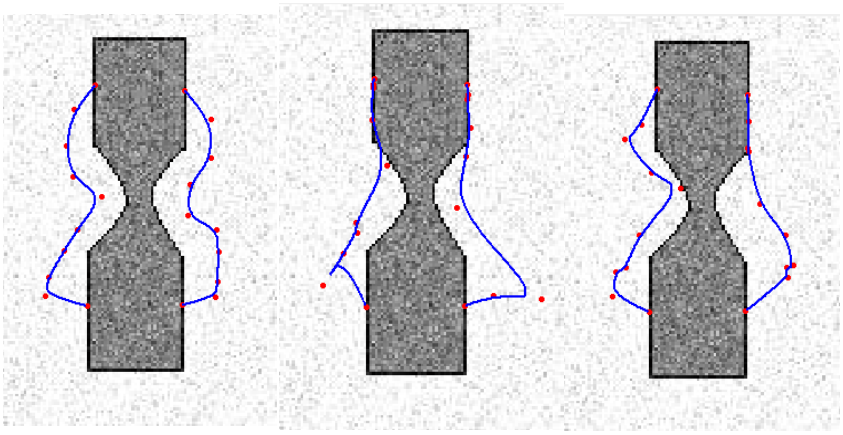

a b c

Figure 5.10: (a) Initial spline, (b) Optimized spline with DP complexity of O(n^3 + N.n); IMPleft =0.4488, IMPright =0.3189 (c) Optimized spline with DP complexity of O(n^4.N); IMPleft =0.2218, IMPright =0.3373

Experiments conducted in this part show that DP algorithm having a complexity of $O(n^4.N)$ is more robust to the initialization of different shape splines than the DP algorithm having a complexity of $O(n^3 + N.n)$. This conclusion is drawn by comparing the IMP metrics of the optimized spline and also by visual inspection. However, DP which is more robust to the initial condition is much slower than the less robust one as will be shown in the latter chapters. At this point, a trade-off appears between robustness to initial condition and optimization time. High complexity algorithm lasts hours and this makes this algorithm unfeasible for clinical applicability. Low complexity algorithm however, converges fast and optimizes the B-splines well enough if they are not initialized too far away from vessel edges. This algorithm is more suitable for clinical applicability due to its short run time, since splines are initialized by expert clinicians, who can start splines close to the vessel edges. Therefore, we have preferred to use low complexity DP algorithm for the optimization of B-splines.

If B-splines are initialized from very far away from the vessel edges, both algorithms fail to optimize the splines as seen in Figure 5.10. Since control points make a search within 3x3 pixels window for the best energy conformation, they are not able to reach far energy fields. As shown in Figure 5.11, initial control points are very far away from the energy field.

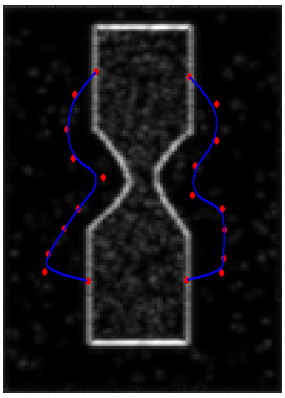

Figure 5.11: Initial spline is displayed on top of Gabor energy field.

5.4. Noise Immunity of Spline Optimization Scheme

In this part, noise immunity of the spline optimization scheme is tested for different types of noise; namely, Gaussian noise, Salt & Pepper noise, Speckle noise and Poisson noise. Speckle noised image is obtained by adding any multiplicative of a pixel intensity value to itself. The other noise types are very commonly used and known ones.

In this experiment, a synthetic image without any noise is used as shown in Figure 5.12 (a). Then, different noise types are added to the original image and noisy images are obtained as shown in Figure 5.13. Afterwards, initialized common spline shown in Figure 5.12 (b) is optimized and optimization results are displayed as in Figure 5.14. Optimization performance was also measured with IMP metric and corresponding results are shown in Table 5.5. This experiment is conducted with the same initial spline and the same ground truth data. In this way, noise immunity of spline optimization is tested with respect to a common initial spline.

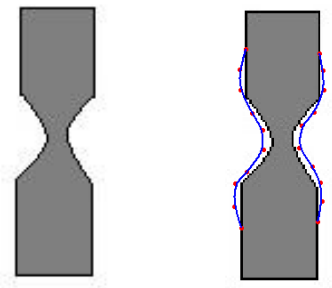

a b

Figure 5.12: (a) Original synthetic image without any noise, (b) Initialized Splines commonly

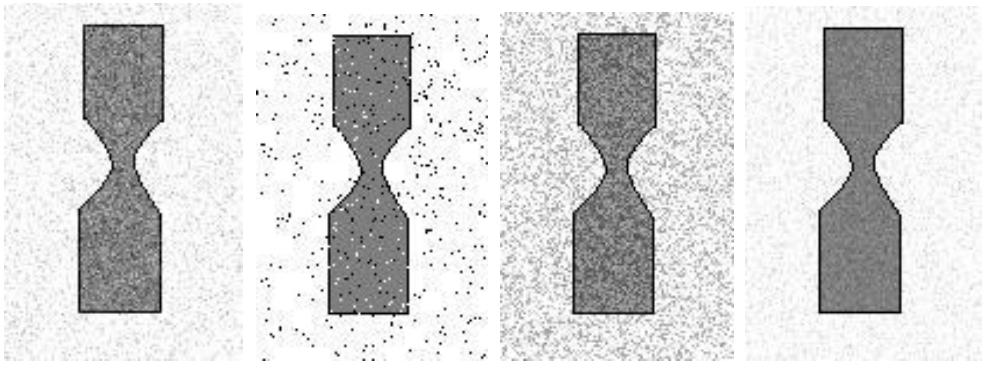

a b c d

Figure 5.13: (a) Gaussian-noised image, (b) Salt & Pepper-noised image, (c) Speckle-noised image, (d) Poisson-noised image

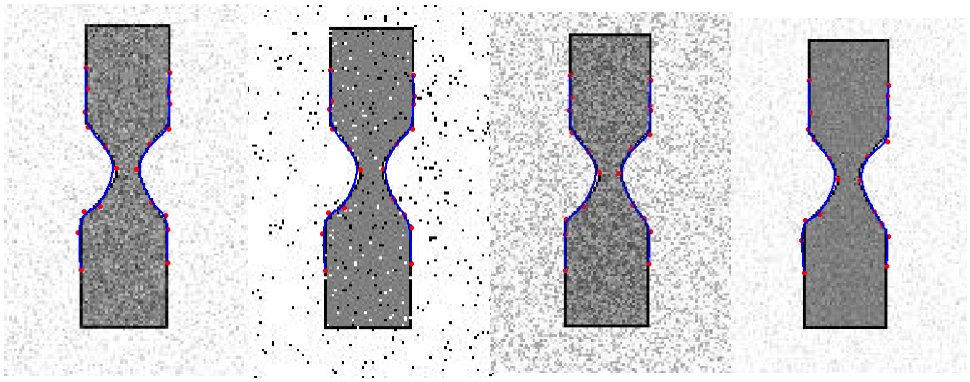

a b c d

Figure 5.14: Optimization of spline under the effect of different noise types: (a) Gaussian noise, (b) Salt & Pepper noise, (c) Speckle noise, (d) Poisson noise.

Table 5.5: IMP metrics of optimized spline under the effect of different noise types.

	Gaussian	Salt & Pepper	Speckle	Poisson
IMP_{left}	0.9588	0.9598	0.9675	0.9559
IMP_{right}	0.9695	0.9675	0.9547	0.9466

As can be seen in Table 5.5, our proposed spline optimization scheme is not much affected by different noise types. Although noise types differ, IMP metric (which represents the resemblance to ground truth spline) is almost the same and has a value around 0.95 meaning that 95 % resemblance to the ground truth data. This

performance is similar to the results obtained in the “Repeatability and Robustness” section.

Of all the noise types, Salt & Pepper noise is more likely to affect the performance of the spline optimization scheme. Especially, black dots near the vessel edges may negatively affect the optimized splines, since black dots appear as local energy spots when Gabor filter is applied. These local energy spots attract the spline to themselves rather than the edge of the vessel.

5.5. Performance Evaluation of Tracing Algorithms

Performance of hybrid tracing algorithm will be evaluated by measuring the number of correctly found traces and total number of traces. Here “correctly found trace” means that a particular trace represents the vessel diameter at that point. These measurements are obtained from both synthetic and real patient images.

Performance measurement on synthetic images is performed using Hybrid Tracing Algorithm, since it is the best one among the other tracing algorithms. To be able to measure the performance of Hybrid Tracing Algorithm on synthetic images, vertically oriented synthetic vessels are used so that expected slope of each trace would be zero. Start and end points of each trace correspond to a floating point number, slope of traces are not exactly equal to zero. If a slope of a trace is in a close vicinity of zero, it is marked as correctly found trace; if a slope is out of the close vicinity of zero, then it is marked as erroneously found trace. Therefore, we need to define a threshold to describe the close vicinity of zero. This threshold is chosen as 0,06.

If Slope of Trace < 0.06, TRUE (Correctly found trace)

If Slope of Trace > 0.06, FALSE (Erroneously found trace)

By using above criteria, three synthetic images, each having a different stenosis topology is tested as shown in Figure 5.15. Results of these measurements are tabulated in Table 5.6.

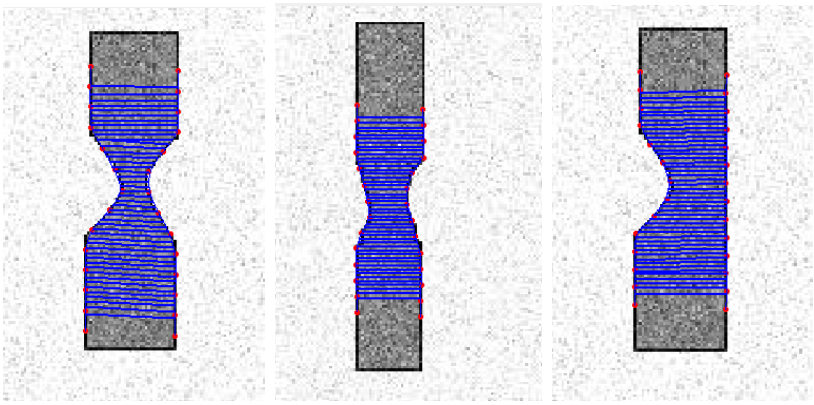

a b c

Figure 5.15: Traces obtained using three different synthetic images

Table 5.6: Performance measurement table of Figure 5.15**.**

	TRUE	FALSE	Percentage
Figure 5.15 (a)	47	0	100 %
Figure 5.15 (b)	47	0	100 %
Figure 5.15 (c)	47	0	100 %

Performance measurement of Hybrid Tracing Algorithm is performed only for a single orientation, since in section 5.6 we showed that proposed tracing algorithm is rotation-invariant. By looking at Table 5.6, one can conclude that performance of Hybrid Tracing Algorithm is 100 % when applied to synthetic images.

Although Hybrid Tracing Algorithm is the best one for synthetic images, all of the tracing algorithms are observed to be successful in different cases depending upon the anatomy and shape complexity of the stenotic artery. To be able to measure the performance of tracing algorithms on real angiographic images, it is not possible to use a straight forward slope approach just as done for synthetic images, since real coronary vessels and stenoses geometry are somewhat more complex than the synthetic images. Therefore, performance on angiographic images will be determined by the judgments and evaluations of the expert interventional cardiovascular surgeon who is the co-advisor of this thesis study. Each trace will be marked as “TRUE” or “FALSE” by the expert surgeon. By dividing the number of correctly found traces to the total number of traces, mean performance of tracing algorithms would be found

for angiographic images. All types of tracing algorithms are applied for each patient and the most successful algorithm is highlighted in Table 5.7.According to the results in Table 5.7 obtained using 5 patient data, mean performance of tracing algorithm is calculated as 98.72 % by using the results of the most successful algorithm for each patient. The more the number of patients are used, the more accurate the performance of the tracing algorithms.

Table 5.7: Performance of tracing algorithms on real patient data.

	Tracing Algorithm	# of Correctly Found Traces	# of Erroneously Found Traces	Performance (%)
Patient-1	**Direct**	**47**	**0**	**100**
	Shortest	44	3	93.61
	Similar	22	25	46.8
	Hybrid	21	26	44.68
Patient-2	Direct	39	8	82.97
	Shortest	**45**	**2**	**95.74**
	Similar	38	9	80.85
	Hybrid	39	8	82.97
Patient-3	Direct	43	4	91.48
	Shortest	**47**	**0**	**100**
	Similar	10	37	21.27
	Hybrid	19	28	40.42
Patient-4	**Direct**	**47**	**0**	**100**
	Shortest	**47**	**0**	**100**
	Similar	15	32	31.91
	Hybrid	**47**	**0**	**100**
Patient-5	**Direct**	**46**	**1**	**97.87**
	Shortest	**46**	**1**	**97.87**
	Similar	16	31	34.04
	Hybrid	16	31	34.04
Mean Performance	-	46.4	0.6	**98.72**

5.6. Robustness of Hybrid Tracing Algorithm to the Orientation of the Vessel

Proposed method used for determination of traces uses an adaptive thresholding algorithm. In other words, threshold value used in the algorithm is determined adaptively with respect to the slope of the tangent lines (i.e. traces). Therefore, it is worthwhile to examine the capability of the hybrid tracing algorithm with respect to tangent lines having different slopes.

For this purpose, synthetic image in Figure 5.6 and its 30 degrees rotated form (Figure 5.18), 60 degrees rotated form (Figure 5.20), 90 degrees rotated form (Figure 5.22), 120 degrees rotated form (Figure 5.24) and 150 degrees rotated form (Figure 5.26) are used respectively. Then each time, all of the four different tracing algorithms (Direct Algorithm, Shortest Distance Algorithm, Similar Slope Algorithm, Hybrid Algorithm) are run. Corresponding results are shown in Figures 5.17, 5.19, 5.21, 5.23, 5.25, 5.27.

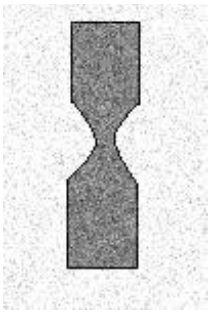

Figure 5.16: Original synthetic image

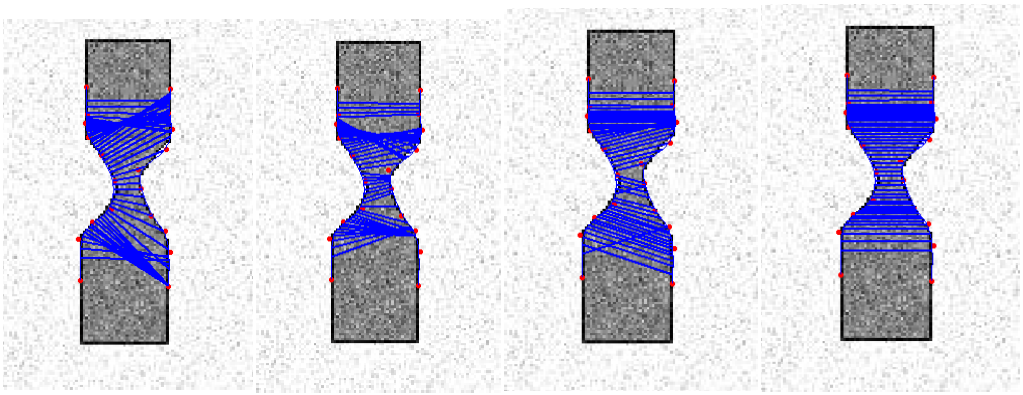

a b c d

Figure 5.17: Traces obtained using (a) Direct Algorithm, (b) Shortest Distance Algorithm, (c) Similar Slope Algorithm, (d) Hybrid Algorithm

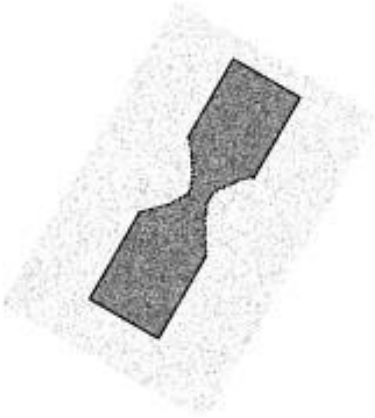

Figure 5.18: 30 degree rotated (clockwise) form of original synthetic image

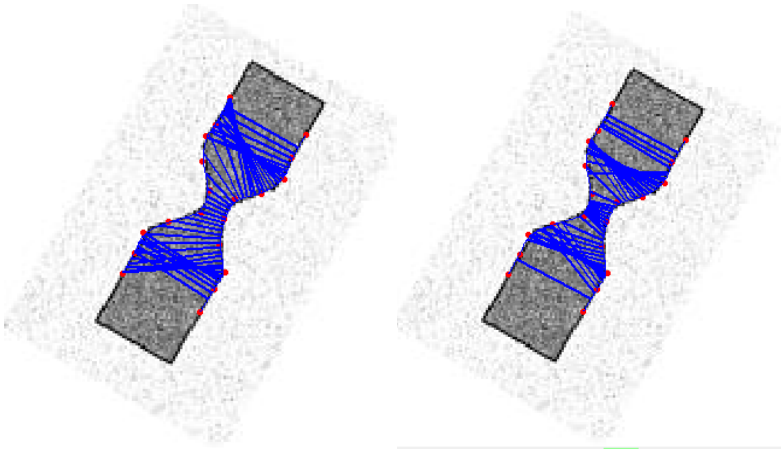

a b

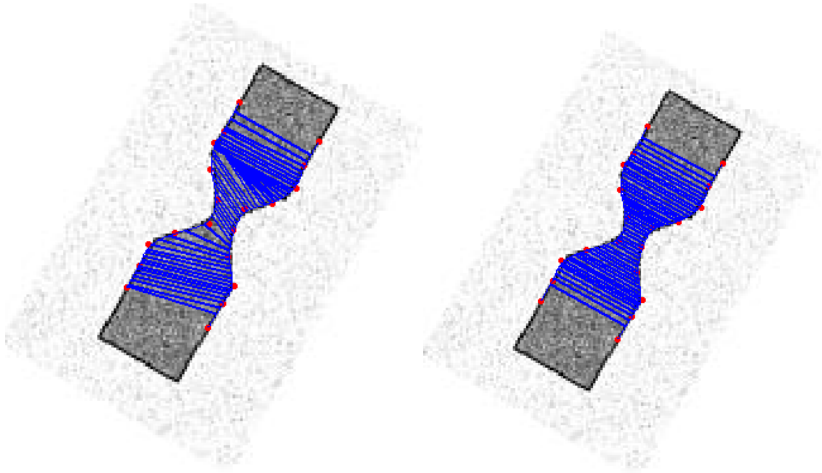

c d

Figure 5.19: Traces obtained using (a) Direct Algorithm, (b) Shortest Distance Algorithm, (c) Similar Slope Algorithm, (d) Hybrid Algorithm

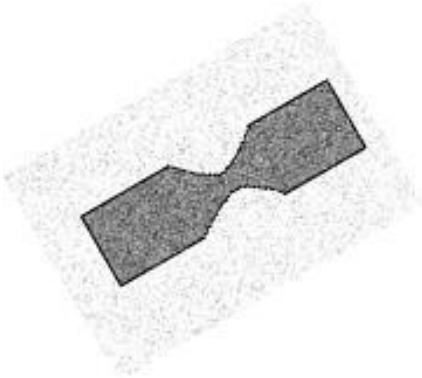

Figure 5.20: 60 degree rotated (clockwise) form of original synthetic image

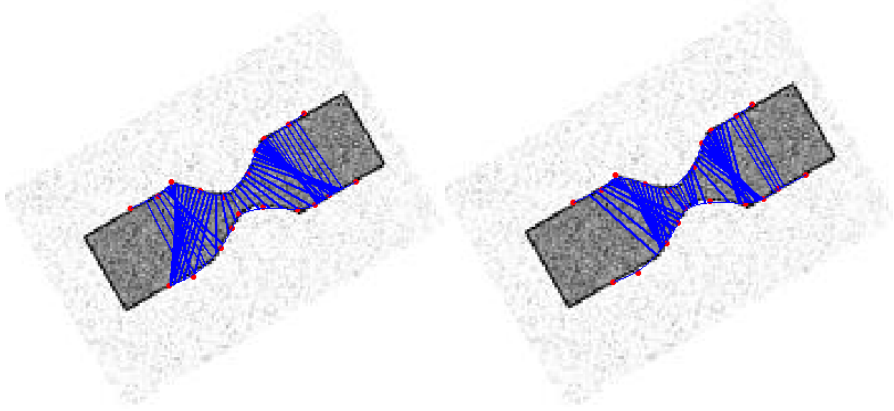

a b

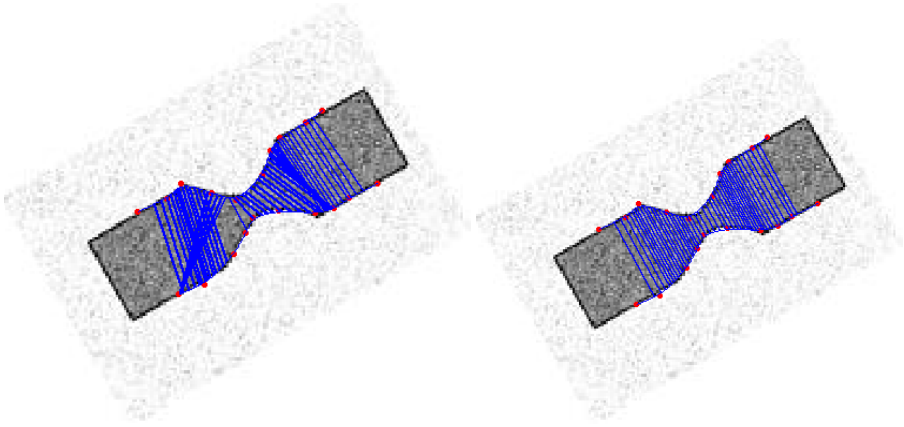

c d

Figure 5.21: Traces obtained using (a) Direct Algorithm, (b) Shortest Distance Algorithm, (c) Similar Slope Algorithm, (d) Hybrid Algorithm

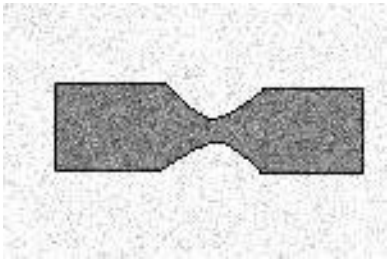

Figure 5.22: 90 degree rotated (clockwise) form of original synthetic image

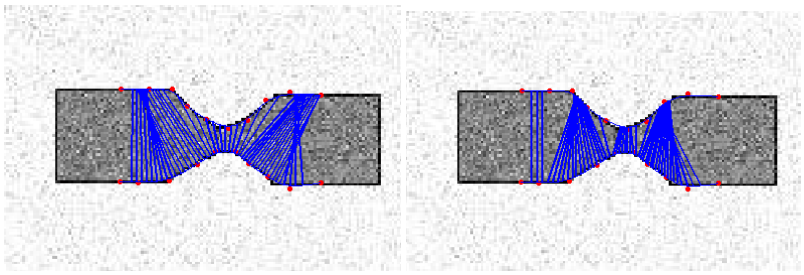

a b

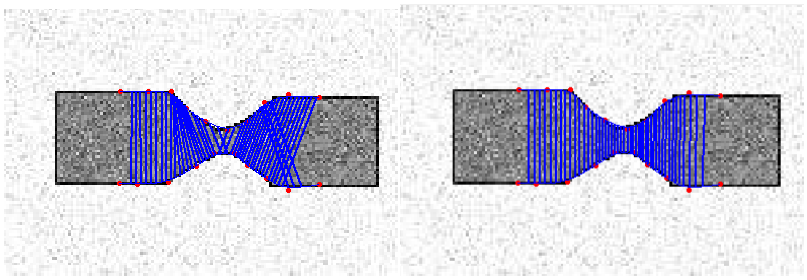

c d

Figure 5.23: Traces obtained using (a) Direct Algorithm, (b) Shortest Distance Algorithm, (c) Similar Slope Algorithm, (d) Hybrid Algorithm

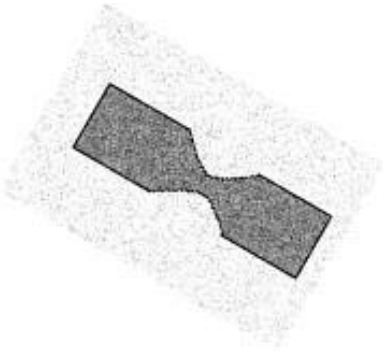

Figure 5.24: 120 degree rotated (clockwise) form of original synthetic image

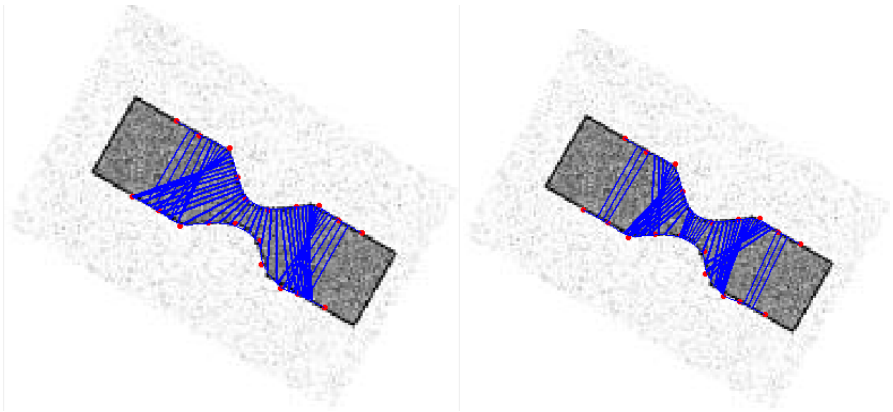

a b

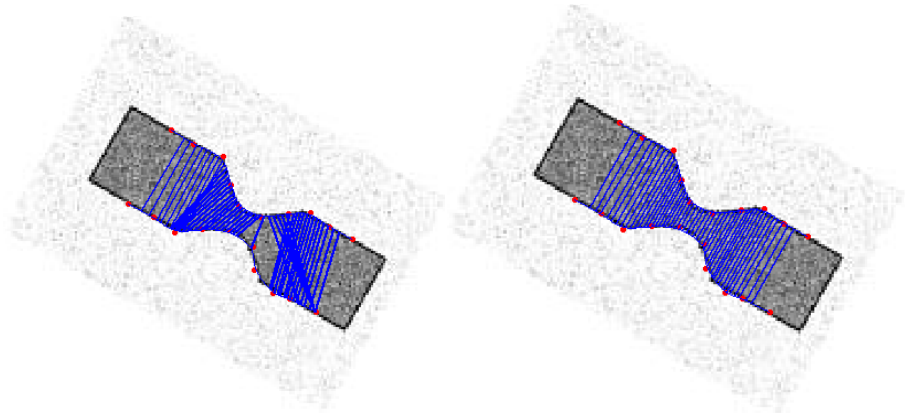

c d

Figure 5.25: Traces obtained using (a) Direct Algorithm, (b) Shortest Distance Algorithm, (c) Similar Slope Algorithm, (d) Hybrid Algorithm

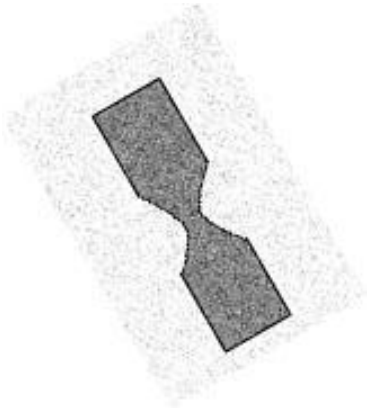

Figure 5.26: 150 degree rotated (clockwise) form of original synthetic image

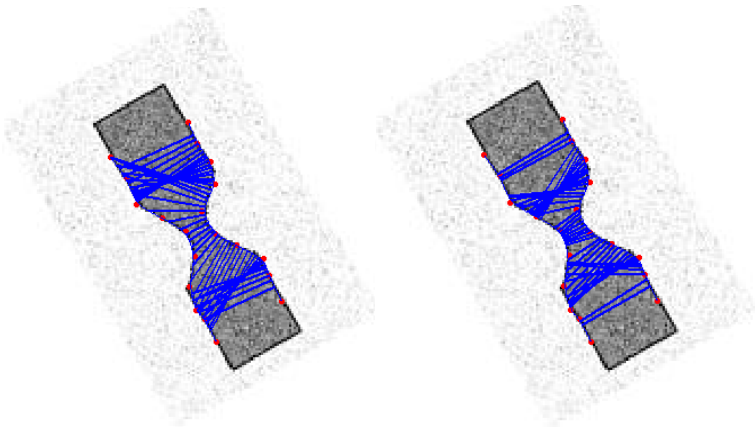

a b

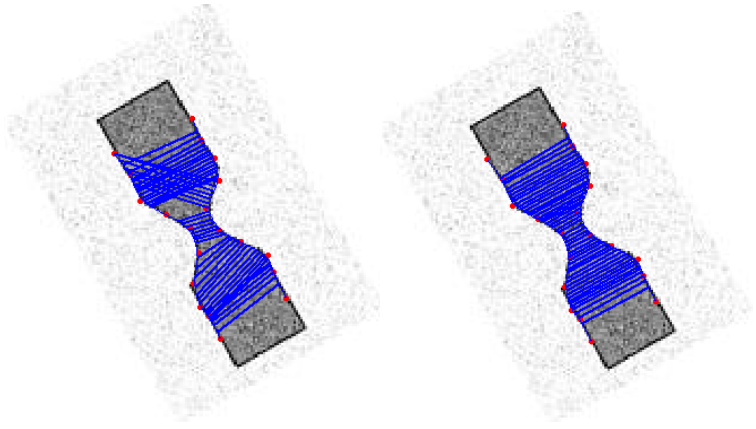

c d

Figure 5.27: Traces obtained using (a) Direct Algorithm, (b) Shortest Distance Algorithm, (c) Similar Slope Algorithm, (d) Hybrid Algorithm

When Figures 5.17 (d), 5.19 (d), 5.21 (d), 5.23 (d), 5.25 (d), 5.27 (d) are analyzed, we can easily claim that the proposed Hybrid Tracing Algorithm is rotation-

invariant. Therefore, Hybrid tracing algorithm can be used for any vessel having any orientation due to its adaptive thresholding behavior. Also, the other types of tracing algorithms, such as Direct Algorithm, Shortest Distance and Similar Slope, are also rotation-invariant due to their nature.

5.7. Performance Evaluation of Spline Fitting on Real Angiographic Images

To evaluate the performance of spline fitting part of the algorithm, data from 5 patients are used. For these 5 patients, each has a stenosis on a coronary artery and the ground truth data, which represents the vessel borders, are determined by the expert interventional cardiologist. Then, two splines are optimized and they are compared to the ground truth data using the IMP metric. Since two contours are used to represent the vessel borders (i.e. right and left spline), performance of both right and left contours are measured using the IMP metric. These performance results are tabulated in Table 5.8. Ground truth splines and optimized splines of these 5 patients are shown in Figures 5.28, 5.29, 5.30, 5.31, 5.32.

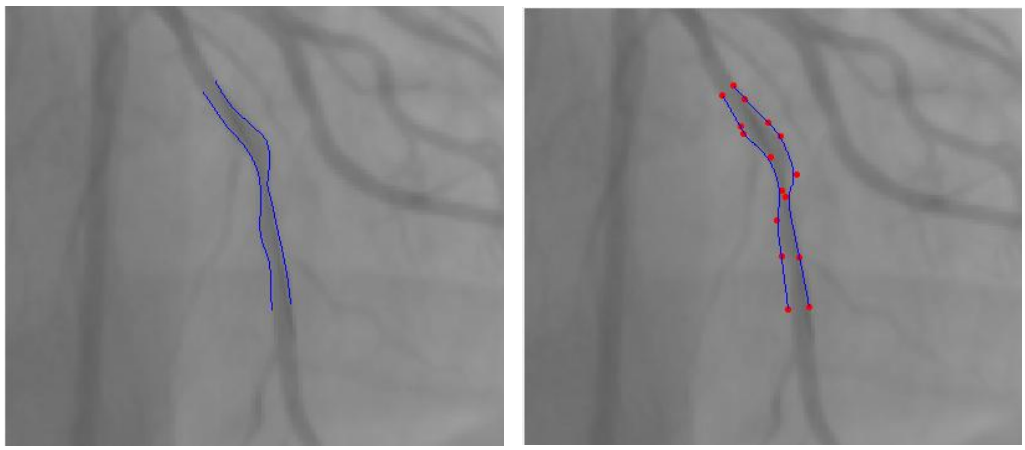

a b

Figure 5.28: (a) Ground truth splines of patient-1, (b) Optimized splines of patient-1

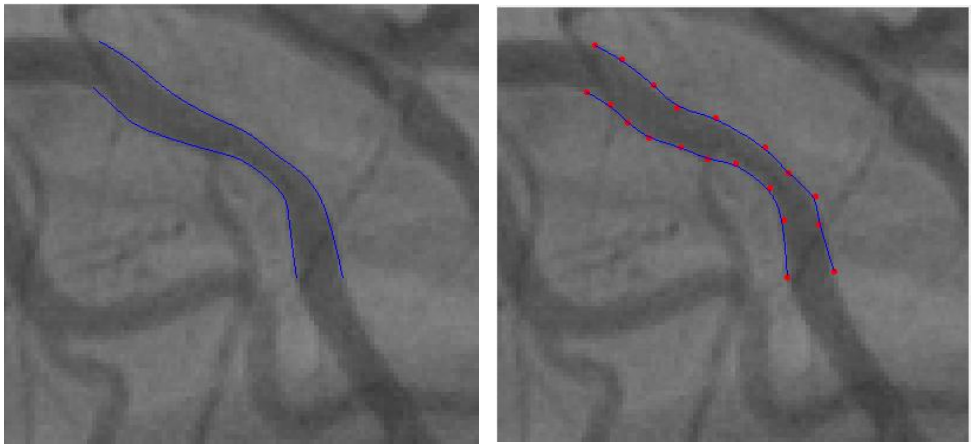

a b

Figure 5.29: (a) Ground truth splines of patient-2, (b) Optimized splines of patient-2

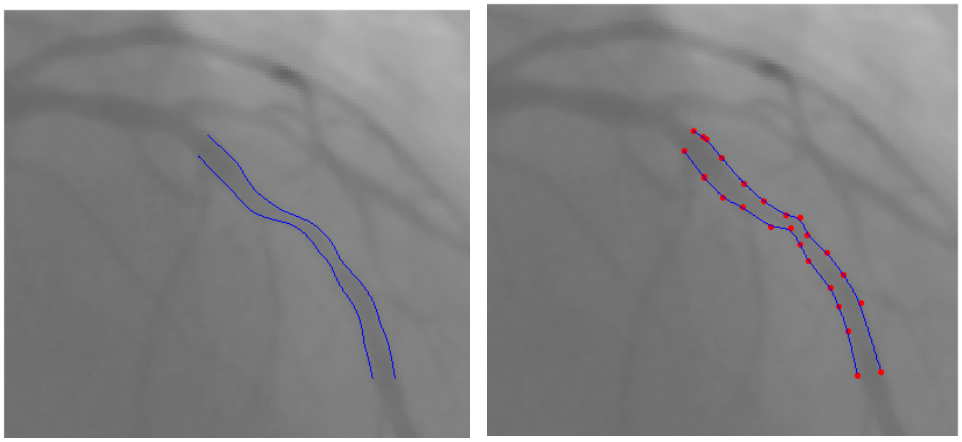

a b

Figure 5.30: (a) Ground truth splines of patient-3, (b) Optimized splines of patient-3

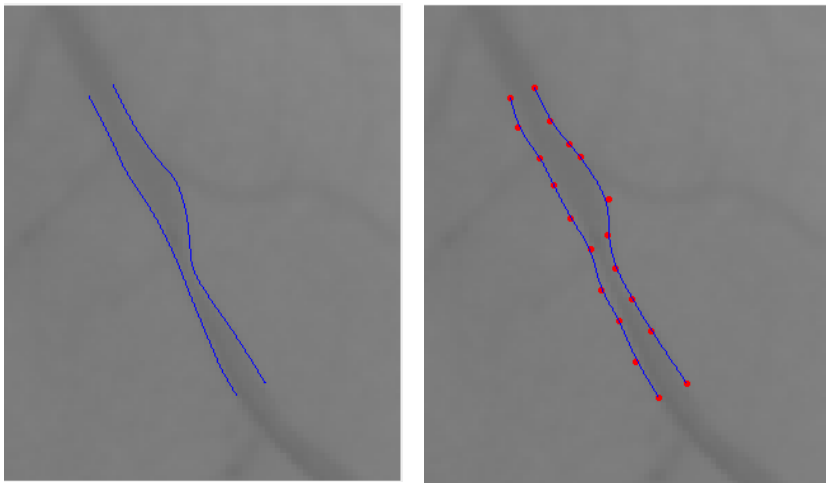

a b

Figure 5.31: (a) Ground truth splines of patient-4, (b) Optimized splines of patient-4

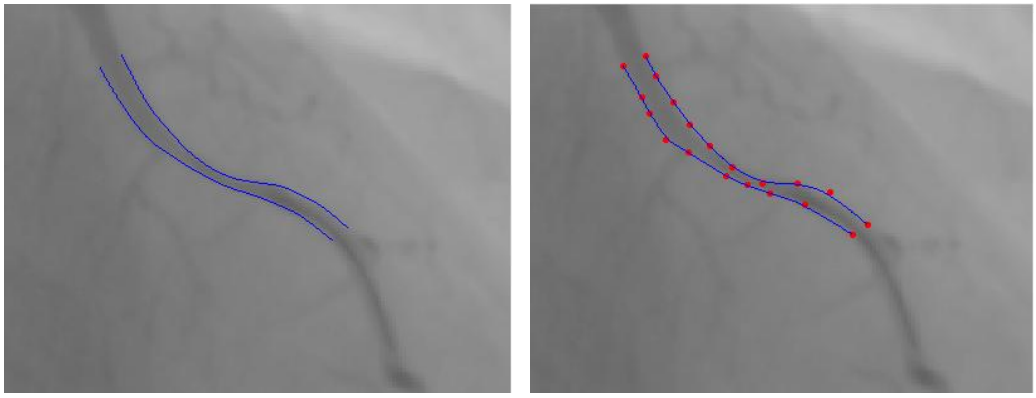

a b

Figure 5.32: (a) Ground truth splines of patient-5, (b) Optimized splines of patient-5

Table 5.8: Spline fitting performance using real patient data.

	IMP (Left Spline)	**IMP (Right Spline)**
Patient-1	0.9442	0.9120
Patient-2	0.9663	0.9772
Patient-3	0.9409	0.9495
Patient-4	0.9424	0.9743
Patient-5	0.9625	0.9714
MEAN	0.9512	0.9568

As can be seen in Table 5.8, average performance of left spline is 0.9512 and average performance of right spline is 0.9568. To evaluate the optimization performance of spline fitting for a single vessel, we can take an average of both right and left splines and obtain IMP = 0.9540. Hence we can conclude that, performance of spline fitting part of the algorithm is 95.4 %.

5.8. Time Performance Analysis of Dynamic Programming

As mentioned in Chapter 4, dynamic programming complexity is $O(n^4N)$ as proposed by **[11]**. However, we have proposed an alternative dynamic programming algorithm with a complexity of $O(n^3 + N.n)$ which has a lower complexity and hence faster than $O(n^4N)$. To show that the proposed DP algorithm is faster and hence less time-consuming, an experiment is conducted with splines having

increasing number of control points. In this experiment, optimization time of splines is measured when different DP algorithms are used. Results of this experiment are tabulated in Table 5.9.

Table 5.9: Comparison of DP algorithms having different algorithmic complexity

		$O(n^3 + N.n)$	$O(n^4N)$
# of Control Pts = 5	Time(sec)	583	171
	# of Iteration	14	4
# of Control Pts = 6	Time(sec)	168	844
	# of Iteration	4	2
# of Control Pts = 7	Time(sec)	485	2222
	# of Iteration	11	3
# of Control Pts = 8	Time(sec)	195	2961
	# of Iteration	5	3

Results shown in the Table 5.9 are obtained in MATLAB (R2011a) coding environment running on Windows 7 operating system (OS). While these time measurements are taken, there were additional parallel processes running on Windows OS. Therefore, time measurements in Table 5.6 are not so accurate but they give the essential key idea.

As the number of control points of the spline increases, spline optimization time of DP having the complexity of $O(n^3 + N.n)$ does not increase much and it is obvious that running time of this algorithm is less dependent to the number of control points compared to the DP algorithm with a complexity of $O(n^4N)$. As mentioned in Chapter 4, N is the number of control points and is n possible positions for each control point. Inversely, running time of DP having the complexity of $O(n^4N)$ drastically increases when the number of control points increases. This is also not surprising, since complexity is a function of N. In other words, running time of this algorithm increases linearly with the number of control points.

To be able to interpret the results presented in Table 5.9, another metric is needed which is independent of number of iterations, since running time is linearly

proportional to the number of iterations. Therefore, we propose a new metric to interpret the timing performance of these two DP algorithms which is Elapsed Time Per Iteration (ETPI).

$$ETPI = \frac{Total\ Elapsed\ Time}{\#\ of\ Iterations} \tag{5-8}$$

By using the results obtained in Table 5.9, ETPI (Elapsed Time Per Iteration) is calculated using the above formula and Table 5.10 is constructed.

Table 5.10: ETPI metric for splines having different number of control points.

	$O(n^3 + N.n)$	$O(n^4N)$
# of Control Pts = 5	41.64	42.75
# of Control Pts = 6	42	422
# of Control Pts = 7	44.09	740.66
# of Control Pts = 8	39	987

Now it is more convenient to interpret the timing performances of the two DP algorithms. DP having the complexity of $O(n^3 + N.n)$ has almost the same ETPI value around 42 seconds while running time of DP having the complexity of $O(n^4N)$ increases drastically up to 1000 second per iteration as the number of control points increases. Therefore, we can claim that the proposed low complexity DP algorithm is faster than high complexity DP algorithm when the number of control points in the spline is greater than five. Another advantage of the proposed DP is that its timing performance does not depend on the number of control points as much as DP with high complexity does.

5.9. Detection and Quantification of Stenosis

Detection of the stenosis is highly dependent on the traces between opposite contours. Each trace represents the diameter of the vessel at that point. Stenosis is detected by using the difference between successive trace lengths. If an abnormal difference is detected between the successive traces, that point is marked as beginning/ending point of the stenosis. If stenosis start/end points are detected

erroneously, resultant 2D quantification of the stenosis will be erroneous too; since mean diameter of non-stenotic region is calculated using the diameter values of traces which are outside of the stenotic region.

To show the stenosis detection ability of the proposed method, three different synthetic images are used which are shown in Figure 5.33 (a), Figure 5.34 (a) and Figure 5.35 (a). After the detection stage, stenoses are quantified by using the five stenosis measures namely, percent diameter stenosis (DS %), percent area stenosis (AS %), lesion length (LL), minimum lumen diameter (MLD) and minimum lumen area (MLA). In the calculation of AS % and MLA, coronary vessels are assumed to have a circular cross-section. Also intermediate steps of stenosis detection/quantification stages are shown in (b), (c), (d) parts of Figures 5.33, 5.34 and 5.35. 2D QCA measures of these three synthetic images are tabulated in Table 5.11.

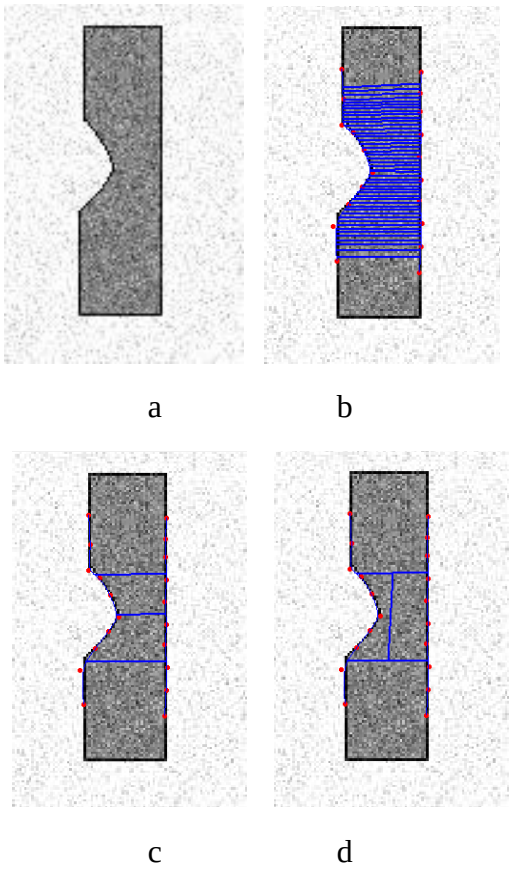

Figure 5.33: (a) Original image, (b) Traces are shown on optimized spline, (c) Detection of Stenotic region, (d) Lesion length

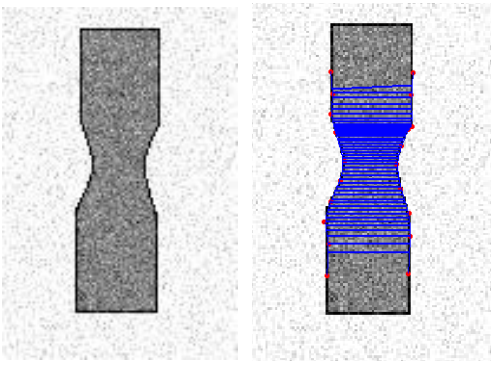

a b

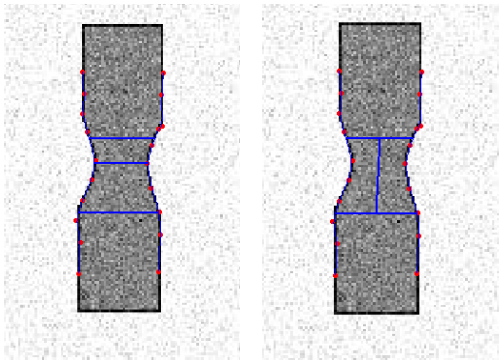

c d

Figure 5.34: (a) Original image, (b) Traces are shown on optimized spline, (c) Detection of Stenotic region, (d) Lesion length

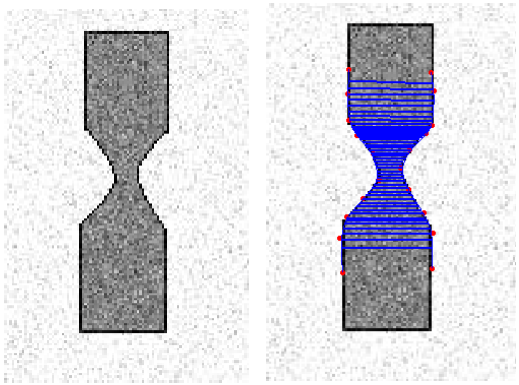

a b

Figure 5.35: (a) Original image, (b) Traces are shown on optimized spline

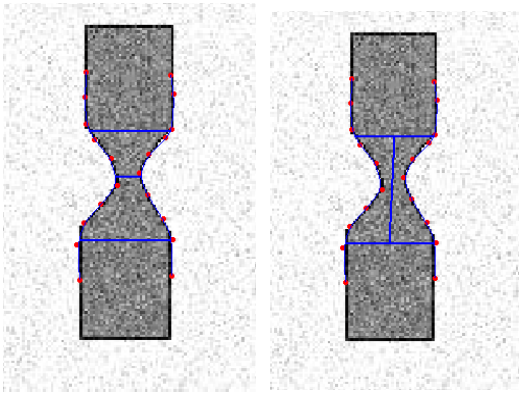

c d

Figure 5.35 (continued): (c) Detection of Stenotic region, (d) Lesion length

Table 5.11: Quantified stenosis comparison of 3 figures.

	Figure 5.33	Figure 5.34	Figure 5.35
DS (%)	37.37	30.04	69.72
AS (%)	60.77	51.06	90.83
LL (pixels)	36.9	31.64	42.21
MLD (pixels)	20.83	22.67	10.16
MLA (pixels^2)	341.08	403.97	81.14

5.10. Correlation between QCA Parameters and FFR Results

In this part, 8 different stenoses taken from randomly selected 8 different patients will be analyzed by using the proposed QCA system. These patients have also reports regarding the FFR results performed in their Left Anterior Descending arteries. Both QCA parameters and FFR values of 8 patients are shown in Table 5.12. Therefore we can compare anatomical properties of the stenosis (i.e. % AS, % DS, Lesion Length etc.) with the corresponding FFR value of the patient, which gives the real and functional significance of the stenosis. In this way, we can determine which QCA parameter is more correlated with the functional significance of the stenosis.

In this QCA analysis, image frames showing the stenotic region are selected in a manner such that the viewing angle and the frame show the most severe stenosis;

since stenosis severity is seen as more or less severe in successive frames or in different viewing angles.

Since not every tracing algorithm (i.e. Hybrid, Shortest etc.) is successful on any type of stenosis geometry, tracing algorithm which gives best representation of vessel diameter is chosen during the QCA analysis. Therefore, clinicians must apply all type of tracing algorithms and choose the one that gives the best performance among them.

During this QCA analysis, λ parameter of PMAD is not kept constant, since noise and contrast characteristics of angiographic images are very different from each other. While λ is taken as 0.05 for low noise and low contrast images, it is taken as 0.1 for high contrast and high noise images.

Table 5.12: FFR values and QCA measures of 8 patients.

	% DS	% AS	Lesion Length(LL) [pixels]	MLD [pixel]	MLA [pixel^2]	Visual Inspection (%)	FFR
Patient-1	50.46	75.45	51.75	4.39	15.2	60	0.74
Patient-2	54.21	79.03	33.00	3.19	8.01	NA	0.72
Patient-3	48.80	73.78	39.17	4.67	17.19	70	0.79
Patient-4	38.68	62.40	47.15	5.78	26.32	50	0.88
Patient-5	65.68	88.22	51.78	2.31	4.2	NA	0.74
Patient-6	62.75	86.12	44.72	2.60	5.32	70	0.86
Patient-7	39.03	62.83	50.17	4.19	13.8	NA	0.78
Patient -8	50.19	75.19	30.61	2.95	6.87	NA	0.77

For statistical analysis, sensitivity (true positive rate) and specificity (true negative rate) must be calculated. To investigate the correlation between FFR values and QCA parameters, we need to define two cutoff values for both x- and y- axis. Cutoff value

for y-axis (FFR) is the gold standard, universal and equals to 0.8. While FFR > 0.8 is an indicator of non-critical lesion, FFR < 0.8 indicates a critical lesion. Cutoff value for x-axis will be determined so that both specificity and sensitivity are optimum and high. Cutoff value in x-axis means that, any value greater than cutoff shows critical lesion and any value less than cutoff shows non-critical lesion. When cutoff values of both x and y axis are drawn, the scatter graph showing the relation between any QCA measure and FFR are divided into four regions as shown in Figure 5.36. In this way, True Positive (**TP**: Critical lesions are correctly identified as critical), True Negative (**TN**: Non-critical lesions are correctly identified as non-critical), False Positive (**FP**: Non-critical lesions are incorrectly identified as critical) and False Negative (**FN**: Critical lesions are incorrectly identified as non-critical) rates could be measured and both sensitivity and specificity can be calculated as shown in equations 5-9 and 5-10.

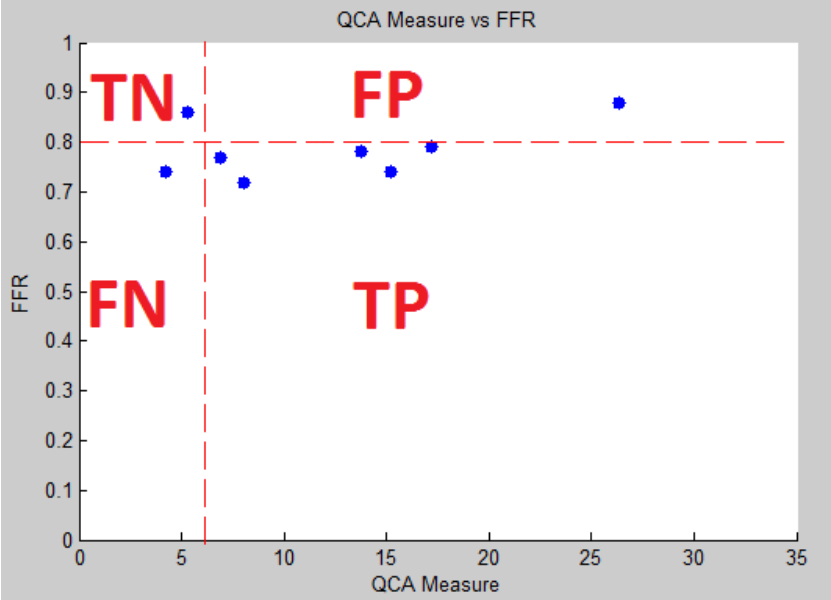

Figure 5.36: TP, TN, FP, FN regions of scatter graph.

$$Sensitivity = \frac{TP}{TP+FN} \quad (5\text{-}9)$$

$$Specificity = \frac{TN}{TN+FP} \quad (5\text{-}10)$$

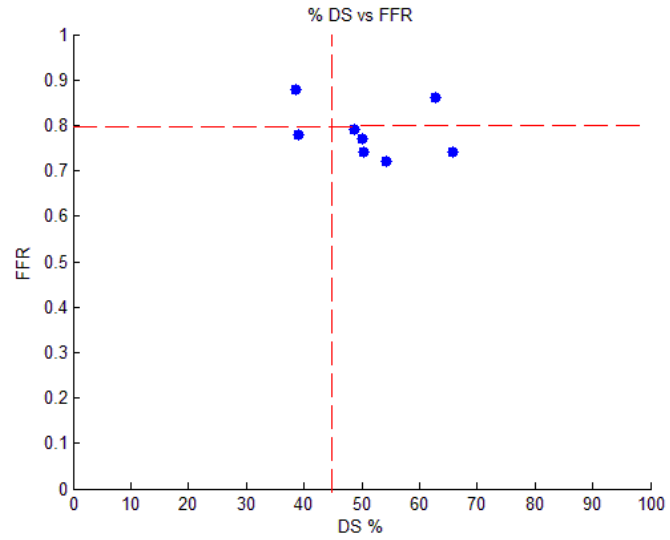

Figure 5.37: Scatter graph showing % Diameter Stenosis vs FFR when cutoff is % 45

Cutoff value for % DS which results in high sensitivity and specificity is about 45 % as shown in Figure 5.37. For this cutoff value, sensitivity and specificity are obtained as follows:

$$Sensitivity = \frac{5}{5+1} = \frac{5}{6} = 0.83$$

$$Specificity = \frac{1}{1+1} = \frac{1}{2} = 0.5$$

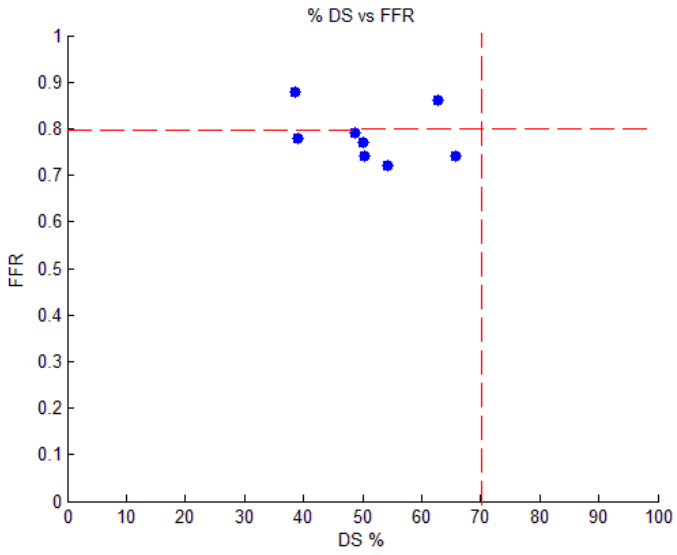

Figure 5.38: Scatter graph showing % Diameter Stenosis vs FFR when cutoff is % 70

Most widely used cutoff value in clinics is 70 % for % DS as shown in Figure 5.38. When cutoff value for % DS is 70 %, sensitivity and specificity are obtained as follows:

$$Sensitivity = \frac{0}{0+6} = 0$$

$$Specificity = \frac{2}{2+0} = \frac{2}{2} = 1$$

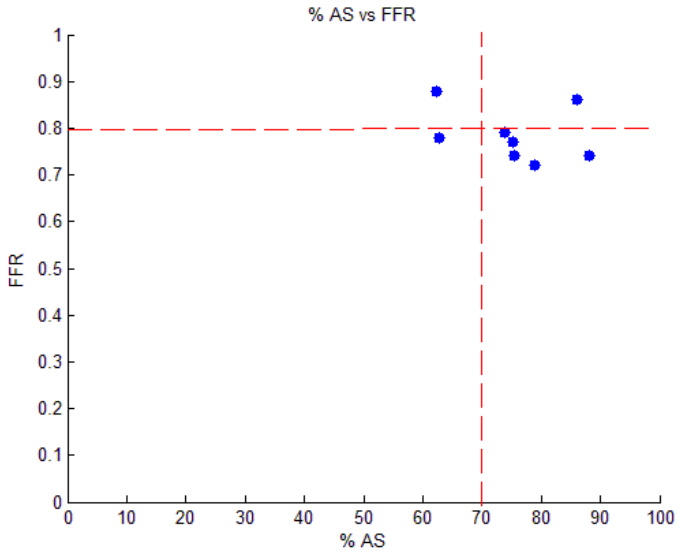

Figure 5.39: Scatter graph showing % Area Stenosis vs FFR when cutoff is % 70

Cutoff value for % AS which results in high sensitivity and specificity is about 70 % as shown in Figure 5.39. For this cutoff value, sensitivity and specificity are obtained as follows:

$$Sensitivity = \frac{5}{5+1} = \frac{5}{6} = 0.83$$

$$Specificity = \frac{1}{1+1} = \frac{1}{2} = 0.5$$

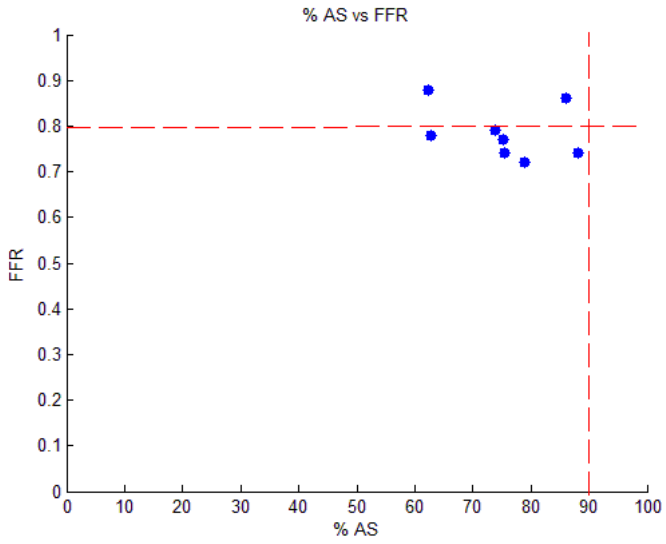

Figure 5.40: Scatter graph showing % Area Stenosis vs FFR when cutoff is % 90.

Most widely used cutoff value in clinics is 70 % for % AS as shown in Figure 5.40. When cutoff value for % AS is 90 %, sensitivity and specificity are obtained as follows:

$$Sensitivity = \frac{0}{0+6} = \frac{0}{6} = 0$$

$$Specificity = \frac{2}{2+0} = 1$$

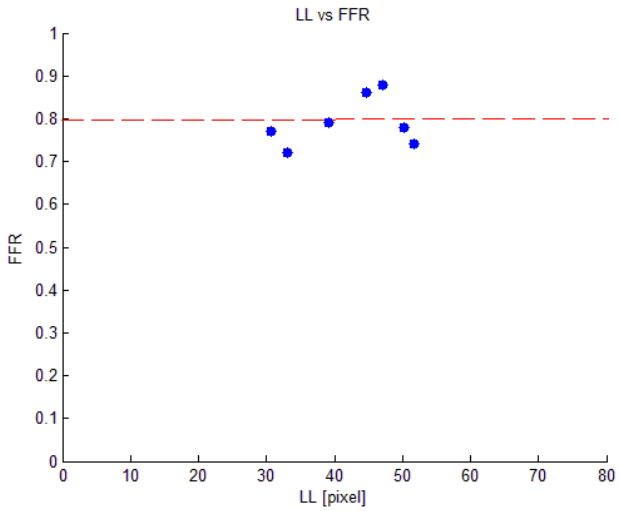

Figure 5.41: Scatter graph showing Lesion Length (LL) vs FFR.

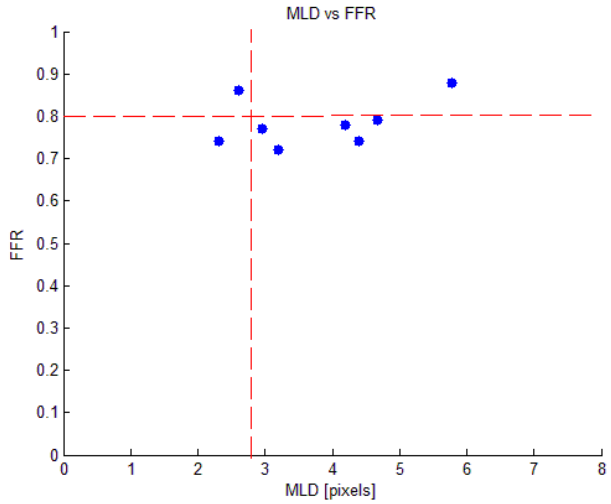

Figure 5.42: Scatter graph showing Minimum Lumen Diameter (MLD) vs FFR

Cutoff value for Minimum Lumen Diameter which results in high sensitivity and specificity is about 2.8 pixels as shown in Figure 5.42. For this cutoff value, sensitivity and specificity are obtained as follows:

$$Sensitivity = \frac{5}{5+1} = \frac{5}{6} = 0.83$$

$$Specificity = \frac{1}{1+1} = \frac{1}{2} = 0.5$$

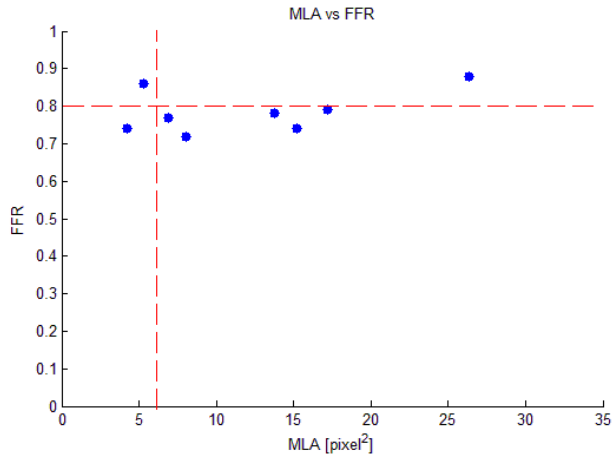

Figure 5.43: Scatter graph showing Minimum Lumen Area (MLA) vs FFR

Cutoff value for Minimum Lumen Area which results in high sensitivity and specificity is about 6 pixel^2 as shown in Figure 5.43. For this cutoff value, sensitivity and specificity are obtained as follows:

$$Sensitivity = \frac{5}{5+1} = \frac{5}{6} = 0.83$$

$$Specificity = \frac{1}{1+1} = \frac{1}{2} = 0.5$$

The cutoff values for % DS and % AS which result in high sensitivity and specificity are 45 % and 70 % respectively. With these cutoff values, sensitivity and specificity are calculated as 83 % and 50 %. However, most of the cardiologists use cutoff values for % DS and % AS as 70 % and 90 % respectively. With these cutoff values, sensitivity and specificity are calculated as 0 and 1.

The relation between Lesion Length (LL) and FFR is displayed in Figure 5.41. Cutoff value which results in high sensitivity and specificity is around 47 pixels length. With this cutoff value sensitivity and specificity are calculated as 0.4 and 0.5 respectively. These values are not high enough and we can conclude that there is no promising correlation between Lesion Length and FFR with these little patient group.

Although sensitivity and specificity are found as 0.83 and 0.5 for the relations between MLD vs FFR and MLA vs FFR, it makes much sense when these measurements are performed in the same part of the coronary tree. Since vessel diameter varies much from the upper part to the lower part of the coronary tree. In our experiment, stenoses are selected from any part of the coronary tree randomly.

5.11. Comparison with Commercial QCA Systems

2D QCA systems similar to the one that we have proposed are also commercially available in the market. The most commonly used and validated QCA products are QAngio XA (Medis, Leiden, The Netherlands) and CAAS (PIE Medical, Maastricht, The Netherlands) **[58]** which are shown Figure 5.44 and Figure 5.45 respectively. In this section, we will compare the capabilities and features of the QCA system we have proposed with those which are commercially available.

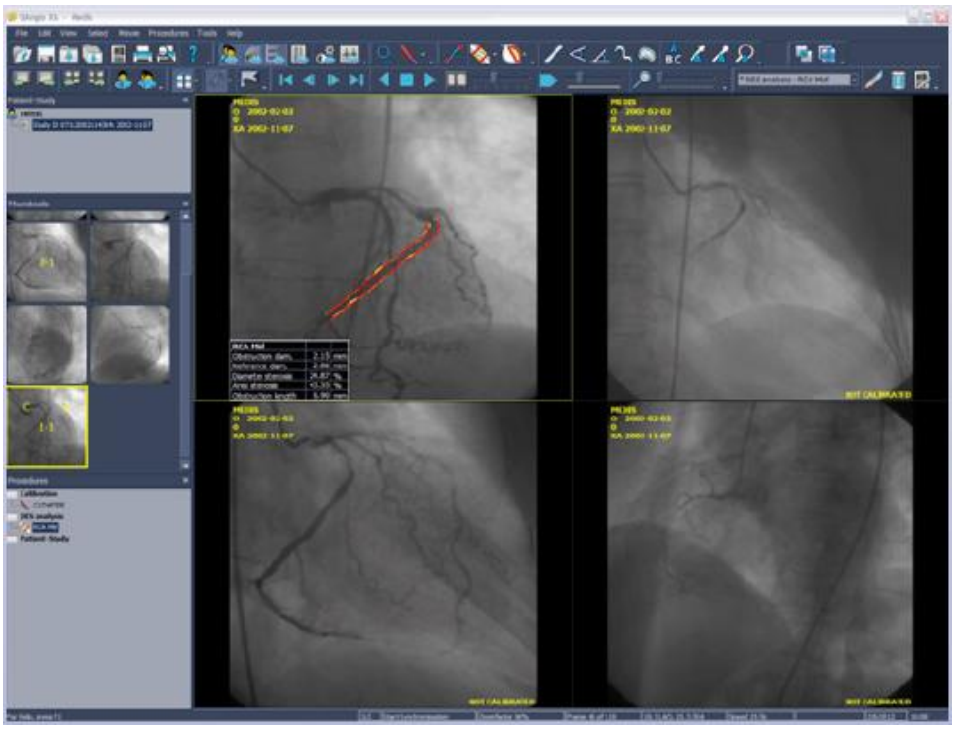

Figure 5.44: GUI of QAngio XA [60]

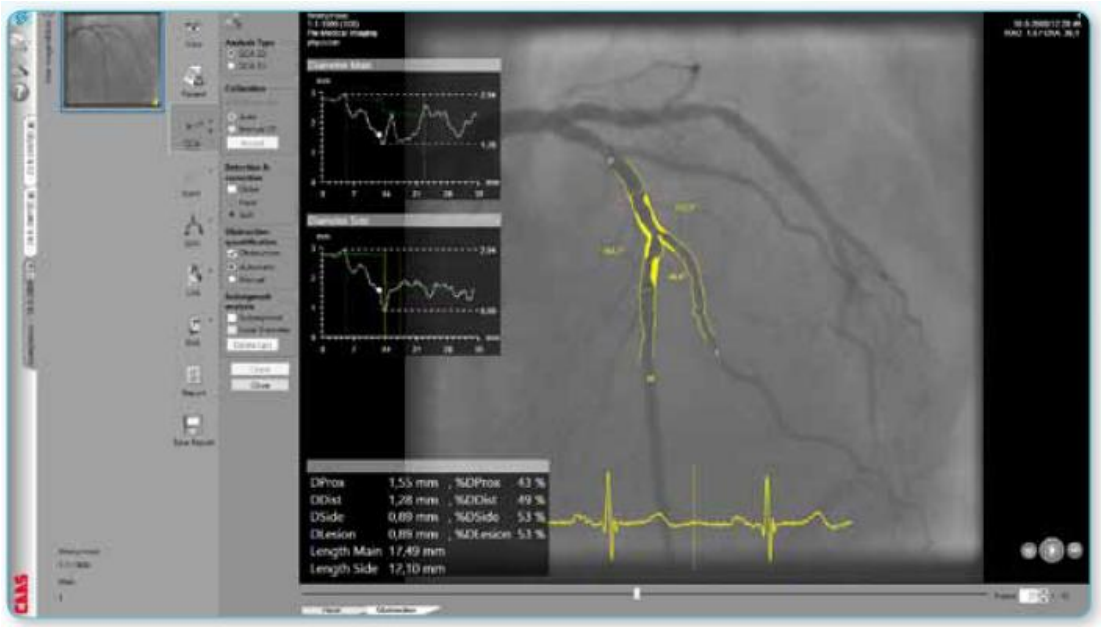

Figure 5.45: GUI of CAAS QCA [59]

Table 5.13: Feature comparison of proposed QCA with contemporary commercial QCA systems

	CAAS QCA	**QAngio XA**	**Proposed QCA**
Company	PIE MEDICAL IMAGING	MEDIS	N/A
Country	Netherlands	Netherlands	Turkey
Vessel Contour Extraction	YES	YES	YES
% Diameter Stenosis	YES	YES	YES
Lesion Length	YES	YES	YES
Min Lumen Diameter	YES	YES	YES
Validation	YES	YES	NO
Stenosis Detection	YES	YES	YES
GUI	YES	YES	YES
Image Export	NO	YES	YES
Reporting	YES	YES	YES
Diameter Profile	YES	YES	YES
Semi –Automatic	YES	YES	YES
DICOM Viewer	YES	YES	YES

As can be seen in Table 5.13, our QCA system has all of the key features and capabilities of the commercial QCA systems. Since these two systems are commercial, they may have more detailed features than the proposed QCA system, but the core features related to the quantification of stenosis are present in our system too.

Above comparisons in Table 5.13 are made according to the documents which are available on the websites of the products **[59] [60]**. For more information about the above QCA systems, their websites can be visited. Also 3D QCA tools of both QCA systems are available in the market.

CHAPTER 6

CONCLUSION

6.1. Summary

We have proposed a semi automatic 2D QCA system for the extraction of coronary vessels and hence for the detection of stenosis by means of anatomical properties of a stenotic coronary artery. This proposed system is an ultimate need especially for interventional cardiologists who need to quantify the severity of a stenosis by visual inspection since they do not have any type of QCA system. Quantification of severity of a coronary stenosis is extremely crucial for the patient who has a cardiovascular disease. According to the level of severity of the stenosis, cardiologists make a choice between Percutaneous Coronary Intervention (PCI), By-pass operation or medical treatment as a treatment planning procedure. Assisting the clinicians for treatment planning with software which detects and identifies severity of the stenosis quantitatively is a very powerful remedy.

As a first step into the QCA system, we have developed a DICOM viewer which enables the user to view, read, navigate, manipulate and work on the angiographic frames embedded inside the DICOM file. Although most of the clinicians do not have a QCA system, they have a DICOM viewer (free or commercial) to be able to see the images taken from an angiography procedure. For detailed information and capabilities about the developed DICOM viewer, which is only a part of our GUI, Appendix B could be visited.

The method we have proposed for the extraction of coronary vessels and for the detection and quantification of stenosis include many novelties and differences with respect to the current literature inside it.

The first novelty presented in the method is assisting the clinician in the spline initialization procedure by supplying a contrast enhanced environment via an

adaptive histogram equalization method. In this way, clinicians initialize the splines in a contrast enhanced environment carefully.

Another novelty is the application of Perona-Malik anisotropic heat diffusion equation (filter) to the XRA images as a pre-processing step so that responses taken from differently oriented Gabor filters and from Canny edge detector give better localized edge features of the coronary vessels. Localized edges will then be very important in the spline fitting stage, since these edge features are used as external energy attracting the snakes on it.

Development of a low complexity and hence less time consuming Dynamic Programming (DP) algorithm is also novel to this study. The proposed DP algorithm is less robust to spline initialization type but very fast than the one existing in the literature. Since the user is an expert clinician in our case, we expect a reasonable spline initialization. By this way, we take advantage of the fast DP algorithm by only initializing splines having reasonable shape compared to the vessel edges. Furthermore, a new semi-automatic spline fitting method is proposed which is even faster than the low complexity DP algorithm.

The most original part of the proposed algorithm is the construction of traces which represent the diameter of the vessel. This part is based on an analytical geometry approach simply by obtaining slope on the vessel edge, determining a line perpendicular to this slope and finding the intersection point of the perpendicular line with the opposite vessel edge. After an intersection point is found on the other spline (vessel edge), a trace search is done within a search window to look for the shortest distance or similar slope. Also a hybrid algorithm is developed by using best parts and eliminating the bad parts of shortest distance and similar slope algorithms.

Finally, QCA parameters of 8 patients are measured and compared with the FFR results of the same patients. In this way, relationships between QCA parameters and FFR values are examined by looking at sensitivity and specificity values.

By using the aforementioned capabilities and methods via a user-friendly GUI, interventional cardiologists are capable of determining anatomical properties of a stenotic lesion such as percent diameter stenosis (DS %), percent area stenosis

(AS %), lesion length (LL), minimum lumen diameter (MLD) and minimum lumen cross-sectional area (MLA) quantitatively rather qualitatively.

6.2. Future Work

PMAD with an adaptive λ parameter as a function of image contrast and image noise level could be developed. In this way, user interaction is reduced and proposed method would be more automatic.

To increase the repeatability performance of the QCA parameters, a new method could be developed instead of proposed tracing algorithms. In section 5.5, performance of tracing algorithms is found as 93.61 %. Any other method having higher performance rate is welcome which would also result in more accurate and repeatable QCA results.

In QCA analysis, single frame is used for stenosis quantification. Instead of single frame, successive frames or frames from different viewing angles could be used for stenosis quantification. Since using successive frames mean video processing in angiographic frames, video processing methods could be developed for stenosis quantification.

To investigate the correlation between QCA parameters and FFR results, more patient data must be studied with the proposed QCA system so that more concrete and conclusive correlations are found. Using only 8 patient data is insufficient to draw concrete correlations.

As explained in the RESULTS chapter, the QCA system we have proposed has almost all of the features and capabilities of the existing commercially available 2D QCA systems. Our 2D QCA system also could be developed to be commercially available in the market.

Lastly, by using the images taken from different viewing angles of 3DRA; a 3D QCA system can be developed, since the results presented by 2D QCA systems are limited and there are commercially available 3D QCA systems in the market.

REFERENCES

[1] D. Gabor, "Theory of communication. Part 1: The analysis of information," *Electrical Engineers - Part III: Radio and Communication Engineering, Journal of the Institution of* , vol.93, no.26, pp.429,441, November 1946

[2] J. Yang, L. Liu, T. Jiang, Y. Fan, "A modified Gabor filter design method for fingerprint image enhancement", *Pattern Recognition Letters*, Volume 24, Issue 12, August 2003, Pages 1805-1817

[3] O. Alireza, S.Bita, "Retinal Vessel Extraction Using Gabor Filters and Support Vector Machines" in Advances in Computer Science and Engineering, Volume 6, 2009, pp 356-363

[4] Qin Li; J. You, D. Zhang,; Bhattacharya, P., "A Multiscale Approach to Retinal Vessel Segmentation Using Gabor Filters and Scale Multiplication", *IEEE International Conference on Systems, Man and Cybernetics* , vol.4, no., pp. 3521,3527, 8-11 Oct. 2006

[5] R. Thai, "Fingerprint Image Enhancement and Minutiae Extraction", Honours Programme, School of Computer Science and Software Engineering, The University of Western Australia, 2003

[6] J.-C. Lee ; C.-H. Lee ; C.-B. Hsu ; P.-Y. Kuei ; K.-C. Chang, "Dorsal hand vein recognition based on 2D Gabor filters", *The Imaging Science Journal*, Volume 62, Issue 3, pp. 127-138, March 2014

[7] B. Konuk, "PALMPRINT RECOGNITION BASED ON 2-D GABOR FILTERS", M. Sc. Thesis, Middle East Technical University, Turkey, January 2007

[8] S.-l. Liu, Z.-d. Niu, G. Sun, Z.-p. Chen, “Gabor filter-based edge detection: A note”, *Optik - International Journal for Light and Electron Optics*, Volume 125, Issue 15, Pages 4120-4123, August 2014

[9] Daugman, J.G., "High confidence visual recognition of persons by a test of statistical independence" , *IEEE Transactions on Pattern Analysis and Machine Intelligence* , vol.15, no.11, pp.1148,1161, Nov 1993

[10] Klein, A.K.; Lee, F.; Amini, A.A., "Quantitative coronary angiography with deformable spline models" , *IEEE Transactions on Medical Imaging*, vol.16, no.5, pp.468,482, Oct. 1997

[11] Brieva, J.; Galvez, M.; Toumoulin, C., "Coronary extraction and stenosis quantification in X-ray angiographic imaging," *Engineering in Medicine and Biology Society, IEMBS '04. 26th Annual International Conference of the IEEE* , vol.1, no., pp.1714,1717, 1-5 Sept. 2004

[12] D. Brosh, S. T. Higano, R. J. Lennon, D. R. Holmes Jr., A. Lerman, “Effect of lesion length on fractional flow reserve in intermediate coronary lesions”, *American Heart Journal*, Volume 150, Issue 2, Pages 338-343, August 2005

[13] Sato, Y.; Araki, T.; Hanayama, M.; Naito, H.; Tamura, S., "A viewpoint determination system for stenosis diagnosis and quantification in coronary angiographic image acquisition" , *IEEE Transactions on Medical Imaging*, vol.17, no.1, pp.121,137, Feb. 1998

[14] J. J. Fischer, H. Samady, J. A. McPherson, I. J. Sarembock, E. R. Powers, L. W. Gimple, M. Ragosta, “Comparison between visual assessment and quantitative angiography versus fractional flow reserve for native coronary narrowings of moderate severity”, *The American Journal of Cardiology*, Volume 90, Issue 3, Pages 210-215, 1 August 2002

[15] World Health Organization, Available at : http://www.who.int/gho/ncd/mortality_morbidity/en/ , Last Accessed in 29.11.2014.

[16] The World Bank, Available at: http://data.worldbank.org/about/country-and-lending-groups, Last Accessed in 29.11.2014

[17] M. Schrijver, "Angiographic Image Analysis to Assess the Severity of Coronary Stenoses", Ph.D. thesis, University of Twente, Netherlands, 2002

[18] R. Smithuis, T. Wilems, "Coronary Anatomy and Anomalies", Radiology Assistant, Available at: http://www.radiologyassistant.nl/en/p48275120e2ed5/coronary-anatomy-and-anomalies.html#i48d0c6d731ff8 , Last Accessed in 30.11.2014

[19] F. Faletra, N. Pandian, S. Y. Ho, "Anatomy of the Heart by Multislice Computed Tomography", West Sussex, UK, WILEY-BLACKWELL, 2008, pp 102-103.

[20] C. Erol, M. Koplay , Y. Paksoy, "Evaluation of anatomy, variation and anomalies of the coronary arteries with coronary computed tomography angiography", *Anatolian J Cardiology* ; Volume 13(2), Pages 154-64, March 2013

[21]http://bodyandhealth.canada.com/channel_section_details.asp?text_id=5397&channel_id=2104&relation_id=85907, Last accessed in 27.04.2015

[22] http://www.nhlbi.nih.gov/health/health-topics/topics/atherosclerosis, Last accessed in 29.04.2015

[23] https://my.clevelandclinic.org/services/heart/disorders/cad/types, Last accessed in 05.02.2015

[24] M. Hamilos, A. Peace, G. Kochiadakis, E. Skalidis, A. Ntalianis, B. D. Bruyne, P. Vardas, "Fractional Flow Reserve: An Indispensable Diagnostic Tool in the Cardiac Catheterisation Laboratory", *Hellenic J Cardiol*, Volume 51, Pages 133-141, 2010

[25] M. L. MARCUS, R. F. WILSON, C. W. WHITE, "Methods of measurement of myocardial blood flow in patients : a critical review", *An Official Journal of the American Heart Association Inc.* , Volume 76, Issue 2, Pages 245-254, August 1987

[26] A. Alghamdi, M. Balgaith, A. Alkhaldi, "Influence of the length of coronary artery lesions on fractional flow reserve across intermediate coronary obstruction", *European Heart Journal Supplements*, Volume 16, Issue suppl. B, Pages B76-B79, 2014

[27] H.-S. Lim, P. A. L. Tonino , B. De Bruyne , A. S.C. Yong , B.-K. Lee, N. H.J. Pijls ,W. F. Fearon, "The impact of age on fractional flow reserve-guided percutaneous coronary intervention: A FAME (Fractional Flow Reserve versus Angiography for Multivessel Evaluation) trial substudy", *International Journal of Cardiology*, Volume 177, Issue 1, Pages 66-70, 2014

[28] N. H.J. Pijls, B. V. Gelder, P. V. der Voort, K. Peels, F. A.L.E. Bracke, H. J.R.M. Bonnier, M. I.H. El Gamal, "Fractional Flow Reserve: A Useful Index to Evaluate the Influence of an Epicardial Coronary Stenosis on Myocardial Blood Flow", *Circulation*, [On-line], Volume 92, Pages 3183-3193, 1995, Available: http://circ.ahajournals.org/content/92/11/3183.full, Last Accessed: 22.01.2015

[29]http://professional-intl.sjm.com/~/media/pro/products/vas/m-r/quantien/us-int-evidence_ffr_pa-pd.ashx?la=en-int, Last accessed in 27.04.2015

[30] J. D. Schuijf1, L. J. Shaw,W. Wijns, H. J. Lamb, D. Poldermans, A de Roos, E. E. van der Wall, J. J. Bax1, "Cardiac imaging in coronary artery disease: differing modalities", *Heart (British Cardiac Society)*, Volume 91,Issue 8, Pages 1110-7, 2005

[31] R. Heo, R. Nakazato, D. Kalra, J. K. Min, "Noninvasive imaging in coronary artery disease", *Seminars in nuclear medicine*, Volume 44, Issue 5, Pages 398-409, 2014

[32] A.F. Frangi, W.J. Niessen, M.A. Viergever, "Three-dimensional modeling for functional analysis of cardiac images, a review," *IEEE Transactions on Medical Imaging*, vol.20, no.1, Pages 2-25, Jan 2001

[33] Z. Sun, "Cardiac Imaging Modalities in the Diagnosis of Coronary Artery Disease", *Journal of Clinical & Experimental Cardiology*, Pages 1-4, 2013

[34] A.G. Fraser, P.T. Buser , J.J. Bax , W.R. Dassen , P. Nihoyannopoulos , J. Schwitter , J.M. Knuuti, M. Hoher, F. Bengel , A. Szatmari, "The future of cardiovascular imaging and non-invasive diagnosis: a joint statement", *European heart journal*, Volume 27, Issue 14, Pages 268-273, 2006

[35] A.A. Amini, T.E. Weymouth, R.C. Jain, "Using dynamic programming for solving variational problems in vision" *IEEE Transactions on Pattern Analysis and Machine Intelligence,* , vol.12, no.9, pp.855-867, Sep 1990

[36] S. Zhang, J. Wang, Y. Gong, S. Zhang, X. Zhang, X. Lan, "Image parsing by loopy dynamic programming", *Neurocomputing*, Volume 145,Issue 5, Pages 240-249, December 2014

[37] C. C.L. Wang, G. Elber, "Multi-dimensional dynamic programming in ruled surface fitting", *Computer-Aided Design*, Volume 51, Pages 39-49, June 2014

[38] P. Perona, J. Malik, "Scale-space and edge detection using anisotropic diffusion," *IEEE Transactions on Pattern Analysis and Machine Intelligence,* vol.12, no.7, pp.629,639, Jul 1990

[39] M.J. Black, G. Sapiro, D.H. Marimont, D. Heeger, "Robust anisotropic diffusion," *IEEE Transactions on Image Processing,* , vol.7, no.3, pp.421,432, Mar 1998

[40] J. A. Lee, X. Geets, V. Gregoire, A. Bol, "Edge-Preserving Filtering of Images with Low Photon Counts", *IEEE Transactions On Pattern Analysis And Machine Intelligence*, VOL. 30, NO. 6, Pages 1014-27, June 2008

[41]Hand vein recognition system with circular difference and statistical directional patterns based on an artificial neural network, 2014

[42] J. Weickert, B.M.T.H. Romeny, M.A. Viergever, "Efficient and reliable schemes for nonlinear diffusion filtering," *IEEE Transactions on Image Processing*, vol.7, no.3, pp.398-410, Mar 1998

[43] C. Lopez-Molina, M. Galar, H. Bustince, B. De Baets, "On the impact of anisotropic diffusion on edge detection", *Pattern Recognition*, Volume 47, Issue 1, Pages 270-281, January 2014

[44] O. Bonnefous, V. M. Pereira, R. Ouared, O. Brina, H. Aerts, R. Hermans, F. van Nijnatten, J. Stawiaski, D. Ruijters3, "Quantification of arterial flow using digital subtraction angiography", *Medical physics*, Volume 39, Issue 10, Pages 6264-75, 2012

[45] K.S. Rhode, T. Lambrou, D.J. Hawkes, A.M. Seifalian, "Novel approaches to the measurement of arterial blood flow from dynamic digital X-ray images", *IEEE Transactions on Medical Imaging*, Volume 24, Issue 4, Pages 500-513, 2005

[46] C. K. Zarins, C. A. Taylor, J. K. Min, "Computed fractional flow reserve (FFTCT) derived from coronary CT angiography", *Journal Of Cardiovascular Translational Research*, Vol. 6, Issue 5, Pages 708-14, 2013

[47] Computational fluid dynamics applied to cardiac computed tomography for noninvasive quantification of fractional flow reserve: scientific basis., 2013

[48] I. Waechter, J. Bredno, R. Hermans, J. Weese, D. C. Barratt, D. J. Hawkes, "Model-based blood flow quantification from rotational angiography", *Medical Image Analysis*, Volume 12, Issue 5, Pages 586-602, October 2008

[49] L. Sarry, Y. J. Peng, J. Y. Boire, "Blood flow velocity estimation from x-ray densitometric data: an efficient numerical scheme for the inverse advection problem", *Physics in Medicine and Biology*, Volume 47, Issue Num 1, Pages 149-62, 2002

[50] L. Sarry, J.-Y. Boire, M. Zanca, J.-R. Lusson, J. Cassagne, "Assessment of stenosis severity using a novel method to estimate spatial and temporal variations of blood flow velocity in biplane coronarography", *Physics in Medicine and Biology*, Volume 42, Number 8, Pages 1549-64, Aug 1997

[51] V. M. Pereira, R. Ouared, O. Brina, O. Bonnefous, J. Satwiaski, H. Aerts, D. Ruijters, F. van Nijnatten, F. Perren, P. Bijlenga, K. Schaller, K.-O. Lovblad, "Quantification of Internal Carotid Artery Flow with Digital Subtraction

Angiography: Validation of an Optical Flow Approach with Doppler Ultrasound" *AJNR Am J Neuroradiol*. , Volume 35(1), Pages 156-63, 2014 Jan

[52] P. Maday, R. Brosig, J. Endres, M. Kowarschik, N. Navab, "Blood flow quantification using optical flow methods in a body fitted coordinate system", *SPIE Medical Imaging*, San Diego, CA, USA, Feb 19-23 2014

[53] C. M. Hentschke, S. Serowy; G. Janiga; G. Rose, K. D. Tönnies, "Estimating blood flow velocity in angiographic image data" , *SPIE Proceedings*, Vol. 7964, March 2011

[54] I. W. Stehle, A. Groth; T. Bruijns, O. Brina, D. A. Ruefenacht, Z. Kulcsar, V. M. Pereira, F. Perren, D. J. Hawkes, J. Weese, "Model-based blood flow quantification from DSA: quantitative evaluation on patient data and comparison with TCCD", *SPIE Proceedings*, Vol. 8314, Feb 2012.

[55] I. A. G. Boaventura, A. Gonzaga, "Method to Evaluate the Performance of Edge Detector", *International Conference on Intelligent Systems Design and Applications*, pp. 341– 346, 2007.

[56] I. A. Abdou and W. Pratt, "Quantitative design and evaluation of enhancement/thresholding edge detectors" , *Proceedings of the IEEE*, vol. 67, no. 5, pp. 753–766, 1979

[57] S. Hueeber, J. Ballani , "B-Spline-Curve", University of Stuttgart, Available: http://m2matlabdb.ma.tum.de/download.jsp?Search=14&SearchCategory=AuthorWithFiles&AuthorName=Stefan+Hueeber&MP_ID=485, Last Accessed: 22.01.2015

[58] S. D. Tomasello, L. Costanzo, A. R. Galassi "Quantitative Coronary Angiography in the Interventional Cardiology" in Advances in the Diagnosis of Coronary Atherosclerosis, Prof. Suna Kirac (Ed.), ISBN: 978-953-307-286-9, InTech, DOI: 10.5772/20243. Available from: http://www.intechopen.com/books/advances-in-the-diagnosis-of-coronary-atherosclerosis/quantitative-coronary-angiography-in-the-interventional-cardiology, 2011, Last accessed in 27.04.2015

[59] Pie Medical Imaging B.V., Maastricht, The Netherlands, Available: http://www.piemedicalimaging.com/product/caas-workstation/qca/, Last Accessed: 22.01.2015

[60] Medis Cardiovascular Imaging, Schuttersveld 92316 XG Leiden The Netherlands, Available: http://www.medis.nl/products/qangioxa, Last Accessed: 22.01.2015

[61] Medical Dictionary, Available: http://medical-dictionary.thefreedictionary.com/, Last Accessed: 22.01.2015

[62] C. Kirbas , F. K. H. Quek, "A review of vessel extraction techniques and algorithms", *ACM Computing Surveys (CSUR)*, Volume 36, Issue 2, Pages 81-121, June 2004

[63] A. Sarwal, A. Dhawan. "3-d reconstruction of coronary arteries", *IEEE Conf. Eng. in Medicine and Bio.*, Vol. 1., Pages 504–505, 1994

[64] M. Chwialkowski, Y. Ibrahim, H. F. Li, R. Peshock, "A method for fully automated quantitative analysis of arterial flow using flow-sensitized MR images" *Comp. Med. Imag- ing and Graphics*, 20(5), 365–378, 1996

[65]N. Niki,Y. Kawata, H. Sato, T. Andkumazaki, "3d imaging of blood vessels using x-ray rotational angiographic system" *IEEE Med. Imaging Conf.* , Vol. 3, Pages 1873–1877 , 1993

[66] E. Sorantin, C. Halmai, B. Erdohelyi, K. Palagyi, L. Nyul, K. Olle, B. Geiger, F. Lindbichler, G. Friedrich, K. Andkiesler. "Spiral-ct- based assessment of tracheal stenoses using 3-d skeletonization", *IEEE Trans. on Med. Img.* , 21(3), 263–273, March 2002

[67] H. Schmitt, M. Grass, V. Rasche, O. Schramm, S. Haehnel, K. Sartor, "An x-ray- based method for the determination of the contrast agent propagation in 3-d vessel structures" *IEEE Trans. on Med. Img.* , 21(3) , 251–262, Mar 2002

[68] P. Yim, P. Choyke, R. Summers, "Grayscale skeletonization of small vessels in magnetic resonance angiography", *IEEE Trans. on Med. Img.* , Vol. 19(6), Pages 568–576, June 2000.

[69] E. Bullitt, S. Aylward,. “Analysis of time-varying images using 3d vascular models”, *Proc. Applied Imagery Pat. Recog. Works*, 9–14, 2001

[70] D. Guo, P. Richardson, “Automatic vessel extraction from angiogram images” *IEEE Comput. Cardiol.* 25, 441–444, 1998

[71] Y. Tolias, S. Panas,. “A fuzzy vessel tracking algorithm for retinal images based on fuzzy clustering”, *IEEE Trans. on Med. Img.*, Vol. 17, 263– 273, 1998

[72] S. Park, J. Lee, J. Koo, O. Kwon, S. Hong, “Adaptive tracking algorithm based on direction field using ml estimation in angiogram”, *IEEE Conference on Speech and Image Technologies for Computing and Telecommunications*, Vol. 2. 671–675, 1997

[73] U. Rost, H. Munkel, C.-E. Liedtke, “A knowledge based system for the configuration of image processing algorithms”, Fachtagung Informations und Mikrosystem Technik, 1998

[74] V. Bombardier, M. Jaluent, A. Bubel, J. Bremont, “Cooperation of two fuzzy segmentation operators for digital subtracted angiograms analysis”, *IEEE Conference on Fuzzy Systems*, 1997

[75] R. Nekovei, Y. Sun, “Back-propagation network and its configuration for blood vessel detection in angiograms”, *IEEE Trans. on Neural Nets*, 6(1) , 64–72, January 1995

[76] I. Hunter, J. Soraghan, T. Mcdonagh, “Fully automatic left ventricular boundary extraction in echocardiographic images”, *IEEE Computers in Cardiology*, Pages 741–744, 1995

[77] I. Kompatsiaris, D. Tzovaras, V. Koutkias, M. Strintzis, “Deformable boundary detection of stents in angiographic images”, *IEEE Trans. on Med. Img*., 19(6) , Pages 652– 662 , June 2000

[78] S. Ramcharitar, J. Daeman, M. Patterson, “First direct in vivo comparison of two commercially available three-dimensional quantitative coronary angiography systems” *Catheter Cardiovasc. Interv.*, 71:44–50, 2008

[79] V. Prinet, O. Monga, C. Ge, S. Xie, S. Andma, "Thin network extraction in 3d images: Application to medical angiograms", *Proc. Int. Conf. Pattern Rec.*, 386–390, 1996

[80] V. Prinet, O. Monga, J. Rocchisani, "Multi-dimensional vessel extraction using crest lines", *IEEE Conf. Eng. in Medicine and Bio.*, Vol. 1, 393–394, 1997

[81] A. Hoover, V. Kouznetsova, M. Goldbaum, . "Locating blood vessels in retinal images by piecewise threshold probing of a matched filter response", *IEEE Trans. on Med. Image*, 19, 203–210, 2000

[82] W. E. Hart, M. Goldbaum, B. Cote, P. Kube, M. R. Andnelson, "Automated measurement of retinal vascular tortuosity", *In ProcAMIA Fall Conference*, 1997

[83] S. Eiho, Y. QIAN, "Detection of coronary artery tree using morphological operator", *IEEE Comput. Cardiol.* , 24, 525–528, 1997

[84] M. Donizelli, "Region-oriented segmentation of vascular structures from dsa images using mathematical morphology and binary region growing" *In Proc. of the Works. Image Proces. For the Medicine*, Vol. 12, 1998

[85] D. Geiger, A. Gupta, L. Costa, J. Vlontzos, "Dynamic programming for detecting, tracking, and matching deformable contours" *PAMI*, 17, 3, 294–302, 1995

[86] L. Sarry, J. BOIRE, "Three-dimensional tracking of coronary arteries from biplane angiographic sequences using parametrically deformable models", *IEEE Trans. on Med. Img.* 20, 1341–1351, 2001

[87] R. Chan, W. Karl, R. LEES, "A new model-based technique for enhanced smallvessel measurements in x-ray cine-angiograms", *IEEE Trans. on Med. Image*, 19, 243–255, 2000

[88] Y. Sato , T. Araki, M. Hanayama, H. Naito, S. Tamura, "A viewpoint determination system for stenosis diagnosis and quantification in coronary angiographic image acquisition", *IEEE Trans. on Med. Img*. 17, 121–137, 1998

[89] K. Zuiderveld, "Contrast Limited Adaptive Histograph Equalization." *Graphic Gems IV*. San Diego: Academic Press Professional, 474–485, 1994

[90] Garg, Rajesh, Mittal, Bhawna, Garg, Sheetal, "Histogram Equalization Techniques For Image Enhancement" ,2011

[91] R. Dwarakish, G. S. Reddy, D. Venkat , "A Comparative Analysis of Histogram Equalization based Techniques for Contrast Enhancement and Brightness Preserving", 2014

[92] C. Tomasi and R. Manduchi, "Bilateral filtering for gray and color images," *IEEE International Conference on Computer Vision*, pp. 839–846, 1998

[93] He, Kaiming, Sun, Jian, Tang, Xiaoou, "Guided Image Filtering", 2013

[94] Garnica, Carsten, Boochs, Frank, Twardochlib, Marek "A New Approach to Edge-Preserving Smoothing For Edge Extraction and Image Segmentation" 2000.

[95] Rashmi , Mukesh Kumar, Rohini Saxena, "ALGORITHM AND TECHNIQUE ON VARIOUS EDGE DETECTION : A SURVEY", *Signal & Image Processing : An International Journal (SIPIJ)*, Vol.4, No.3, June 2013

[96] M. Nosrati , R. Karimi, M. Hariri, K. Malekian, "Edge Detection Techniques in Processing Digital Images : Investigation of Canny Algorithm and Gabor Method", *World Applied Programming*, Vol (3), Issue (3), March 2013. 116-121 ISSN: 2222-2510

[97] M. Kass, A. Witkin, D. Terzopoulos, "Snakes: Active contour models*"*, *International Journal of Computer Vision*, 1(4): 321-332, 1998

[98] O. Coulon, S.J. Hickman, G.J. Parker, G.J. Barker, D.H. Miller, S.R. Arridge, "Quantification of spinal cord atrophy from Magnetic Resonance Imaging via a B-Spline Active Surface Model" *Magn. Res. in Medicine*, 47(6): 1176-1185, 2006

[99] G. Navarro, "A guided tour ton approximate string matching", *ACM Computing survey*, 33 (1),pp 31-88, 2001

APPENDIX A

Glossary of Medical Terminology

This appendix is prepared for those who have not any medical background related to cardiovascular anatomy and physiology to assist for better understanding of this thesis study. Source of this glossary is a web-based medical dictionary **[61]** which combines the definitions from many other medical dictionaries.

Atherosclerosis: Atherosclerosis is the build up of a waxy plaque on the inside of the blood vessels. In Greek, athere means gruel, skleros means hard. Atherosclerosis is often called arteriosclerosis. Arteriosclerosis (from the Greek arteria, meaning artery) is a general term for hardening of the arteries. Arteriosclerosis can occur in several forms, including atherosclerosis.

Bifurcation: The point at which division into two branches occurs.

Foreshortening: Distortion that gives the appearance of decreased depth in an image that is being studied radiographically.

Hyperaemia: An excessive amount of blood in an organ or part

Ischemia: Ischemia is an insufficient supply of blood to an organ, usually due to a blocked artery.

Non-Communicable Disease: A non-communicable disease, or NCD, is a medical condition or disease, which by definition is non-infectious and non-transmissible among people.

Percutaneous : Performed through the skin.

Percutaneous Coronary Intervention (PCI or angioplasty with stent): Percutaneous Coronary Intervention (PCI) commonly known as coronary angioplasty

or simply angioplasty, is a non-surgical procedure used to treat the stenotic (narrowed) coronary arteries of the heart found in coronary heart disease.

Revascularization: To reestablish the blood supply to (an organ or bodily part), especially by surgical procedure.

Stenoses: Plural of stenosis

Stenosis: An abnormal narrowing or contraction of a duct or canal.

Vasodilation: Dilation of a blood vessel, as by the action of a nerve or drug.

APPENDIX B

Graphical User Interface (GUI)

Since our proposed algorithm is not fully automatic, user interaction with our Graphical User Interface (GUI) should be a user-friendly one. Because of this reason, our GUI has warning dialog boxes to warn the user, progress bars to inform the user about the ongoing process, message boxes to guide the user etc.

This section serves also as a user guide.

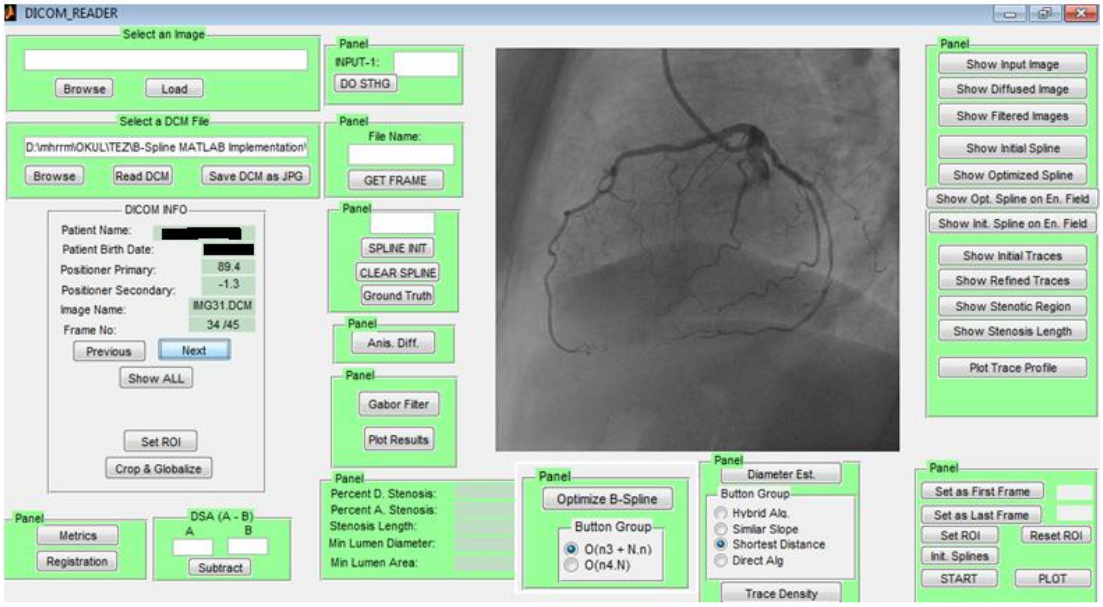

Figure B.1: Overall apperance of GUI.

B.1. Image Selection

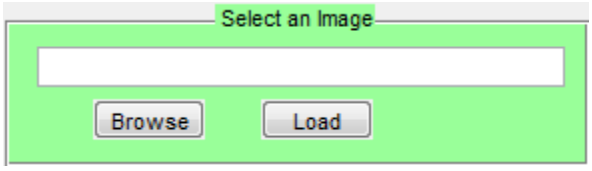

Figure B.2: Image selection panel.

User can work on JPG, PNG, BMP etc. images by just selecting the desired image from any directory.

- **Browse**: By clicking this button a window is opened so that the user can select an image from any directory. After this button is clicked below window is opened. Now the user is free to choose any type of image.

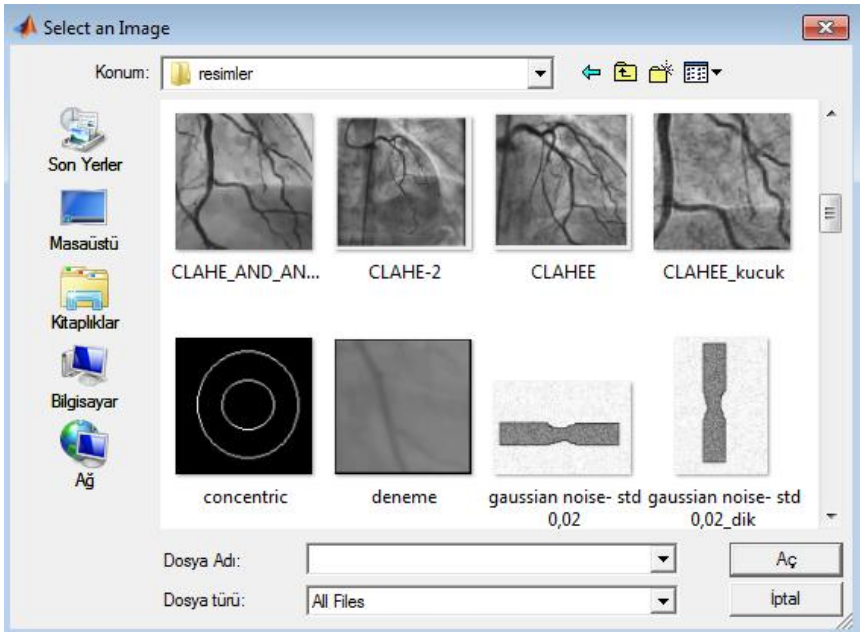

Figure B.3: Window opened after clicking the button "Browse".

- **Load**: After the desired image is selected, user has to click on this button so that selected image is loaded to the system and displayed on the GUI.

B.2. DICOM Reader

As mentioned earlier in the Contribution section, a DICOM reader is a must and a prerequisite for medical images to be worked on. Therefore, my GUI includes an embedded DICOM Reader which can be used as a stand alone tool.

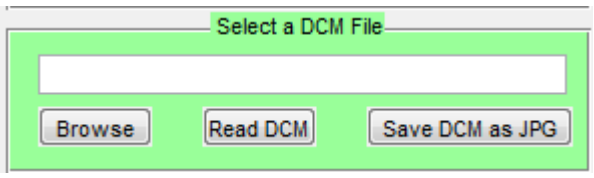

Figure B.4: DICOM file selection panel.

- **Browse**: By clicking this button a window is opened so that the user can select an DICOM file (*.dcm) from any directory. After this button is clicked below window is opened. Now the user is free to choose any DICOM file of any patient.

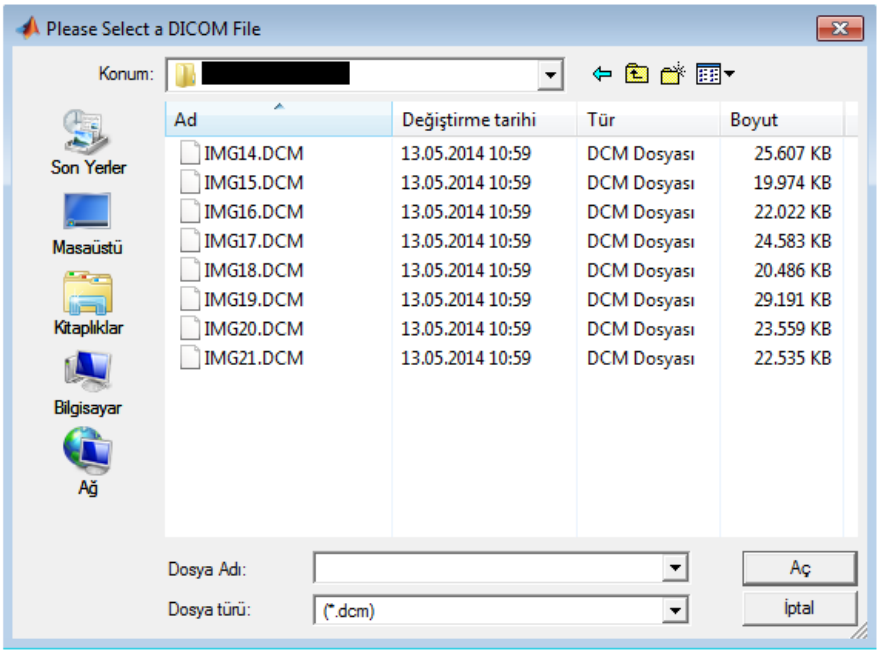

Figure B.5: Window opened after clicking the button “Browse”.

- **Read DCM**: Selected DICOM file is read after this button is clicked. During the reading operation, a progress bar is displayed as follows:

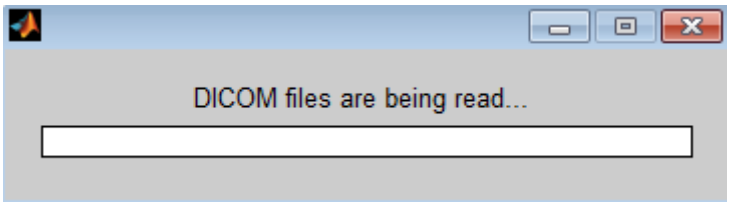

Figure B.6: Progress bar displayed during reading of DICOM file.

- **Save DCM as JPG**: DICOM files consist of many frames taken successively in time. If the user wants to save each frame inside the the DICOM in JPG format, clicking on this button is necessary. All frames are saved into the current folder of MATLAB.

B.3. DICOM Info Display Area

DICOM files include many information related with the patient and imaging parameters. Some of them are displayed to the user: Patient name, patient birth date, image name, frame number, image acquisitian angles etc. as shown in the below figure.

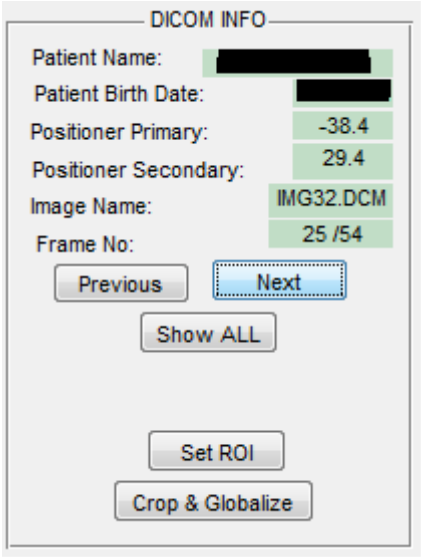

Figure B.7: DICOM info display area.

- **Previous / Next:** By clicking these two buttons, the user can navigate in between the frames embedded in DICOM file.
- **Set ROI:** Generally, the clinicians are interested in a specific ROI (Region Of Interest) in which a stenosis exists. By selecting a ROI, user saves time by avoiding to run the algorithm for unnecessary parts of the image.

After this button is clicked, warning diolog boxes as shown in the below figure is displayed to guide the user.

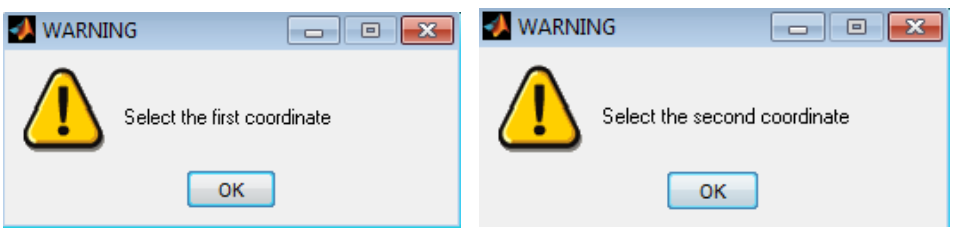

a b

Figure B.8: Warning dialog boxes for (a) first coordinate, (b) second coordinate.

After two coordinates of the ROI is entered, ROI is displayed as a blue frame on the image.If the user wants to change the ROI, s/he can click again the same button and select the two coordinates.

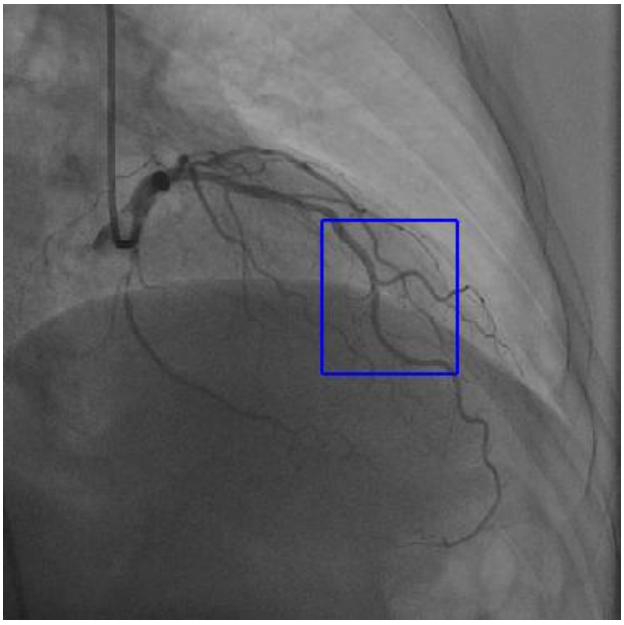

Figure B.9: Selected ROI on an image

- **Crop & Globalize**: After a ROI is selected, user can crop and globalize the ROI by clicking on this button.

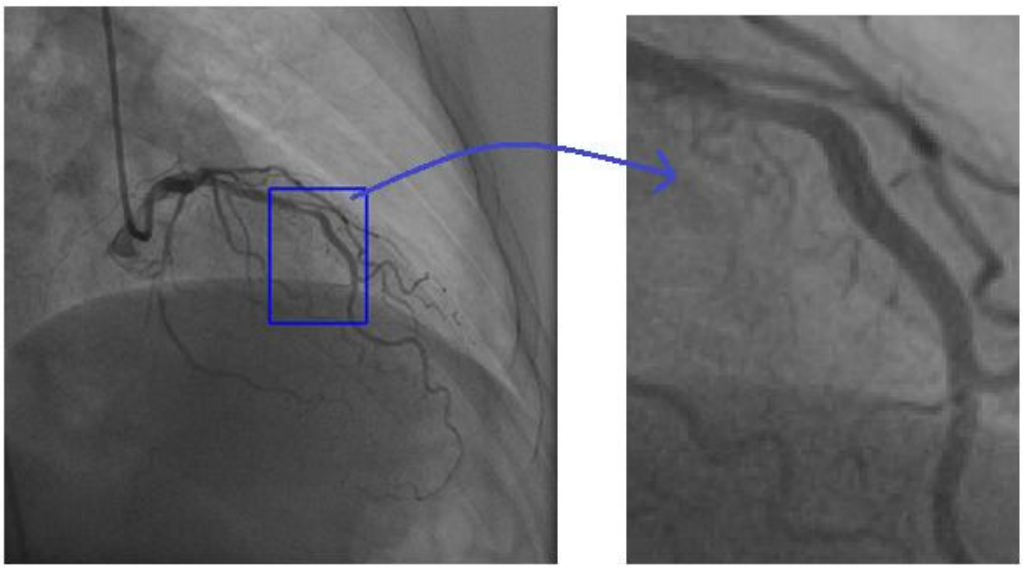

Figure B.10: Cropping the image after a ROI is selected.

B.4. Spline Initialization Panel

This panel is used for spline initialization in user-defined number of control points**.**

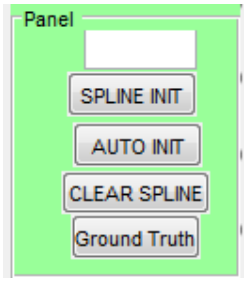

Figure B.11: Spline Initialization Panel

- **SPLINE INIT:** After this button is clicked, the user is expected to enter control points as the number entered in the related box for each spline.

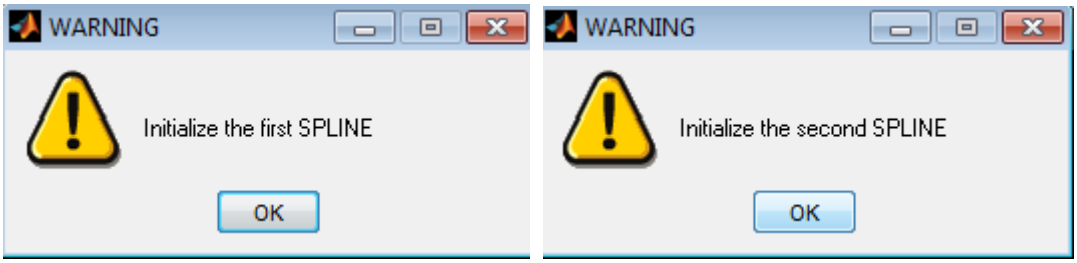

Figure B.12: Warning dialog boxes guiding the user about spline initialization

- **AUTO INIT**: This button is used for Fast Semi-automatic Spline Fitting part of the algorithm.
- **CLEAR SPLINE:** Clicking this button clears the constructed splines.
- **Ground Truth:** This button is used for the determination of ground truth spline by the expert clinicians.

B.5. Anisotropic Diffusion Panel

This panel is used for Perona-Malik anisotropic diffusion.

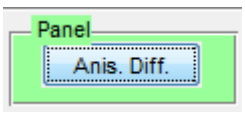

Figure B.13: Anisotropic Diffusion panel.

- **Anis. Diff.**: By clicking this button, Anisotropic diffusion is applied onto the selected image/ROI.

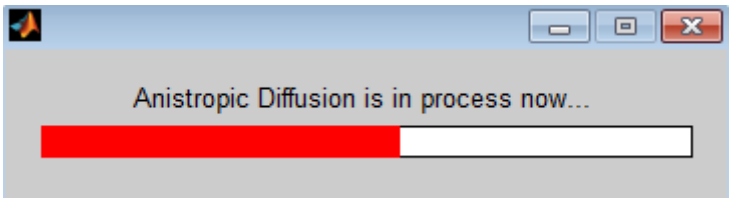

Figure B.14: Progress bar for Anisotropic diffusion.

B.6. Gabor Filtering Panel

This panel is used to construct the energy field using the responses obtained from a family of Gabor filter.

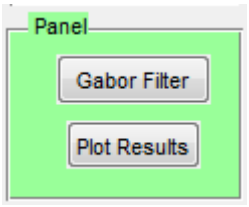

Figure B.15: Gabor filtering panel.

- **Gabor Filter:** Clicking on this button constructs the energy field using the responses of Gabor filters. Gabor filters are applied on the Anisotropic diffused image.
- **Plot Results:** This button is used to display the individual responses of each Gabor filter.

B.7. Spline Optimization Panel

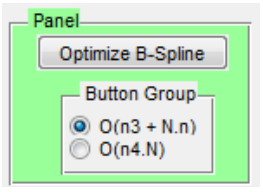

Figure B.16: Spline Optimization Panel

After Anisotrpic diffusion and Gabor filtering is applied, initialized splines are optimized using Dynamic Programming (DP) having different algorithmic complexities.

- **Optimize B-Spline:** After this button is clicked, initialized splines start to be optimized according to the DP complexity chosen by the user. For each DP complexity, different information is displayed accordingly. For DP with low complexity, spline number, iteration number and the energy difference between consecutive splines are displayed. For DP with high complexity, in addition to those information, subspline number is displayed.

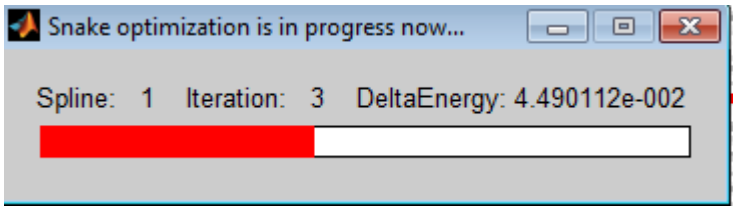

Figure B.17: Progress bar appers when optimization is in progress with DP

B.8. Trace Profile Panel

In this panel, the user can obtain the traces which represent the diameter length of the vessel through the vessel according to the chosen algorithm (i.e. Direct, Shortest Distance, Similar Slope, Hybrid Alg.).

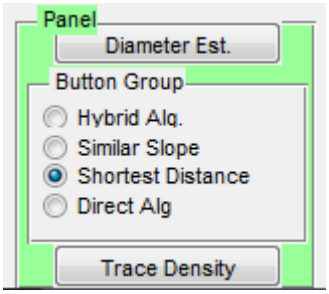

Figure B.18: Trace Profile Panel

- **Diameter Est.:** By clicking this button, trace profile of the vessel is drawn according to the algorithm selection of the user. Naturally, trace profiles are constructed by using the optimized splines, not initalized ones.

B.9. Stenosis Characteristics Panel

After all of the previously mentioned steps are performed sequentially, anatomic properties of the stenosis is extracted and displayed on this panel as shown in the below figure.

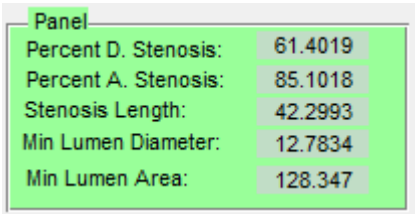

Figure B.19: Stenosis characteristics panel

B.10. Selective Display Panel

Using buttons on this panel, user can display any image that is obtained in any intermediate step of the algorithm. This panel makes our algorithm transparent to the user by showing the intermediate steps of the algorithm.

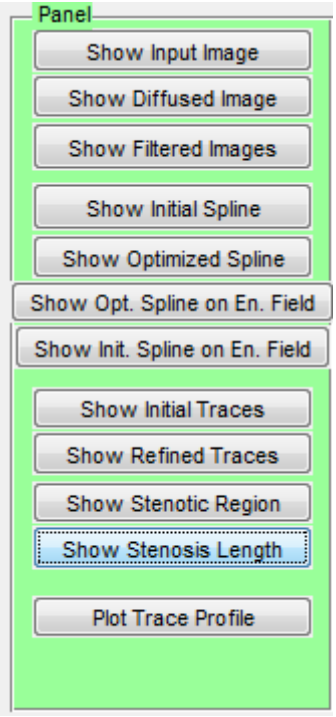

Figure B.20: Selective display panel that shows intermediate results of the algorithm.

B.11. Get Frame Panel

User can save the image that displayed in the output display area with a desired name to the current folder of MATLAB.

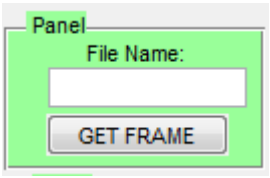

Figure B.21: Get Frame Panel